Investigations on supported nano-Silver Catalysts:
Correlation of Particle Size, Silver – Oxygen Interaction and Reactivity

vorgelegt von

Master of Science

Maximilian Lamoth

geboren in Bad-Kreuznach

von der Fakultät II – Mathematik und Naturwissenschaft

der Technischen Universität Berlin

zur Erlangung des akademischen Grades

Doktor der Naturwissenschaften

- Dr. rer. nat. -

genehmigte Dissertation

Promotionsausschuss

Vorsitzender:	Prof. Dr. Martin Lerch
Gutachter:	Prof. Dr. Robert Schlögl
Gutachter:	Prof. Dr. Thorsten Ressler
Gutachter:	Prof. Dr. Matthias Ballauff

Tag der wissenschaftlichen Aussprache: 01. Februar 2019

Berlin 2019

Acknowledgement

In the first place, I would like to express my sincere gratitude to Prof. Dr. Robert Schlögl, director of the department of Inorganic Chemistry at the Fritz Haber Institute of the Max Planck Society and of the department of Heterogeneous Reactions at the Max Planck Institute for Chemical Energy Conversion. He has given me the opportunity to conduct this interesting work in the field of heterogeneous catalysis at his institute, supported me with scientific guidance and provided an inspiring example for how to address the problems of our time.

I would like to particularly acknowledge Prof. Dr. Thorsten Ressler and Prof. Dr. Matthias Ballauff, who gladly accepted to invest their valuable time in reviewing this work. Additional gratitude goes to Prof. Dr. Martin Lerch for taking the chair of the examination board.

Especially I would like to acknowledge the dedication of my supervisor Dr. Elias Frei with which he supported me in many ways. With his scientific discussions he contributed significantly to the quality of this thesis.

Another and special thank you goes to my group leader Dr. Annette Trunschke and to Dr. Frank Rosowski as scientific director of BasCat, for their advice and discussions, most notably during the BasCat meetings.

I am also deeply grateful to my colleagues who scientifically supported me in many ways: Jasmin Allan (TGA, XRD), Wiebke Frandsen (SEM), Dr. Frank Girgsdies (XRD), Thomas Gries (SBA-15 synthesis), Rania Hanna (catalytic tests), Maike Hashagen (BET), Dr. Walid Hetaba (fundamentals of TEM), Dr. Travis Jones (theoretical calculations), Dr. Alexander Klyushin (XPS and Raman), Dr. Pierre Kube (catalytic tests and technical support), Dr. Albert Machoke (catalytic tests), Jessica Plagemann (BET), Dr. Milivoj Plodinec (TEM), Dr. Ludwig Scharfenberg (atmTAP), Dr. Gerardo Algara Siller (fundamentals of TEM), Dr. Andrey Tarasov (TGA), Dr. Olaf Timpe (ICP-OES) and Dr. Sabine Wrabetz (microcalorimetry).

Additionally, I would like to thank the Mechanical Workshop of the FHI as well as the Electronic Lab for their high-quality support of experiments end syntheses.

I would also like to thank the Reactivity Group, my colleagues and especially Dr. Gregor Koch, Dr. Leon David Zwiener, Elisabeth Wolf, Daniel Brennecke and Dr. Kathleen Lamoth for their scientific discussions and emotional backup during the past years.

Last but not least, my appreciation goes to my friends and family who supported me during a long way. Most of all my wife Kathleen, who supported me more than I could have wished for, at any time and place!

Abstract

A clear picture on the origin of the catalytic performance of silver (Ag) nanoparticles in heterogeneous catalytic oxidation reactions is still missing, even after decades of research. In this context, this thesis addresses the synthesis and investigation of Ag nanoparticles in the lower nanometer regime, particularly targeting the ability of activating oxygen and characterizing their silver – oxygen (Ag–O) interaction. The Ag nanoparticle catalysts are tested in the catalytic oxidation of carbon monoxide (CO) as well as the ethylene (C_2H_4) epoxidation reaction, which are both reported to be influenced by particle size related effects.

The synthesis of Ag catalysts supported on silica and corundum, using an improved impregnation technique, is demonstrated. The resulting Ag particle sizes can be divided into bulk-like, nanoparticles of 1 – 6 nm and *in-situ* created Ag clusters below 1 nm in diameter. All resulting supported catalysts are investigated in the catalytic oxidation of CO as probe reaction for their oxidation capability. Ag nanoparticles and bulk-like Ag are investigated concerning their pre-treatment dependence for CO oxidation and all catalysts are further tested regarding their CO oxidation performance. The related Ag–O interaction strength is discriminated by thermal desorption spectroscopy (TDS) combined with a novel method based on the adsorption of C_2H_4, in addition enabling the determination of the available Ag surface area. The combination of all methods facilitates a correlation of the Ag–O interaction strength, Ag surface area and CO oxidation activity.

Different supported Ag catalysts (bulk-like and nanoparticles) are further tested in the ethylene epoxidation reaction under industrially relevant conditions. The dependence of the catalytic performance on the oxygen concentration in/on Ag is additionally demonstrated. The combination of TDS and kinetic investigations is used to identify the relevant oxygen species responsible for the CO_2 formation and inhibition of the overall catalytic activity. Isotope experiments using $^{18}O_2$ and $C^{18}O_2$ are conducted to gain further insight on the nature and location of oxygen in/on the Ag nanoparticles. The results provide fundamental understanding on the performance of supported Ag particles in the ethylene epoxidation and reveal the origin of particle size related catalytic discriminations.

For an increased stabilization of Ag nanoparticles, in this work additionally the application of mesoporous silica SBA-15 as support material is investigated. A systematic variation of aging temperatures and dwell times, as well as the addition as NH_4F, is applied to reduce undesired microporosity. Their impact is correlated to the structural and chemical characteristics of the material. A direct influence of the structural properties on the chemical properties of the surface is extracted by isopropanol oxidation, a probe reaction for acid and redox active surface sites. As a consequence of the combined results by complementary techniques, a lower limit for surface area and related properties of SBA-15 is identified as descriptor, critical for its structural integrity and therefore also for its application as support material.

Zusammenfassung

Ein klares Bild über den Ursprung der katalytischen Leistungsfähigkeit von Silber(Ag)-Nanopartikeln in heterogenen katalytischen Oxidationsreaktionen fehlt auch nach jahrzehntelanger Forschung. In diesem Kontext wird in dieser Arbeit die Synthese und Untersuchung von Ag-Nanopartikeln im unteren Nanometerbereich beschrieben. Schwerpunkte liegen dabei auf ihrer Fähigkeit Sauerstoff zu aktivieren und der Charakterisierung der Silber-Sauerstoff (Ag – O) Interaktion. Die Ag-Nanopartikelkatalysatoren werden sowohl in der katalytischen Oxidation von Kohlenmonoxid (CO), als auch in der Epoxidierung von Ethylen (C_2H_4) getestet, die beide als durch Partikelgrößeneffekte beeinflusste Reaktionen beschrieben werden.

Die Synthese von geträgerten Ag-Katalysatoren auf Siliziumdioxid und Korund wird, unter Anwendung einer verbesserten Imprägnierungstechnik, demonstriert. Die resultierenden Ag-Partikelgrößen können in makroskopische Ag Partikel, Nanopartikel von 1 – 6 nm und *in-situ* erzeugte Ag-Cluster unter 1 nm im Durchmesser unterteilt werden. Die resultierenden Trägerkatalysatoren werden mittels einer katalytischen Test-Reaktion, der Oxidation von CO, auf ihre Oxidationsfähigkeit, sowie Ag-Nanopartikel und makroskopische Ag Partikel auf ihre Vorbehandlungsabhängigkeit, untersucht. Die damit verbundene Ag–O Interaktionsstärke wird durch die Thermodesorptionsspektroskopie (TDS) in Kombination mit einem neuartigen Verfahren auf Basis der Adsorption von C_2H_4 unterschieden, welche zusätzlich eine Möglichkeit zur Bestimmung der verfügbaren Ag-Oberfläche darstellt. Die Kombination aller Methoden ermöglicht eine Korrelation von Ag–O Wechselwirkungsstärke, Ag-Oberfläche und CO-Oxidationsaktivität.

Ausgewählte Ag-Katalysatoren (makroskopische und Nanopartikel) werden in der Ethylen Epoxidationsreaktion unter industriell relevanten Bedingungen getestet. Die Abhängigkeit der katalytischen Leistung von der Sauerstoffkonzentration in/auf Ag wird zusätzlich untersucht. Die Kombination von TDS und kinetischen Untersuchungen wird verwendet, um die relevanten Sauerstoffspezies zu identifizieren, die für die CO_2-Bildung und Hemmung der gesamten katalytischen Aktivität verantwortlich sind. Isotopenversuche mit $^{18}O_2$ und $C^{18}O_2$ werden durchgeführt, um weitere Erkenntnisse über die Art und Lage von Sauerstoff in/auf den Ag-Nanopartikeln zu gewinnen. Die Ergebnisse liefern grundlegende Erkenntnisse über die Leistungsfähigkeit von geträgerten Ag-Partikeln in der Ethylen Epoxidierung und zeigen den Ursprung der Partikelgrößen bezogenen katalytischen Diskriminierungen.

Für eine verbesserte Stabilisierung von Ag-Nanopartikeln wird in dieser Arbeit zusätzlich das Potenzial von mesoporösem Siliziumdioxid, SBA-15, als Trägermaterial untersucht. Zur Reduzierung der unerwünschten Mikroporosität werden eine systematische Variation von Alterungstemperaturen und Verweilzeiten, sowie die Zugabe von Ammoniumfluorid eingesetzt. Die Auswirkungen auf strukturelle und chemische Eigenschaften des Materials werden dabei untersucht. Ein direkter Einfluss der Struktureigenschaften auf die

chemischen Eigenschaften der Oberfläche wird durch die Isopropanol-Oxidation, eine Sondenreaktion für säure- und redoxaktive Oberflächenstellen, extrahiert. Aufgrund kombinierten Ergebnisse, basierenden auf komplementäre Techniken, wird eine minimale Oberfläche und die damit verbundenen Eigenschaften des SBA-15, als Deskriptor identifiziert, der für seine strukturelle Integrität verwendet werden kann, und damit auch für seine Anwendung als Trägermaterial entscheidend ist.

Contents

Abbreviations

a_0	unit cell dimension
ADF	annular dark-field
α-Al_2O_3	corundum
atmTAP	temporal analysis of products approach at atmospheric pressure
a.u.	arbitrary units
Ag–O	silver – oxygen
$Ag^{\delta+}$	partially oxidized silver
BET	Brunauer-Emmet-Teller
c	molar concentration
D_p	pore diameter
E_A	activation energy
E_{ads}	adsorption energy
EDX	energy dispersive X-ray spectroscopy
EGA	evolved gas analysis
EO	ethylene epoxide
eq	equivalents
fcc	face centered cubic
FID	flame ionization detector
F_V	total volumetric flowrate
GHSV	gas hourly space velocity
HTA	high temperature aging
ICP	inductively coupled plasma
IR	infrared
LTA	low temperature aging
M	molarity
n	reaction order
N_{ad}	number of moles per adsorbed molecules
m/z	mass per charge
O_{ads}	adsorbed oxygen atom
OES	optical emission spectrometry

PDF	powder diffraction file
PEO	poly(ethylene oxide)
PPO	poly(propylene oxide)
PS	particle size
(P)XRD	(powder) X-ray diffraction
Q_{ads}	integral heat of adsorption
S	selectivity
$S(\infty)$	steady-state signal
SA	surface area
SD	standard deviation
SEM	scanning electron microscopy
$S_{\mu\text{-pore}}$	micropore surface area
(S)TEM	(scanning) transmission electron microscopy
S_{total}	total surface area
t	time
T	temperature
$T_{10\%}$	temperature for 10 % conversion
TCD	thermal conductivity detector
TGA	thermogravimetric analysis
TPR	temperature programmed reduction
wt.-%	weight percent
X	conversion
XPS	X-ray photoelectron spectroscopy

1 Introduction

The progressively increasing population, which almost tripled since the 1950s, enforces an equally increasing demand for chemical feedstocks. Hereby, the catalytically driven syntheses is a key aspect[1] to deal with the projected growth in world chemical sales expected to almost double from the year 2016 to 2030.[2] Among the worldwide produced petrochemical based materials, ethylene represents the second-largest volume, after ammonia.[3] It is mainly produced by thermal cracking of hydrocarbons in the presence of steam (steam cracking). A significant fraction of ethylene is converted into ethylene epoxide (EO), which had a global production capacity of 34.5 million tons in 2016,[4] with ethylene glycols being used to produce antifreezes and polyesters as main products.

EO is synthesized in a heterogeneous catalytic reaction by the partial oxidation of ethylene[5, 6] as illustrated in Figure 1A. The reaction is performed at elevated temperature (200 – 280 °C) and pressure (14 – 20 bar). As catalyst, corundum (α-Al_2O_3) supported silver (Ag) is employed with loadings of around15 weight percent (wt.-%). Undesired side products are acetaldehyde, which also occur upon isomerization of EO, or CO_2 as total combustion product. The EO molecule, as shown in Figure 1B, belongs to the group of cyclic ethers and exhibits a highly strained structure. It exhibits a high reactivity which correlates with the highly exothermic ring opening of the molecule. The total combustion reaction, with $\Delta H_{C2H4 \rightarrow CO2} = -1423\ kJ \cdot mol^{-1}$, is furthermore the thermodynamically favored oxidation product compared to the formation of EO with $\Delta H_{C2H4 \rightarrow C2H4O} = -105\ kJ \cdot mol^{-1}$.[6, 7] Consequently, the high reactivity is also a main cause for its challenging synthesis, so that up to date, Ag has been found to be the only metal that can catalyze the direct oxidation of ethylene to EO with a sufficiently high selectivity.[8]

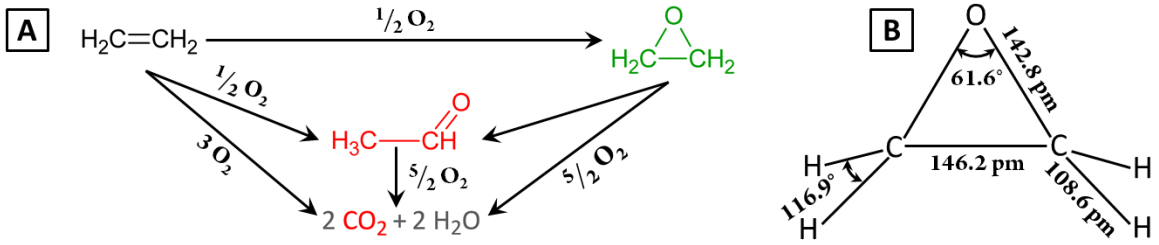

Figure 1. Overview of ethylene oxidation reactions (A) and physical properties of the ethylene epoxide molecule (B). Data for (B) are taken from reference [6].

The application of other transition metals as oxidation catalysts results in the complete combustion of ethylene.[9, 10] The complexity can be further illustrated by the change in achieved selectivity towards EO in the last decades. While un-promoted Ag is reported to reach a selectivity of around 50 %[11], modern industrial catalysts reach up to 90 % using various promotors, precisely adjusted synthesis and reaction parameters[5]. All these improvements could mainly be made by trial-error methods, since the interaction of all contributions

is so far still not completely understood.[12-15] To facilitate further improvements, this thesis contributes to a deeper understanding of Ag based catalysts, especially with regard to the ethylene epoxidation reaction.

1.1 Catalytic relevance of the silver – oxygen interaction

The unique character of Ag regarding the partial oxidation of ethylene is based on its chemical interaction with oxygen. It was demonstrated by Nagy *et al.*[16] that oxygen can diffuse into the Ag subsurface region *via* an interstitial mechanism using low-resistance diffusion paths originating from grain boundaries and open crystalline planes to form bulk-dissolved oxygen. The dissolved species were also shown to segregate into low-indexed planes (surface-embedded oxygen) by a proposed diffusion mechanism in which oxygen substitutes Ag atoms in the lattice at elevated temperatures above 600 °C. The diffusion was monitored by applying X-ray diffraction (XRD) analysis of Ag powder in *in-situ* oxidizing, pure oxygen atmosphere. Thereby, the effect of dissolved oxygen on the structure of the Ag lattice was investigated. With increasing temperature, the unit-cell was shown to expand. It thereby provided a direct evidence for the incorporation of oxygen into the Ag bulk since the expansion can be regarded as a consequently secondary effect of the oxygen diffusion.

A deeper look into the Ag structure can further help to understand the occurrence of the described oxygen diffusion. Since Ag exhibits a face-centered cubic (*fcc*) packing structure, one unit cell comprises four octahedral voids (one per Ag atom) and eight tetrahedral voids (two per Ag atom). Taking the atomic radii of oxygen and Ag into account, it can be proven that oxygen atoms fit into the larger octahedral voids while the tetrahedral voids are too small.[17, 18] However, oxygen occupying octahedral voids in the Ag lattice can be described as relevant diffusion sites, as illustrated in Figure 2.[19] Thereby, it is likely that oxygen atoms diffuse from one octahedral void to an adjacent one through neighboring tetrahedral voids.

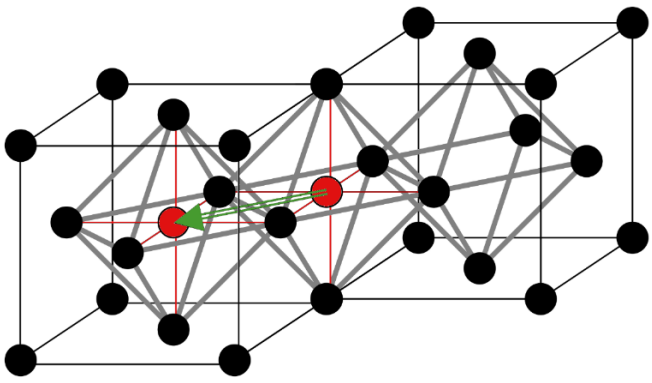

Figure 2. Shown are two unit cells of Ag and the direction of oxygen atom diffusion (red circles and green arrow) using octahedral voids in the *fcc* Ag lattice (black circles). (Adapted from reference [20])

As a member of the 11th group in the periodic table of elements, valence isoelectronic metals are copper (Cu) and gold (Au), also crystallizing in the *fcc* lattice structure. However, it is well known that Au exhibits an extraordinarily high resistance to oxygen, which is a strong indicator that oxygen is not stabilized on or in Au

as described for Ag. Additionally, Ag and Au exhibit nearly the same atomic radii, which rules out stearic effects as hindrance for e.g. oxygen diffusion. On this basis, Eberhard *et al.*[19] investigated Ag, Cu and Au regarding their oxygen diffusivity. They could identify that oxygen is able to diffuse through Ag as well as Cu, while Au shows no oxygen diffusibility. Electronic calculations showed that the presence of oxygen in the octahedral sites of the Ag and Cu lattice resulted in a weakening of the bonds between adjacent metal-atoms. This consequently leads to an expansion of the Ag or Cu lattice with a decreased electron density for neighboring metal atoms which reduces the diffusion resistance. The opposite effect was observed for Au, with oxygen causing an increase in the metal-metal bond strength resulting in an increased diffusion resistance. It is supported by Jones *et al.*[21], demonstrating that the solubility of oxygen in Au and Ag is mediated by the energy cost of breaking metal–metal bonds.

An additional physical property of oxidized Ag makes the silver – oxygen (Ag–O) chemistry unique. The decomposition temperature of silver oxide (Ag_2O) of around 200 °C[22] is located in the temperature regime for the industrial ethylene epoxidation reaction of 200 – 280 °C,[5] while Cu(II) oxide decomposes to Cu(I) oxide at 1030 °C.[23] Consequently, a stable bulk oxide formation for Ag cannot take place under the conditions required for epoxidation.[24, 25] Instead, it was directly observed that surface reconstructions with $Ag^{\delta+}$ sites are formed, which are necessary for ethylene adsorption and a prerequisite for (ep)oxidation.[26, 27]

The intriguing surface and subsurface Ag–O chemistry explain why exclusively Ag catalysts are used for the ethylene epoxidation reaction. Further, besides the described bulk-dissolved and surface-embedded oxygen, a large variety of oxygen species have been described like weakly adsorbed atomic or molecular and strongly bound, ionic and covalent species, located surface, subsurface or near defects.[13, 28] Some oxygen species related to the epoxidation process on the Ag surface have been characterized by applying X-ray photoelectron spectroscopy (XPS) of the oxygen O 1s edge, as illustrated in Figure 3. Changes in the bonding characteristics of oxygen atoms result in shifts in their core-level binding energies, allowing their distinction.

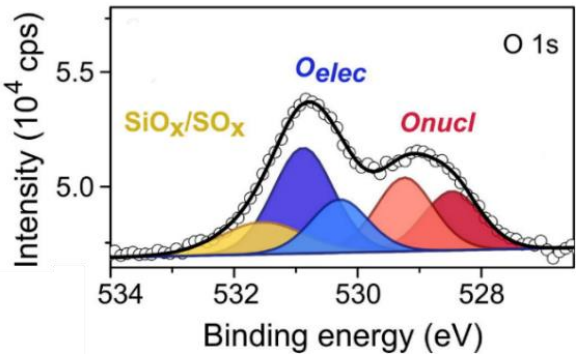

Figure 3. Representative XPS spectrum of the oxygen O 1s edge of Ag powder measured after 12 h *in-situ* ethylene epoxidation reaction at 230 °C.[13] *Oelec* = electrophilic oxygen, *Onucl* = nucleophilic oxygen

Thereby, oxygen atoms with higher partial charge (strongly bound, nucleophilic oxygen) are reported to be responsible for C–H bond cleavage of ethylene, which is the first step to the total oxidation path. Less charged oxygen atoms (weakly bound, electrophilic oxygen) interact preferentially with the ethylene π-bond forming the epoxidation product.[29, 30]

The Ag–O system has also been well characterized by the application of thermal desorption spectroscopy (TDS) of oxygen by numerous studies.[16, 28, 31-33] The Ag–O interaction strength can hereby be evaluated by the desorption temperature of oxygen. Comparable to the XPS technique, a variety of oxygen species have been described.[16, 31] Some of those, however, change regarding their desorption temperature upon varying treatment conditions like oxygen partial pressures and temperatures or desorption conditions. It makes correlations regarding their catalytic relevance complicated, but clearly demonstrates that the pronounced oxygen subsurface chemistry plays an important role in catalysis and further points out the described intriguing behavior of oxygen in and on Ag.[16, 31] Nevertheless, it represents a suitable technique to extract information on the Ag–O chemistry. In addition, a particular advantage of TDS approaches is the possible analysis of also insulating materials, as it is the case for metal nanoparticles supported on alumina or silica. Those are usually not accessible by surface techniques that involve electrons as information carrier due to various charging effects.[34] The use of thin oxide films as support material provide a solution to this problem, but only represent a model system which is not necessarily transferable to "real-world" catalytic systems.[1, 35] Based on the described advantageous and possibilities offered by the TDS approach, it also applied to investigate the Ag–O interaction of various supported Ag catalysts as demonstrated in chapter 2 and chapter 3.

The vital role in catalysis of oxygen species in and on Ag gets furthermore obvious when considering that metallic Ag is not able to interact with C_2H_4 since its electronic configuration of s^1d^{10} does not allow transferring electrons to the Ag d-band.[25, 36, 37] For the partially oxidized $Ag^{\delta+}$, electron density from the Ag^0 d-band is removed which enables the donation of π-electrons. This allows C_2H_4 to interact with all kinds of Ag^+ sites, from Ag_2O to $Ag^{\delta+}$ from partially oxidized $Ag^{\delta+}O_x$. Furthermore, the strength of the Ag–O interaction is affecting the C_2H_4 interaction strength with $Ag^{\delta+}O_x$, since the binding strength of C_2H_4 depends on the corresponding acceptance of π-electrons. This strength also strongly affects the selectivity during the epoxidation. As side benefit, C_2H_4 can thereby be applied as sensor molecule for described Ag sites which can be used to contribute to the understanding and characterization the complex Ag–O chemistry. This novel approach is demonstrated in chapter 2.

1.2 Silver particle size effect

Most of the above described contributions to the Ag–O chemistry were made on model system like single crystals, foils or powders. Those are usually in dimensions of at least a few hundred nanometers and therefore

representative for bulk Ag characteristics. Industrially relevant catalysts, however, consist of supported silver particles which also involves the formation of Ag particles in the regime below 100 nm, as illustrated exemplarily in the scanning electron microscopy (SEM) image in Figure 4 for Ag supported on low-surface area corundum.

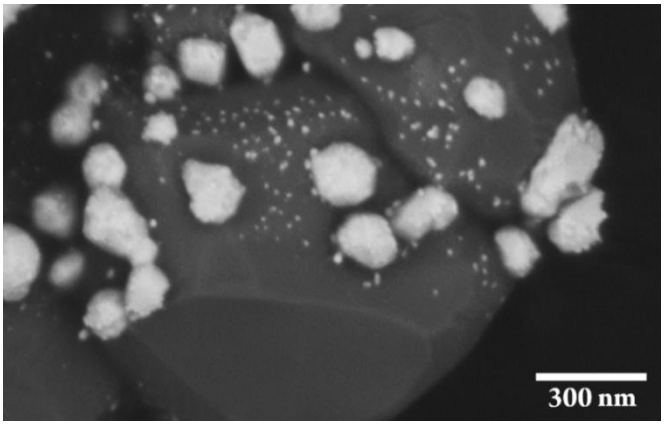

Figure 4. SEM image of silver nanoparticles supported on corundum. Bright spots refer to Ag. Besides the presence of particles larger than 100 nm, also Ag nanoparticles in the lower nanometer regime of below 10 nm in diameter can be identified.

The relevance of that particular particle size regime had already been investigated by Peter Harriott in 1971, since a strong particle size effect had at this time already been reported for other metal catalyzed reactions.[38] He observed that silica (SiO_2) supported Ag particles even below 10 nm in size can result in a reasonable activity as well as selectivity to EO. He also proposed that, if an effect for the particle size does exist, it must take place for particles below 3 nm. Up to now, this proposal has not been reviewed since the synthesis and investigation of small and stabilized Ag nanoparticles, especially of only a few nanometer in size, is challenging.[1, 39] This might also be the reason why in the following years further studies aiming at the investigation of Ag particle size effects in the ethylene epoxidation reaction have been performed for mainly 10 – 100 nm supported Ag particles. An exception is represented by Wu and Harriott[40] who studied supported Ag on silica in the range of 3 – 50 nm Ag particle size. They observed the highest conversion of ethylene, $X(C_2H_4)$, at around 5 – 6 nm. In contrast to Harriott's previous study, they observed a low selectivity to EO, $S(EO)$, which steadily increased with increasing Ag particle size up to around 50 nm, representing the largest Ag particle size investigated in their work. A following considerable contribution was made by Cheng and Clearfield[41], resulting in a maximum for $S(EO)$ and $X(C_2H_4)$ at around 50 nm, being in contrast to the previous study. Furthermore, they observed a decrease in selectivity as well as conversion for larger particle sizes. Lee *et al.*[42] observed again a steady increase in $S(EO)$ for increasing Ag particle size, ranging from investigated 6 – 50 nm. It remained at a maximum for larger particle sizes (50 – 100 nm) in the case of silica supported particles but showed a decrease in $X(C_2H_4)$ when supported on corundum. The same increase was observed for the $X(C_2H_4)$, reaching a maximum at 40 – 50 nm in the case of corundum supported Ag and a

plateau starting at around 60 nm for silica supported Ag. Hereby, only the corundum supported Ag catalyst performed similar to the results by Cheng and Clearfield. Goncharova *et al.*[43] showed a steady increase in $S(EO)$ from 10 – 100 nm, and a maximum in $X(C_2H_4)$ for around 50 nm followed by a plateau, as observed by Lee *et al.* Recent results from 2017 regarding a Ag particle size effect were presented by Reijen *et al.*[44] In contrast to the previous investigations, they compared the $S(EO)$ at a constant low $X(C_2H_4)$ of 2.8 %, resulting in constant $S(EO)$ for various Ag particle sizes. Consequently, no particle size effect was attributed to the selectivity in the range of 20 – 200 nm Ag particle size. The achieved $X(C_2H_4)$ were again in agreement with previous reported studies, reaching its maximum at 60 – 70 nm.

Recapitulating, based on the inconsistent results after more than 40 years of research, it is still unclear if a Ag particle size effect for the ethylene epoxidation reaction exists. Although a consent seems to have formed, stating that Ag particles below 10 nm are "known to exhibit no catalytic activity"[45], a recent result further calls this into question. Fotopoulos *et al.*[46] achieved the synthesis of silica supported, in average 9 nm, Ag particles. They thereby demonstrated that Ag particles smaller 10 nm can reach $X(C_2H_4)$ of up to 65 % with $S(EO)$ of 30 – 35 %. They exhibited a comparable performance as a corundum supported reference catalyst with significantly larger Ag particle sizes, underlining the open question of the influence of particle size on the epoxidation of ethylene.

In the case of insufficient data, as described for Ag particles below 10 nm and their performance in the ethylene epoxidation, one can search for comparable effects for related catalytic reactions. An example is the oxidation of carbon monoxide (CO) applying Ag based catalysts, which was reported to show Ag particle size related effects. Lim *et al.*[47] performed XPS measurements of Ag particles that were synthesized by evaporating a Ag rod on highly oriented pyrolytic graphite (HOPG). The Ag nanoparticles below 3 nm showed a single peak at 531 eV in the O 1s spectrum upon oxidation. This oxygen species was shown to be unreactive towards the oxidation CO, indicating that also the 3 nm sized particles are inactive. Qu *et al.*[48] observed a similar effect, with a volcano type dependence and a maximum activity in CO oxidation for Ag particles with a mean size of about 6 – 8 nm. Interestingly, Lei *et al.*[49] demonstrated that for the propylene epoxidation reaction on Ag, a beneficial effect for sub-nanometer sized Ag particles exists.

Regardless of whether the effect is promoting or inhibiting the catalytic performance, it is undoubted that a metal particle size effect is expected to be located in the particle size range of roughly below 5 nm.[50-53] This hypothesis is supported by investigations of the Campbell group that demonstrated that Ag[54-56], as well as Cu[57, 58] and Au[59] exhibit divergent effects when decreasing below a certain particle size.[60, 61] They determined adhesion energies *via* single crystal adsorption calorimetry by measuring the heat of adsorption of metal atoms as they are vapor deposited onto single-crystal oxides under ultrahigh vacuum. An example for

the heat of Ag atom adsorption onto different oxide surfaces is illustrated in Figure 5. The Ag atoms transiently adsorb on clean parts of the oxide surface but quickly diffuse across the surface and add to form Ag particles on the surface. Shown are the particle sizes in the range up 8 nm and the measured heat of the Ag atom adsorption versus the final resulting Ag particle diameter to which it adds. The corresponding chemical potential, which is estimated by the difference in magnitude between the bulk heat of sublimation of the metal and its differential heat of adsorption on particles of that size, is significantly increasing for Ag particle sizes below 4 nm, in the case of MgO(100) below 6.5 nm. This observation reveals that this particle size regime is of great importance for Ag catalyzed reactions, especially oxidation reactions. Although the investigated interactions are on oxidic supports, it can be assumed that a comparable phenomenon could exist for the interaction of Ag particles with any kind of oxygen, which will also be investigated and discussed in the later course of this work in chapter 2 for the CO oxidation and chapter 3 for the ethylene epoxidation reaction.

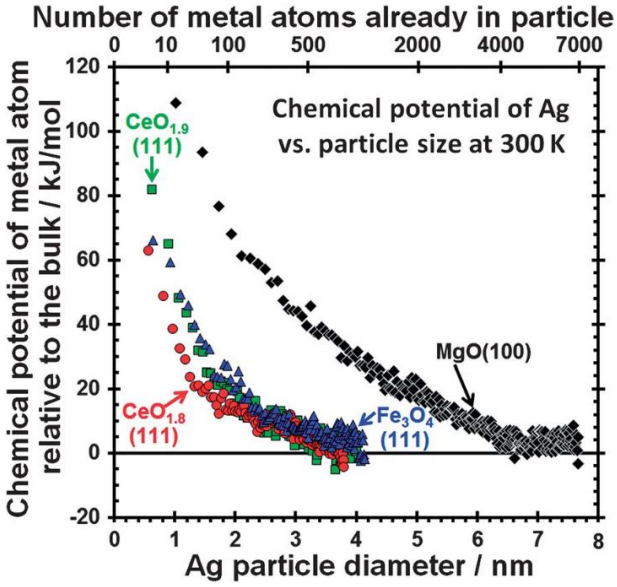

Figure 5. Chemical potential of Ag atoms in Ag nanoparticles on different oxide surfaces versus the average Ag particle size. Entropy differences are neglected.[61]

1.3 Synthesis and stabilization of silver nanoparticles

The mere knowledge of a potential particle size effect can solely be regarded as the first step. A prerequisite for its investigation is the successful synthesis of the relevant particle size, being present in a narrow particle size distribution and stable under the desired reaction conditions. Those requirements can be realized by choosing a proper support material as well as a suitable synthesis method.

A common strategy for metal nanoparticle stabilization is the use of metal-support interactions that are based on a certain functionality of the support.[62-66] However, due to high reactivity of EO, employed support materials need a high degree of chemical inertness to not further convert EO to undesired products. The way

how to determine this important support characteristic was introduced by Harriott[38] who dosed EO over various alumina and silica materials to test their deployability in the ethylene epoxidation reaction. He demonstrated that different supports show different EO oxidation behaviors. Thereby, he was able to show that alumina samples with decreasing amount of the alpha phase, in return meaning an increasing amount of transition alumina phases, have a higher EO oxidation rate. He also showed that SiO_2 materials exhibit a very low EO oxidation rate comparable to pure α-Al_2O_3 of around 8 $m^2 \cdot g^{-1}$, despite their higher surface area of 350 $m^2 \cdot g^{-1}$. Kanoh *et al.*[67] confirmed this result and further introduced the concept of the isomerization of EO to acetaldehyde taking place on the support with its subsequent oxidation happening on the Ag particles. Lee *et al.*[68] went back to the role of the support and extended the study to a broad field of oxidic supports. They concluded that only α-Al_2O_3, SiO_2, ZrO_2, SiC and TiO_2 (rutile) are selective towards EO, with their S(EO) listed in descending order. All other supports, namely TiO_2 (anatase), Al_2O_3 (boehmite), Nb_2O_5, V_2O_5, MgO and Y_2O_5, were only active in the isomerization or total oxidation of EO. Thereby, the acetaldehyde formation was attributed to the acidity of the support. It was supported by Yong *et al.*[69] who interpreted the formation of major organic products to be effected by weak Brønsted acidic sites. They also used the EO decomposition/isomerization test to show that by introducing Ag in SiO_2, the main conversion product changed from acetaldehyde to mainly CO_2, being in agreement with the concept reported by Kanoh *et al.* The measurement of the surface acidity by infrared (IR) spectroscopy additionally supports the low surface acidity for silica, despite their high number of functional hydroxyl groups. Hereby, Brønsted acidic sites can be detected indirectly *via* their interaction with bases of appropriate strength and by monitoring the formation of the corresponding protonated species. Lewis acidic sites are analyzed by adsorption of basic probe molecules like pyridine, whereby the strength of shift of the corresponding IR bands upon adsorption is interpreted as indication for the sample's acidity.[70,71]

A complementary method is the adsorption and reaction of alcohols on metal oxide catalysts as chemical probe reaction for surface acid-base properties and therefore also chemical reactivity of the surface. Ai and Suzuki[72] correlated acidic and basic properties of metal oxide catalysts with their rates of dehydration and dehydrogenation of isopropanol. Their work showed that using the reaction products from isopropanol oxidation, a reflection of the nature of the active surface of catalysts or supports is possible. In their work it was shown that isopropanol can undergo dehydration resulting in propylene formation on acidic surface sites or dehydrogenation *via* a concerted mechanism on adjacent acidic and basic surface sites yielding acetone.

Based on the described literature reports, only α-Al_2O_3 and SiO_2 materials demonstrated the necessary chemical inertness towards EO. However, a support that should be able to stabilize metal nanoparticles of only a few nanometers should exhibit a high number of functional groups. Silica materials provide a high number of low acidic hydroxyl groups. In contrast, the low surface acidity of α-Al_2O_3 is based on the high

temperature synthesis applying more than 1100 °C.[73] It decreases the number of acidic groups to an almost neglectable amount, which is also correlated to the reduction of the specific surface area down to usually below 5 $m^2 \cdot g^{-1}$.[5] Therefore, α-Al_2O_3 cannot be employed as support for nanoparticles with a desired size below 10 nm. Consequently, only silica remains as suitable support. The available surface area is thereby another crucial parameter and determines the particle dispersion and thereby also the smallest achievable particle size. A high surface area additionally increases the sintering stability based on an increased interparticle distance, making porous silica materials an attractive choice.[74, 75] Among them, mesoporous SBA-15 shows also the necessary thermal stability to be applied under reaction conditions, and is therefore in detailed studied in chapter 4.[76, 77] Also non-porous silica synthesized by flame hydrolysis offer a high surface area and show a high structural as well as textural stability.[78] They are furthermore easily commercially available and are therefore identified as suitable support material for the synthesis of small nanoparticles, hence applied as support material in chapter 2 and chapter 3.

An adequate support meterial can be loaded by impregnation, which is the preferred method if the catalytically active phase should be present as nanometer-sized particles.[79] The OH-group rich surface of SiO_2 thereby provides anchoring sites for the catalyst precursor by undergoing ion exchange reactions of Ag^+ ions as illustrated in Figure 6A, distributing and stabilizing the precursor over the complete support surface area.[80] This, however, is only possible if the impregnation solution is water based due to the hydrophilic surface of the applied silica support. A silver nitrate ($AgNO_3$) based precursor, offering a high solubiulity in water, is therefore the precursor of choice. $AgNO_3$ additionally enables a controlled development of Ag nanoparticles by thermally induced precursor decomposition (thermolysation) through melting at 210 °C before its decomposition at 440 °C.[22] This treatment represents the last synthesis step for supported Ag catalysts and leads to the formation of supported metallic Ag nanopoarticles, as illustated in Figure 6B.

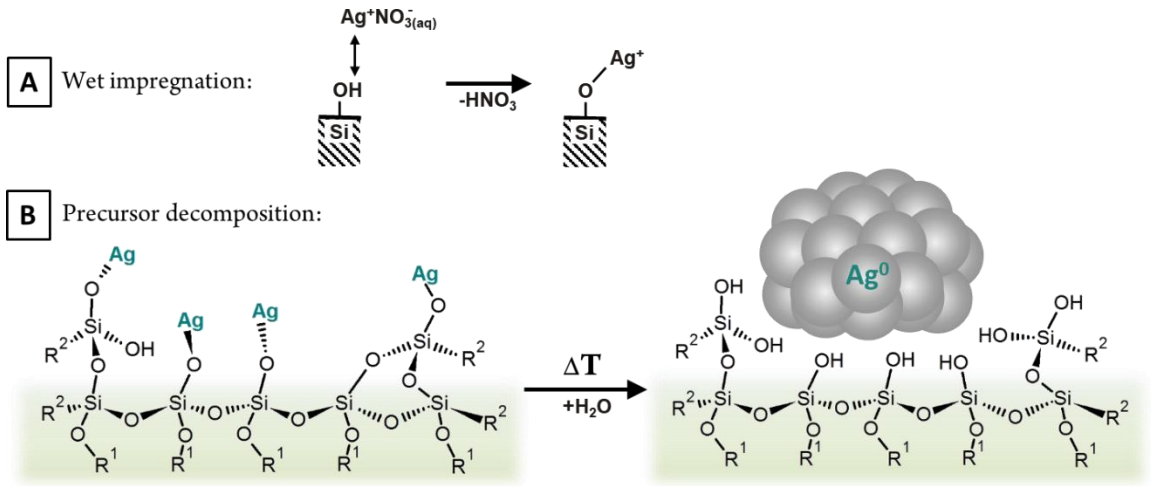

Figure 6. Scheme of a wet impregnation approach on a silica support using aqueous silver nitrate ($AgNO_{3(aq)}$) as Ag precursor. (A) illustrates the ion exchange reaction upon impregnation and (B) the metallic Ag nanoparticle formation induced by the precursor decomposition, inducing the reduction of Ag^+.

1.4 CO oxidation as test reaction

CO can be regarded as a common probe molecule for the investigation of surface sites with its oxidation being applicable as a model reaction for more complex oxidation reactions like the epoxidation of ethylene. Thereby, the CO oxidation represents a prototypical reaction, since it is one of the best-known heterogeneous reactions and can therefore also be regarded as benchmark system. It facilitates the reduction of the complexity of the applied catalysts by observing their reactivity to CO and O_2. Hereby, the oxidation of CO is rather used as chemical probe for the catalysts surface properties than a real catalytic performance test.[81] It is also believed that the knowledge gained from single crystal studies are transferrable to oxide-supported nanoparticles when they are prepared under well-defined conditions, which further underlines the value of CO oxidation as a model reaction.[82] Furthermore, the reaction cannot happen in the gas phase (spin forbidden), because the reactants have a total spin of $S = 1$ (triplet ground sate of O_2) while the reaction product CO_2 exhibits $S = 0$. The necessary dissociative adsorbed oxygen on a catalyst is in the zero-spin state, though the reaction can proceed. The neglection of gas phase reactions is therefore also a beneficial effect. An additional fundamental advantage of CO oxidation is the presence of one rate determining step (adsorption of CO) and the evolution of one single product. The oxidation product CO_2 thereby interacts much weaker with the surface metals than CO does, which also simplifies the measurement and the interpretation of the reaction data. It is also worth mentioning the reaction occurs over a wide range of 13 orders of magnitude of pressures[83], which allows investigations being conducted under various conditions.

The CO oxidation reaction mechanism has been well investigated with clear evidence for Langmuir-Hinshelwood kinetics.[84] It includes, as mentioned, a dissociative adsorption of O_2 into atomic oxygen species. They can, as described for the case of Ag, be located in various forms at subsurface or surface sites of the metal. The oxidation further prerequisites that both reactants are in close proximity to each other to be able to undergo the oxidation reaction. Therefore, the adsorption sites must implicate a certain characteristic which can only be fulfilled by an ensemble of atoms that exhibit an electron-accepting Lewis function which adsorbs CO and additionally stabilizes weakly bound, electrophilic oxygen that is capable of oxidizing CO. As already mentioned, the electrophilic oxygen also plays a crucial role in the ethylene epoxidation reaction. Its indirect investigation using CO as sensor molecule can therefore be a useful descriptor for a catalysts epoxidation capability.

A catalyst can also be “poisoned” by high oxygen and/or CO concentrations on the surface of the active material. Oxygen needs two nearby sites to undergo the described dissociative adsorption, whereby CO only interacts with one adsorption site. The consequence of the catalytic oxidation reaction for which an adsorbed oxygen atom reacts with an adsorbed CO molecule to gaseous CO_2 ($O_{ad} + CO_{ad} \rightarrow CO_{2,gas}$) leaves two free adsorption sites remaining. They can be occupied by one O_2 molecule undergoing dissociation to two O_{ad} or

by two CO molecules. However, the adsorption of only one CO molecule hinders the second site to be available for O_2. Thereby, an enrichment of CO_{ad} species can occur if they are not desorbed or oxidized. Alternatively, the surface can also become oxygen rich and thereby prevents the adsorption of CO. For both cases, potentially active reaction pathways are disabled. The necessary desorption of CO or O_2 to "self-heal" the catalyst can only happen in an appropriate chosen pressure and/or temperature range. Moreover, this reveals the importance of appropriate pre-treatment conditions, since a surface oxygen-rich catalyst will be less active in the early stages of the reaction due to an already oxygen-poisoned state. Elevated pre-treatment temperatures, strongly depending on the Ag–O interaction of the Ag catalyst, can lead to desorption of O_{ad} from occupied adsorption sites. The result would be a higher initial reactivity based on an increased number of potential CO adsorption sites. Based on this concept, the CO oxidation can also be used as a sensor for the oxygen interaction of the catalyst. Such an approach is also demonstrated in chapter 2. It also shows that the oxidation of CO can be interpreted as an indicator for the capability of a catalyst to active O_2, which is also a key parameter for catalysts used in the ethylene epoxidation reaction.

The reductive character of CO can also be applied *in-situ*, since it represents a mild reduction for Ag precursor materials to obtain metallic Ag. Such an approach can be beneficial in terms of the synthesis of preferably small metal nanoparticles. Thereby, an *in-situ* formation of metal nanoparticles can be induced, whose effect is also studied in chapter 2 of this thesis.

A rather straight forward information that can be concluded from the catalysts activity in CO oxidation is the stability of the Ag nanoparticles towards sintering, which is increasing with decreasing size.[85] The exothermic oxidation of CO,[81] especially at elevated temperatures, unavoidably transfers thermal energy to the particles, further promoting the sintering process. It consequently leads to a decrease of available surface sites and therefore decreases the reaction rate of CO oxidation. This sensitivity of CO oxidation to the available surface area of the metal provides the basis to use CO oxidation also as a test reaction for the stability of the catalyst. This allows the determination of unappropriated treatment conditions, as further demonstrated in chapter 2.

1.5 Objective and outline

This thesis addresses the investigation of a potential Ag particle size effect in the oxidation of CO as well as the partial oxidation of ethylene. The observed effects are correlated to the specific Ag nanoparticles size and their interaction strength to oxygen. The characterization of the particle size dependent "Ag–O fingerprint" enables the identification of the origin of diverging catalytic performances for different supported Ag nanoparticle sizes.

In this context, chapter 2 demonstrates the synthesis of Ag nanoparticles below 6 nm in diameter, supported on hydrophilic fumed silica (Ag/SiO_2). The resulting highly stable catalysts are applied in the oxidation of CO, which is used as a test reaction for oxygen activation as well the capability of small Ag nanoparticles to perform catalytical oxidation reactions. The test reaction additionally gives first indications of the corresponding Ag–O interaction, which is studied in more detailed by O_2-TDS analysis and microcalorimetry. For a possible correlation of available active surface area and catalytical performance, various Ag/SiO_2 catalysts as well as a corundum supported reference sample (Ag/α-Al_2O_3) are characterized concerning their Ag surface area using a newly developed method based on their adsorption capacity for ethylene. In combination with kinetic investigations, this allows a clear discrimination between particle size effects and an increase of active surface area due to simple dispersion effects of nanostructures.

In chapter 3, the knowledge gained from chapter 2 is transferred to the catalytic epoxidation of ethylene to EO. Ag/SiO_2 catalysts as well as the Ag/α-Al_2O_3 reference are thoroughly tested in the epoxidation reaction under industrially relevant conditions. Nature and location of adsorbed oxygen species are analyzed using $^{18}O_2$ and $C^{18}O_2$ labeled TDS experiments. The influence of these species is shown by variations of their amount available for catalysis and the related consequences on the selectivity as well as activity in the ethylene epoxidation. Thereby, the catalytical performances are correlated to the corresponding Ag–O fingerprint *via* TDS analysis at different states of the catalyst's activation. Together with kinetic investigations and EO decomposition/isomerization tests, valuable knowledge about the selective state of Ag catalysts in the ethylene epoxidation reaction is created.

Chapter 4 investigates the potential of mesoporous silica SBA-15 being applied as support material. Besides the hydrophilic fumed silica used as support in chapter 2 and chapter 3, SBA-15 represents a promising candidate for providing an increased stabilization of Ag nanoparticles. However, the bottleneck of SBA-15 synthesis is the reduction of its microporosity while increasing the mesopore size without significantly decreasing the pore wall thickness being a key parameter for its thermal stability. Also, the overall surface area is desired to be as high as possible. The change of the SBA-15 properties after various high temperature aging (HTA) procedures and the application of fluoride species which are used to pronounce the HTA effect is thoroughly investigated. The combination of N_2 physisorption methods, low angle X-ray diffraction as well as transmission electron microscopy analysis allows the identification of critical synthesis parameters that should be avoided for the sake of structural integrity. The application of isopropanol oxidation tests further enables the correlation of physical changes to transitions in the chemical surface properties.

1.6 References

[1] R. Schlögl, *Angew. Chem., Int. Ed.* **2015**, *54*, 3465-3520; *Angew. Chem.* **2015**, 127, 3531-3589

[2] Facts & Figures 2017 of the European chemical industry, *December 2017*, European Chemical Industry Council

[3] *Chemistry of the Elements (Second Edition)* (Eds.: N. N. Greenwood, A. Earnshaw), Butterworth-Heinemann, Oxford, **1997**, pp. 406-472.

[4] Global and China Ethylene Oxide (EO) Industry Report, 2017-2021, *July 2017*, Report ID: 5013139

[5] T. Rosendahl, T. Mäurer, C. K. Dobner, A. Lehr, J. Wanka; WO 20130/61294 A1, **2013**, BASF SE, Ludwigshafen (GER)

[6] S. Rebsdat, D. Mayer, in *Ullmann's Encyclopedia of Industrial Chemistry*, Wiley-VCH Verlag GmbH & Co. KGaA, **2000**.

[7] J. P. Dever, K. F. George, W. C. Hoffman, H. Soo, in *Kirk-Othmer Encyclopedia of Chemical Technology, Vol. 10*, Wiley, **2004**, pp. 632 -673.

[8] M. O. Ozbek, I. Onal, R. A. van Santen, *J. Catal.* **2011**, *284*, 230-235.

[9] K. Reuter, M. Scheffler, *Appl. Phys. A* **2004**, *78*, 793-798.

[10] M. Mavrikakis, D. J. Doren, M. A. Barteau, *J. Phys. Chem. B* **1998**, *102*, 394-399.

[11] R. A. Van Santen, H. P. C. E. Kuipers, in *Adv. Catal., Vol. Volume 35* (Eds.: D. D. Eley, H. Pines, P. B. Weisz), Academic Press, **1987**, pp. 265-321.

[12] M. O. Özbek, R. A. van Santen, *Catal. Lett.* **2013**, *143*, 131-141.

[13] T. C. R. Rocha, M. Hävecker, A. Knop-Gericke, R. Schlögl, *J. Catal.* **2014**, *312*, 12-16.

[14] E. A. Carbonio, T. C. R. Rocha, A. Y. Klyushin, I. Pis, E. Magnano, S. Nappini, S. Piccinin, A. Knop-Gericke, R. Schlogl, T. E. Jones, *Chem. Sci.* **2018**.

[15] M.-L. Bocquet, A. Michaelises, in *Properties of Single Organic Molecules on Crystal Surfaces*, pp. 389-424.

[16] A. J. Nagy, G. Mestl, D. Herein, G. Weinberg, E. Kitzelmann, R. Schlögl, *J. Catal.* **1999**, *182*, 417-429.

[17] A. Holleman, N. Wiberg, E. Wiberg, et al., *Lehrbuch der Anorganischen Chemie*, Boston: De Gruyter, Berlin, **2008**.

[18] A. F. Wells, *Structural Inorganic Chemistry*, OUP Oxford, **2012**.

[19] M. E. Eberhart, M. M. Donovan, R. A. Outlaw, *Phys. Rev. B* **1992**, *46*, 12744-12747.

[20] The interaction of O_2 with silver, J. A. Bergwerff, **2003**

[21] T. E. Jones, S. Piccinin, C. Stampfl, *Mater. Chem. Phys.* **2013**, *141*, 14-17.

[22] W. M. Haynes, *CRC Handbook of Chemistry and Physics, 96th Edition*, CRC Press, **2015**.

[23] H. W. Richardson, in *Ullmann's Encyclopedia of Industrial Chemistry*, Wiley-VCH Verlag GmbH & Co. KGaA, **2000**.

[24] G. Rovida, F. Pratesi, M. Maglietta, E. Ferroni, *Surf. Sci.* **1974**, *43*, 230-256.

[25] V. I. Bukhtiyarov, A. Knop-Gericke, in *Nanostructured Catalysts: Selective Oxidations*, The Royal Society of Chemistry, **2011**, pp. 214-247.

[26] W.-X. Li, C. Stampfl, M. Scheffler, *Phys. Rev. B* **2003**, *68*, 165412.

[27] R. Reichelt, S. Günther, M. Rößler, J. Wintterlin, B. Kubias, B. Jakobi, R. Schlögl, *Phys. Chem. Chem. Phys.* **2007**, *9*, 3590-3599.

[28] D. Herein, A. Nagy, H. Schubert, G. Weinberg, E. Kitzelmann, R. Schlögl, in *Z. Phys. Chem. (Muenchen, Ger.), Vol. 197*, **1996**, p. 67.

[29] V. I. Bukhtiyarov, A. I. Nizovskii, H. Bluhm, M. Hävecker, E. Kleimenov, A. Knop-Gericke, R. Schlögl, *J. Catal.* **2006**, *238*, 260-269.

[30] V. I. Bukhtiyarov, I. P. Prosvirin, R. I. Kvon, *Surf. Sci.* **1994**, *320*, L47-L50.

[31] C. Rehren, G. Isaac, R. Schlögl, G. Ertl, *Catal. Lett.* **1991**, *11*, 253-265.

[32] B. Xinhe, D. Jingfa, *J. Catal.* **1986**, *99*, 391-399.

[33] G. W. Busser, O. Hinrichsen, M. Muhler, *Catal. Lett.* **2002**, *79*, 49-54.

[34] J.-W. Park, *J. Vac. Sci. Technol. A* **1997**, *15*, 292-293.

[35] H. J. Freund, D. W. Goodman, in *Handbook of Heterogeneous Catalysis*, **2008**.

[36] J. L. Solomon, R. J. Madix, J. Stöhr, *J. Chem. Phys.* **1990**, *93*, 8379-8382.

[37] T. E. Jones, R. Wyrwich, S. Böcklein, T. C. R. Rocha, E. A. Carbonio, A. Knop-Gericke, R. Schlögl, S. Günther, J. Wintterlin, S. Piccinin, *J. Phys. Chem. C* **2016**, *120*, 28630-28638.

[38] P. Harriott, *J. Catal.* **1971**, *21*, 56-65.

[39] R. Schlögl, S. B. Abd Hamid, *Angew. Chem. Int. Ed.* **2004**, *43*, 1628-1637; *Angew. Chem.* **2004**, *116*, 1656-1667

[40] J. C. Wu, P. Harriott, *J. Catal.* **1975**, *39*, 395-402.

[41] S. Cheng, A. Clearfield, *J. Catal.* **1985**, *94*, 455-467.

[42] J. K. Lee, X. E. Verykios, R. Pitchai, *Appl. Catal.* **1989**, *50*, 171-188.

[43] S. N. Goncharova, E. A. Paukshtis, B. S. Bal'zhinimaev, *Appl. Catal. A* **1995**, *126*, 67-84.

[44] J. E. van den Reijen, S. Kanungo, T. A. J. Welling, M. Versluijs-Helder, T. A. Nijhuis, K. P. de Jong, P. E. de Jongh, *J. Catal.* **2017**, *356*, 65-74.

[45] S. V. Tsybulya, G. N. Kryukova, S. N. Goncharova, A. N. Shmakov, B. S. Balzhinimaev, *J. Catal.* **1995**, *154*, 194-200.

[46] A. P. Fotopoulos, K. S. Triantafyllidis, *Catal. Today* **2007**, *127*, 148-156.

[47] D. C. Lim, I. Lopez-Salido, Y. D. Kim, *Surf. Sci.* **2005**, *598*, 96-103.

[48] Z. Qu, W. Huang, M. Cheng, X. Bao, *J. Phys. Chem. B* **2005**, *109*, 15842-15848.

[49] Y. Lei, F. Mehmood, S. Lee, J. Greeley, B. Lee, S. Seifert, R. E. Winans, J. W. Elam, R. J. Meyer, P. C. Redfern, D. Teschner, R. Schlögl, M. J. Pellin, L. A. Curtiss, S. Vajda, *Science* **2010**, *328*, 224-228.

[50] M. Boudart, *Adv. Catal.* **1969**, *20*, 153.

[51] J. R. Anderson, *Science Progress (1933-)* **1985**, *69*, 461-484.

[52] R. van Hardeveld, F. Hartog, *Adv. Catal.* **1972**, *22*, 75-113.

[53] R. Van Hardeveld, F. Hartog, *Surf. Sci.* **1969**, *15*, 189-230.

[54] J. C. Sharp, Y. X. Yao, C. T. Campbell, *J. Phys. Chem. C* **2013**, *117*, 24932-24936.

[55] J. A. Farmer, J. H. Baricuatro, C. T. Campbell, *J. Phys. Chem. C* **2010**, *114*, 17166-17172.

[56] J. H. Larsen, J. T. Ranney, D. E. Starr, J. E. Musgrove, C. T. Campbell, *Phys. Rev. B* **2001**, *63*, 195410.

[57] T. E. James, S. L. Hemmingson, T. Ito, C. T. Campbell, *J. Phys. Chem. C* **2015**, *119*, 17209-17217.

[58] T. E. James, S. L. Hemmingson, C. T. Campbell, *ACS Catal.* **2015**, *5*, 5673-5678.

[59] S. L. Hemmingson, T. E. James, G. M. Feeley, A. M. Tilson, C. T. Campbell, *J. Phys. Chem. C* **2016**, *120*, 12113-12124.

[60] C. T. Campbell, Z. Mao, *ACS Catal.* **2017**, *7*, 8460-8466.

[61] C. T. Campbell, J. R. V. Sellers, *Faraday Discuss.* **2013**, *162*, 9-30.

[62] X. Liang, J. Li, M. Yu, C. N. McMurray, J. L. Falconer, A. W. Weimer, *ACS Catal.* **2011**, *1*, 1162-1165.

[63] Z. Ma, S. Dai, in *Heterogeneous Gold Catalysts and Catalysis*, The Royal Society of Chemistry, **2014**, pp. 1-26.

[64] D. Yan, F. Wang, Y. Zhao, J. Liu, J. Wang, L. Zhang, K. C. Park, M. Endo, *Mater. Lett.* **2009**, *63*, 171-173.

[65] A. Cao, R. Lu, G. Veser, *Phys. Chem. Chem. Phys.* **2010**, *12*, 13499-13510.

[66] J. A. Farmer, C. T. Campbell, *Science* **2010**, *329*, 933.

[67] H. Kanoh, T. Nishimura, A. Ayame, *J. Catal.* **1979**, *57*, 372-379.

[68] J. K. Lee, X. E. Verykios, R. Pitchai, *Appl. Catal.* **1988**, *44*, 223-237.

[69] Y.-S. Yong, E. M. Kennedy, N. W. Cant, *Appl. Catal.* **1991**, *76*, 31-48.

[70] G. Busca, in *Metal Oxides: Chemistry and Applications*, CRC Press, **2005**, pp. 247-318.

[71] G. Busca, *Phys. Chem. Chem. Phys.* **1999**, *1*, 723-736.

[72] M. Ai, S. Suzuki, *J. Catal.* **1973**, *30*, 362-371.

[73] L. K. Hudson, C. Misra, A. J. Perrotta, K. Wefers, F. S. Williams, in *Ullmann's Encyclopedia of Industrial Chemistry*, Wiley-VCH Verlag GmbH & Co. KGaA, **2000**.

[74] R. Luque, A. Mariana Balu, J. Manuel Campelo, M. Dolores Gracia, E. Losada, A. Pineda, A. Angel Romero, J. Carlos Serrano-Ruiz, in *Catalysis: Volume 24, Vol. 24*, The Royal Society of Chemistry, **2012**, pp. 253-280.

[75] D. Zhao, J. Feng, Q. Huo, N. Melosh, G. H. Fredrickson, B. F. Chmelka, G. D. Stucky, *Science* **1998**, *279*, 548-552.

[76] A. Taguchi, F. Schüth, *Micropor. Mesopor. Mat.* **2005**, *77*, 1-45.

[77] S. Wang, *Micropor. Mesopor. Mat.* **2009**, *117*, 1-9.

[78] https://www.aerosil.com/sites/lists/RE/DocumentsSI/Technical-Overview-AEROSIL-Fumed-Silica-EN.pdf (2018-11-19)

[79] I. Chorkendorff, J. W. Niemantsverdriet, *Concepts of Modern Catalysis and Kinetics*, Wiley, **2017**.

[80] E. Marceau, X. Carrier, M. Che, O. Clause, C. Marcilly, in *Handbook of Heterogeneous Catalysis*, Wiley-VCH Verlag GmbH & Co. KGaA, **2008**.

[81] H.-J. Freund, G. Meijer, M. Scheffler, R. Schlögl, M. Wolf, *Angew. Chem. Int. Ed.* **2011**, *50*, 10064-10094; *Angew. Chem.* **2011**, *123*, 10242-10275.

[82] J. Libuda, I. Meusel, J. Hoffmann, J. Hartmann, L. Piccolo, C. R. Henry, H.-J. Freund, *J. Chem. Phys.* **2001**, *114*, 4669-4684.

[83] G. A. Somorjai, R. M. Rioux, *Catal. Today* **2005**, *100*, 201-215.

[84] T. Engel, G. Ertl, *J. Chem. Phys.* **1978**, *69*, 1267-1281.

[85] W. Luo, W. Hu, S. Xiao, *J. Phys. Chem. C* **2008**, *112*, 2359-2369.

2 Size effect of supported silver nanoparticles and clusters in CO oxidation influenced by their silver – oxygen interaction

2.1 Abstract

Supported Ag catalysts on silica and corundum have been synthesized applying an improved impregnation technique. The resulting Ag particle sizes can be divided into three categories concerning: (I) bulk-like, (II) nanoparticles of 1 – 6 nm and (III) *in-situ* created Ag clusters below 1 nm. Ag nanoparticles and bulk-like Ag are investigated concerning their pre-treatment dependence for CO oxidation showing that harsher pre-treatment conditions need to be applied for smaller particle sizes, based on their tendency to form Ag_2CO_3. A particle size effect for Ag in oxidation reactions is investigated using CO oxidation as a test reaction. The CO oxidation performance is increasing with decreasing particle size with Ag clusters showing the highest activity. Thermal desorption experiments combined with a novel method based on the adsorption of ethylene (C_2H_4) as sensor molecule are further used to discriminate the silver – oxygen (Ag–O) interaction strength of bulk-like Ag, Ag nanoparticles and Ag clusters, showing a distinct Ag–O chemistry for the three individual particle size regimes. By applying C_2H_4 breakthrough curve measurements the available Ag surface area is determined, which enables a correlation of Ag surface area and CO oxidation rate. Correlations of Ag–O interaction strength, Ag surface area and CO oxidation activity are discussed within the scope of this work.

2.2 Introduction

Supported Ag catalysts are used in several oxidation reactions such as of carbon monoxide[1] and methanol[2] or epoxidation of ethylene[3] and propene[4]. Since Ag is generally applied in a broad particle size (PS) regime, reliable studies on Ag PS effects are rare. The investigation of PS effects in catalysis is significantly important since they can influence the catalysts activity and selectivity due to changes in chemical characteristics caused by quantum-confinement effects for very small particles of only a few nanometers.[5-9] For the ethylene epoxidation reaction the influence of Ag PS in the regime of roughly 10 – 200 nm has already been well investigated with an overall consent that increasing Ag PS up to around 50 – 80 nm leads to more active but equally selective catalysts and that nanoparticles below 10 nm show a suppressed or decreased catalytic activity, following a volcano-type behavior.[5-7, 10-14] Only a limited number of studies were so far able to investigate the Ag PS regime below 10 nm concerning their catalytic activity in ethylene epoxidation[15], propylene epoxidation[16], carbon monoxide oxidation[17], or the interaction of Ag with oxygen[18] and various oxide support surfaces[19, 20]. However, so far the results allow no clear conclusion whether Ag nanoparticles are more or less active in oxidation reactions when decreasing its size down to a few nanometers or cluster size. In addition, the debate is influenced by the complex and unique chemistry of Ag and oxygen.[21-25]

The unique character of Ag compared to other metals is reasoned in the activation of oxygen on the surface and subsurface, while stable oxide phases at elevated temperatures and atmospheric pressure[26] are absent. This intriguing surface and subsurface silver – oxygen (Ag–O) chemistry explains why e.g. for the ethylene epoxidation reaction exclusively supported Ag catalysts are used. Further, a large variety of oxygen species like atomic, molecular, strongly bound, ionic, covalent, surface, subsurface, near defects, bulk-dissolved or surface-embedded oxygen have already been described and are still under debate.[27, 28] Nevertheless, most of these findings are made on single crystals, foils or powders,[29-32] since the synthesis and investigation of small and stabilized Ag nanoparticles is challenging.[33, 34]

The synthesis of well-defined small Ag nanoparticles with a narrow sizes distribution can be regarded as the first step to reliably facilitate PS effect investigations. Crucial parameters are the properties of the support material and the precursor material for Ag. For the suitability of the support, the specific surface area, structural stability and number and nature of functional groups are important. Sticking to the partial oxidation reaction of ethylene, a feature of the desired product ethylene epoxide is its high sensitivity to especially Lewis-acidic groups on the support surface.[35] This limits the number of possible supports, with corundum (α-Al_2O_3) and silica (SiO_2) as most promising candidates.[36] Besides, the low surface acidity of α-Al_2O_3 is based on the overall low number of functional groups due to its low specific surface area of usually below 5 $m^2 \cdot g^{-1}$.[37] For a successful synthesis and stabilization of nanoparticles, however, high surface area supports are needed. The necessary chemical inertness of the supports also limits the use of metal-support interactions, which is a common strategy for metal nanoparticle stabilization.[38-42] Flame hydrolyzed silica exhibits a high concentration of surface OH-groups paired with a high hydrophilicity, a moderate surface acidity and high structural as well as textural stability and is therefore identified as suitable support material for the synthesis of small nanoparticles and applied as support material in this work.

As precursor materials, among Ag carbonates, sulfates, acetates, oxalates, lactates, succinates, glycolates and multiple amine systems[43, 44], Ag nitrate ($AgNO_3$) offers the useful ability of melting at 210 °C before its decomposition at 440 °C.[45] This enables a rather controlled development of Ag nanoparticle by thermal treatments. Additionally, $AgNO_3$ dissolves easily in water, thus, being a suitable impregnation solution for hydrophilic silica. The OH-group rich surface of SiO_2 enables Ag^+ ions to undergo ion exchange reactions[46], thereby being distributed and stabilized over the complete support surface area leading to metallic nanoparticles below 6 nm, which was, to the best of our knowledge, so far only achieved on e.g. very acidic and porous supports like Zeolites.[47] Furthermore, a partial calcination can be used to *in-situ* create Ag clusters during reaction conditions, which represents a novel approach in the course of the presented research.

In summary, this work deals for the first time with the investigation of the Ag–O chemistry for a series of silica supported Ag catalysts with solely Ag nanoparticles below 6 nm down to cluster sized Ag. All samples

were thoroughly analyzed by multiple techniques including powder X-ray diffraction (PXRD), thermogravimetric analysis (TGA) coupled to evolved gas analysis (EGA), scanning electron microscopy with energy dispersive X-ray detector (SEM/EDX) and transmission electron microscopy (TEM). We apply the oxidation of carbon monoxide as a test reaction for the activation of oxygen[48] and a combination of thermal desorption spectroscopy (TDS), microcalorimetry and ethylene adsorption (as probe molecule) for a qualitative and quantitative assessment of the Ag–O interaction. For comparison reasons, a conventional Ag/α-Al_2O_3 sample is analyzed.

2.3 Experimental section

Synthesis of Ag/SiO_2 and Ag/α-Al_2O_3. For the silica supported catalysts SiO_2 (Aerosil 300, DEGUSSA, hydrophilic fumed silica powder, primary particles: spherical, 7 – 40 nm, no porosity) was transferred into a round-bottom flask. The flask was attached to a vacuum evaporator, which was modified to a dedicated impregnation setup, to achieve a controlled distribution on the support under low vacuum. The support was subsequently outgassed under a pressure of 60 mbar at room temperature for 10 min, followed by impregnation under 60 mbar under constant stirring and rotation of the flask. Aqueous $AgNO_3$ ($AgNO_{3(aq)}$) was used according to 5 wt.-% Ag loading (labeled as Ag5/SiO_2) with a drop rate of 30 drops per minute. The impregnated support was dried for at least 12 h at 110 °C in air. The dried material was pressed at $5 \cdot 10^4$ N·cm^{-2} for 1 min and transferred into a 100 – 200 µm sieve fraction. The subsequent calcination was performed in a rotating tube furnace with a constant flow of 21 % O_2 in Ar (300 ml·min^{-1}) with a heating rate of 2 °C·min^{-1} to 400 – 600 °C with 0 – 3 h dwell time, labeled as X/Y with X = temperature and Y = dwell time. The sample was finally cooled down to room temperature under the same gas feed.

The amount of H_2O needed for impregnation was determined by adding the exact amount for which no excess H_2O was visible on the support and no clumping occurred. This volume is referred to as "solvent capacity volume" (SCV) and describes the amount of solvent needed to fill the pores and to cover the complete surface of the material. Thereby, it enables a good distribution of the solved $AgNO_{3(aq)}$ on the available surface area of the support. In the case of SiO_2 Aerosil® 300 with a specific BET surface area of 328 m^2·g^{-1} the necessary amount of H_2O to reach the SCV was determined to 1.43 ml·g^{-1}.

For the synthesis of a reference sample, 15.5 wt.-% Ag was loaded on corundum (α-Al_2O_3) with a specific surface area of ~1.0 m^2·g^{-1} using an Ag oxalate based precursor according to patent literature[37], labeled as Ag15/α-Al_2O_3. In short, a silver oxalate-ethylenediamine complex was synthesized by mixing oxalic acid dehydrate, ultrapure water, KOH and $AgNO_3$ to form a silver oxalate complex which is subsequently reacted with the complexing agent ethylenediamine. The α-Al_2O_3 support was then impregnated with the silver oxalate-ethylenediamine solution followed by a calcination under air.

CO oxidation was performed in a self-constructed catalytic reactor setup equipped with an on-line gas analyzer (X-STREAM XE, Emerson/Rosemount) with an infrared and a paramagnetic sensor, for the simultaneous quantification of oxygen, carbon monoxide, carbon dioxide and water. CO gas was purified using a carbonyl remover consisting of a tube filled with inert silicon carbide heated up to 300 °C. The He gas passed a water and oxygen filter patron (AIR LIQUIDE). A quartz plug-flow U-tube reactor was loaded with 30 mg of the Ag5/SiO_2 catalyst (100 – 200 µm sieve fraction) diluted with 250 mg inert SiC (250 – 355 µm sieve fraction) and surrounded by about 40 mg quartz wool on each side. In the case of Ag15/α-Al_2O_3 catalysts, three times more mass had to be loaded to reach the same catalyst volume and space velocity. CO oxidation was performed with 96 vol.-% He, 2 vol.-% CO and 2 vol.-% O_2 at 100 ml·min^{-1}. All samples were pre-treated in 21 % O_2 in He at a flow of 100 ml·min^{-1} at a certain temperature and dwell time. The catalytic oxidation was tested in a three-cycle test with heating to 250 °C with 2 °C·min^{-1} and cooling to 30 °C between each cycle. For excluding diffusion limitation effects, the samples were analyzed by comparing the temperatures for 10 % CO conversion ($T_{10\%}$ or Temperature $X_{CO,10\%}$).

The reaction order was determined by pre-treating the samples at 300 °C for 3 h in 21 % O_2 in He and one subsequent CO cycle to 250 °C. After that the samples were kept constantly at 100 °C with a variation of O_2 or CO partial pressure.

Powder X-ray diffraction (PXRD) patterns were recorded using a BRUKER AXS D8 ADVANCE II THETA/THETA diffractometer in Bragg-Brentano geometry using Ni filtered Cu $K_{\alpha 1+2}$ radiation and a position sensitive LynxEye silicon strip detector. The sample powder was filled into the recess of a cup-shaped sample holder, the surface of the powder bed being flush with the sample holder edge (front loading). The resulting diffractograms were analyzed by full pattern fitting using the TOPAS software[49] to extract lattice parameters and crystallite sizes.

N_2 physisorption was performed in a QUANTOCHROME AUTOSORB-6-B-MP machine after degassing a specific amount (500 mg for α-Al_2O_3, 30 mg for SiO_2) of the sample at 150 °C for 15 h. The resulting isotherms were recorded at the temperature of liquid nitrogen. Calculation of the surface area was performed according to the equation of Brunauer, Emmet and Teller (BET equation).[50]

Thermogravimetric analysis / evolved gas analysis (TGA-EGA) was conducted using a STA 449 C Jupiter thermoanalyzer (NETZSCH) under oxidative (21 % O_2 in Ar) or inert (Ar) gas atmosphere with a total flow of 100 ml·min^{-1}. The sample was heated up with 2 °C·min^{-1} to 500 – 600 °C without or with 1 h dwell time. The setup was connected to a quadrupole mass spectrometer (QMS200 Omnistar, BALZERS) for evolved gas analysis *via* a quartz capillary heated to 40 °C. All data were analyzed using the NETZSCH Proteus Thermal Analysis software package (Version 6.10).

Scanning transmission electron microscopy (STEM) imaging was performed using a double Cs corrected JEM-ARM200CF (JEOL) operated at 200 kV and equipped with ADF (annular dark-field) and BF (bright-field) detectors. Samples were prepared by direct deposition of dry powder onto a QUANTIFOIL Au holey grid. For the resulting histograms, the diameter of 1000 particles was measured for each sample.

Scanning electron microscopy (SEM) was performed on a HITACHI S-4800 equipped with a field emission gun and YAG-BSE (backscattered electrons) and **energy dispersive X-ray** (EDX) detectors. The system was operated at a working distance of 10 mm applying 10 kV.

C_2H_4 adsorption measurements were performed using a temporal analysis of products approach at atmospheric pressure (atmTAP) at 40 °C using breakthrough curve measurements with a high-speed transient reactor.[51] A plug-flow reactor was loaded with a catalyst sample with a mass of 100 mg. The sample was pre-treated at 300 °C for 3 h under a constant flow of 21 % oxygen in He, after which the reactor was cooled slowly to the desired temperature under the same gas flow. Before the C_2H_4 breakthrough curve was measured, the gas flow is first changed to pure He (100 ml·min^{-1}) to completely purge the gas-phase oxygen from the reactor. Then, the gas composition was instantly switched to 3.93 mbar C_2H_4 in He. Besides C_2H_4, a small fraction of Ar was also present in the feed in order to determine the mean reactor residence time of a non-adsorbing reference species. The C_2H_4 and Ar concentrations at the reactor exit were monitored using a mass spectrometer. For each sample the adsorption measurement was repeated three times. In between those measurements, C_2H_4 was thoroughly desorbed by ramping the temperature to 230 °C under 21 % O_2 in He and subsequent cooling to 40°C.

Microcalorimetry was performed in a HT1000 (RT – 1000 °C) and MS70 (RT – 100 °C) Tian-Calvet calorimeter (SETARAM) combined with a custom-designed high vacuum and gas dosing apparatus. The sample was placed in batch reactor. C_2H_4 adsorption experiments were performed after cleaning the samples at 300 °C for 3 h in synthetic air (200 mbar O_2) or additional reduction by CO oxidation feed (2 % CO, 2 % O_2) followed by stepwise dosing of around 0.01 – 4.00 mbar C_2H_4 at 40 °C. Prior to readsorption of C_2H_4 the sample was treated at 10^{-8} mbar to desorb reversible bound C_2H_4 and free C_2H_4 adsorption sites. Oxygen adsorption experiments were performed at 200 °C after (I) a pre-treatment of 600 °C at 10^{-8} mbar for 1 h and (II) a proximate reduction at 400 °C for 1 h combined with 10 mbar H_2.

Thermal desorption spectroscopy (TDS) was applied for the temperature programmed desorption of oxygen. Therefore, a self-constructed setup which enables the testing of powder samples was used. The setup was equipped with mass flow controllers, an IR-light furnace (BEHR IRF 10) and a mass spectrometer (PFEIFFER VACUUM QME 200). The powder sample was placed on a small quartz-glass boat which is placed in a quartz tube (inner diameter of 14 mm, outer diameter of 20 mm, length of 450 mm) located inside of

furnace and connected to the system using Ultra Torr vacuum fittings. Prior to the desorption experiment the samples were pre-treated at 1 bar in 25 % O_2 in Ar at a flow of 100 ml·min^{-1} for 12 h at 210 °C, which cleaned the surface of the sample and saturated the Ag with oxygen (surface and bulk). The gases were detected using the mass spectrometer leak valve. Afterwards the system was stepwise brought to 9·10^{-7} mbar and directly connected to the mass spectrometer. The desorption experiment was conducted at a heating rate of 25 °C·min^{-1} up to 700 °C. All masses and the temperature were monitored online.

Inductive coupled plasma – optical emission spectroscopy (ICP-OES) was used to determine the Ag loading of the catalysts. Therefore, the sample was solubilized using LiF, nitric acid and water at 230 °C, diluted with water and analyzed with a PERKIN ELMER ICP OES Optima 8300.

2.4 Results and discussion

Table 1. Overview of investigated Ag (pre-)catalysts with nominal (nom) and experimentally (exp) determined Ag loading (SEM-EDX, ICP-OES and PXRD), BET support surface area (SA_{BET}), median Ag particle size (STEM), Ag domain size (PXRD) and internal FHI number

sample	Calc. conditions [°C·h^{-1}]	Ag loading [wt.-%] (nom)	Ag loading [wt.-%] (exp)	Support SA_{BET} [m^2·g^{-1}]	Median Ag particle size [nm]	Ag domain size [nm]	FHI #
$AgNO_3/SiO_2$	-	5	2.5[*1] 4.3[*2]	328			27150
$Ag5/SiO_2$	400/1	5	2.6[*1]	328	2.0	n/a	27127
	400/3		-		-	n/a	27128
	500/1		3.1[*1]		2.4	n/a	27130
	500/3		-		-	n/a	27131
	600/1		3.2[*1] 4.5[*2]		2.3	6.1±0.9	27133
	600/3		-		-	6.3±0.9	27134
Ag15/ α-Al_2O_3	280/0.2	15.5	29.1[*1] 12.4[*2] 14.0[*3]	~1.0	~30 and ~200	39.4	26630

[*1]: SEM-EDX, [*2]: ICP-OES, [*3]: PXRD full pattern fitting

2.4.1 Sample preparation and characterization

All samples (see Table 1) were synthesized by impregnation following an incipient wetness approach, while the solvent capacity volume (SCV) was determined experimentally (details see experimental part). For the impregnation, a modified vacuum evaporator was used. Benefits are the use of low vacuum (60 mbar), rotation of the flask and controlled addition of impregnation solution, all occurring in a closed system. This enables a superior distribution of the impregnation solution compared to conventional impregnation techniques. An important criterion for Ag nanoparticles with a narrow PS distribution is the properly chosen surface area of the support. Figure 7 shows representatively the ratio between the surface area, the PS of Ag

and the interparticle distance, which determines the sintering stability of the formed particles (nearby the Ag support interaction) for a support loaded with 5 wt.-% Ag. It reveals that for a good stabilization of nanoparticles below 2 nm support surface areas of already a few hundred $m^2 \cdot g^{-1}$ are necessary. For this reason hydrophilic flame hydrolyzed SiO_2 (here: Aerosil 300) was selected since it offers a suitable BET surface area of 328 $m^2 \cdot g^{-1}$. Thereby, it theoretically enables the synthesis and stabilization of nanoparticles consisting of less than 200 atoms down to even smaller clusters that consist of less than 50 Ag atoms. In the following, the samples are named according to their Ag loading in wt.-% and the chosen support, i.e. 5 wt.-% Ag on silica as $Ag5/SiO_2$. Calcination conditions are labeled as X/Y (X = temperature, *T* in °C; Y = dwell time, *t* in h), i.e. $Ag5/SiO_2$ 400/1 for a calcination at 400 °C with 1 h dwell time. Pre-treatment conditions for catalytic or analytical tests are given with the same *T*/*t* notation. An overview of relevant samples and their corresponding characteristics is given in Table 1.

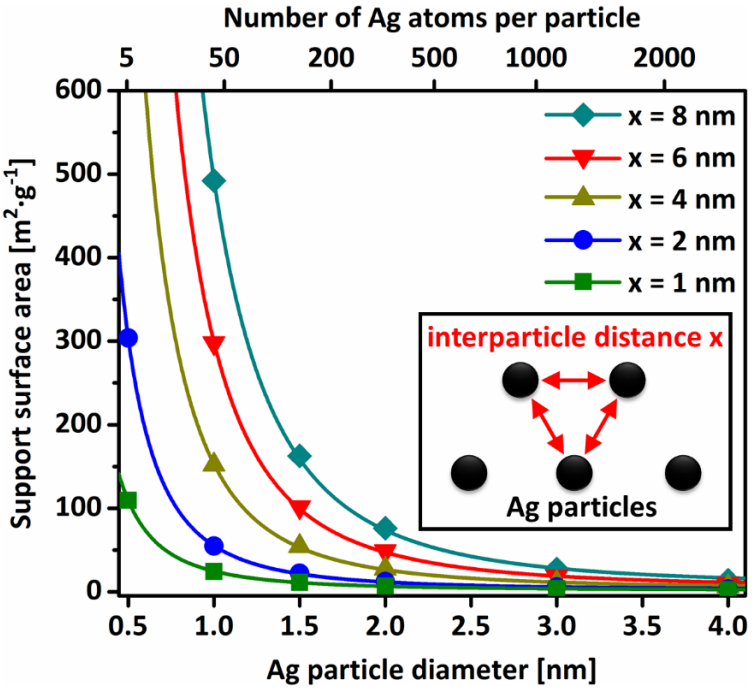

Figure 7. Required support surface area per gram support versus Ag nanoparticle size for different interparticle distances x of 1, 2, 4, 6 and 8 nm. Calculations were performed for 5 wt.-% Ag loading. (no wetting assumed)

To identify proper calcination conditions, a $AgNO_3/SiO_2$ precursor was analyzed with TGA-EGA upon thermal treatment (Figure 8A). After desorbing the physisorbed H_2O, a first NO release is detected at 160 °C with a NO evolution maximum at 220 °C, being in good agreement with reported 210 °C[45] for the $AgNO_3$ melting point. It is assumed that $AgNO_3$ nano-islands are formed, which are size-determining for the final Ag particles and clusters. Upon further calcination, $AgNO_3$ decomposes to Ag^0 which is again indicated by a strongly increased NO signal with an overall maximum at 390 °C. The detected mass loss of 3.33 % during

NO evolution (m/z = 30, 150 °C – 500 °C) is slightly higher than the theoretical weight loss of 2.87 %, explained by additional H_2O evolution (m/z = 18, 25 – 465 °C).

Based on the TGA-EGA of differently calcined samples (Figure 8B), a remaining amount of 14 % $AgNO_3$ is calculated after a calcination temperature of 400 °C without dwelling (400/0) and 6 % for 400 °C for 1 h dwelling (400/1). At calcination temperatures of 500 °C and higher no remaining NO evolution was detected. Based on these results (TGA-EGA, Figure 8A+B), a set of samples with three different calcination temperatures (400 °C, 500 °C and 600 °C) and two different dwell times (1 h and 3 h) at each temperature was synthesized. The comparably mild calcination temperature of 400 °C (with 6 % residual $AgNO_3$) is selected since any thermally induced sintering should be avoided.

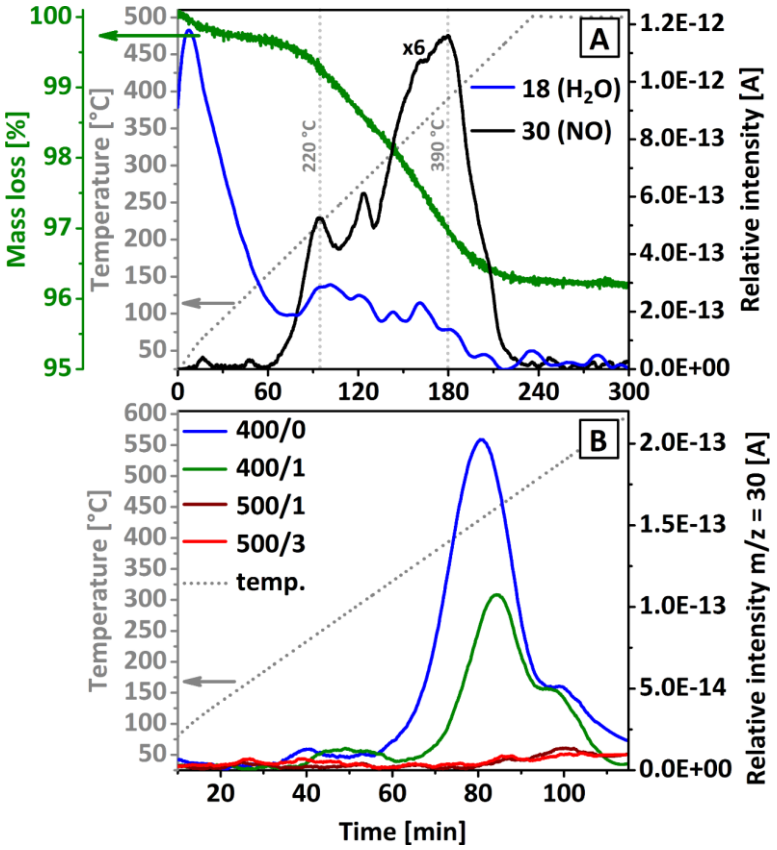

Figure 8. TGA-EGA of dried $AgNO_3/SiO_2$ (5 wt.-%) precursor (A) with a heating rate of 2 °C·min^{-1} to 500 °C under synthetic air in a total flow of 100 ml·min^{-1}. Mass signal m/z = 18 and m/z = 30 (amplified times six for improved visibility) corresponds to the evolution of H_2O and NO, respectively. Catalysts $Ag5/SiO_2$ (B) after calcination at 400 °C for 0 h (400/0), 400 °C for 1 h (400/1), 500 °C for 1 h (500/1) and 500 °C for 3 h (500/3) was investigated by comparing m/z = 30 evolutions.

For an experimental analysis of the Ag loading (Table S4) ICP-OES was performed. The Ag loading for the $AgNO_3/SiO_2$ precursor was determined to 4.3 wt.-%, being in very good agreement with the results for sample $Ag5/SiO_2$ calcined at 600/1 of 4.5 wt.-%. Both values are, in addition, very near to the nominal loading of 5 wt.-%. Supplementary, EDX analysis was performed, resulting in a loading for the $AgNO_3/SiO_2$ precursor

and the calcined Ag5/SiO_2 catalysts in the range from 2.48±0.77 – 3.23±0.33 wt.-%. Within the standard deviation of the measurements, all samples show the same wt.-% Ag loading. The detected loadings are smaller than the theoretical one and the ones detected by ICP-OES. This can be attributed to the size of the Ag particles, leading to a weakly detectable signal by the EDX detectors. It can be explained by the excitation bulb of the incoming electron beam, whereby less excitation is expected for smaller particles because the main excitation occurs in the support material. However, all Ag5/SiO_2 samples derived from the same precursor batch $AgNO_3$/SiO_2 and therefore are expected to have the same Ag loading.

For an overview of the resulting Ag PS after impregnation and calcination, STEM analysis was performed for the $AgNO_3$/SiO_2 precursor dried at 110 °C for 12 h without calcination, and additionally Ag5/SiO_2 samples calcined at conditions of 400/1 and 600/1. After drying, the $AgNO_3$/SiO_2 shows a uniform size distribution with Ag PS up to 4.6 nm and a median value of 1.8 nm (Figure 9A). Those nanoparticles show a d-spacing of the Ag 111 lattice plane of 2.40 Å (Figure S22), being in good agreement with the literature value of 2.36 Å.[52] Besides, the inset of Figure 9A (red box) presents a higher magnification image of the precursor sample, showing single Ag atoms that are well distributed over the support surface, which are likely atomically dispersed Ag^+ species that formed after ion-exchange reactions on the silica support. A representative STEM image for sample Ag5/SiO_2 400/1 is shown in Figure 9B with the corresponding PS distribution (histogram). The Ag particles are well distributed over the support without atomic species visible and a median PS of 2.0 nm, with a standard deviation (SD) of 0.71 nm. In comparison, the Ag5/SiO_2 600/1 sample exhibits a median PS of 2.3 nm (SD = 0.72 nm, see Figure 13B). In addition, a very narrow size distribution is obtained without Ag particles larger than 5.8 nm.

Comparable studies with $AgNO_{3(aq)}$ impregnations on SiO_2[53] led to increased Ag PS and broad size distributions, which emphasizes the advantage of the developed synthesis technique. As direct result of the higher calcination temperature (from 400 to 600 °C) the amount of Ag clusters (< 1nm) is reduced from 6.4 % to 1.7 %. The impact of the calcination temperature on the Ag PS below 1 nm is insignificant, which underlines the high temperature stability of the synthesized Ag particles.

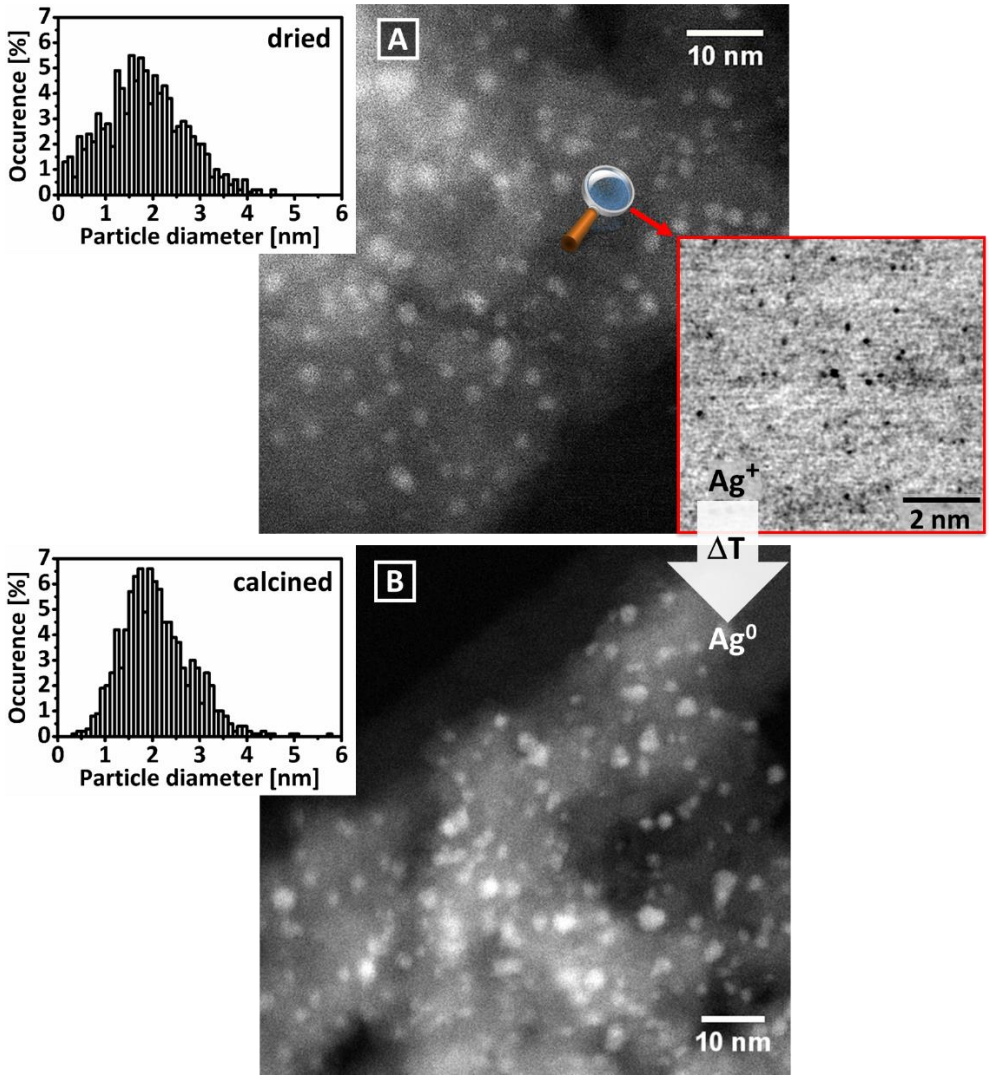

Figure 9. STEM ADF image of the catalyst precursor $AgNO_3/SiO_2$ (A). Inset of (A) shows a higher magnification image of the same sample (red box), which was inverted and processed using a Gaussian blur (original image see Figure S22). $Ag5/SiO_2$ catalyst calcined at conditions of 400/1 is shown in (B). Bright spots correspond to Ag particles. PS distribution insets are shown on the top left.

For all samples PXRD analysis was performed (Figure 10). PXRD provides integral information about e.g. the phase compositions and no remaining $AgNO_3$ or Ag_2O as by-phase was detected. The broad diffuse signal between 16 – 40° 2Θ is assigned to amorphous SiO_2. For samples calcined at 400 °C the present Ag nanoparticles are XRD amorphous, which is a result of the small Ag domains. With increasing calcination temperatures the Ag reflections start to appear and get well visible for applied 600 °C. For the samples $Ag5/SiO_2$ 600/1 and 600/3 also the volume-weighed mean domain sizes and lattice parameter can be extracted from full pattern analysis, with 6.1±0.9 nm and 4.089±0.012 Å for 600/1 and 6.3±0.9 nm and 4.090±0.009 Å for 600/3. Thereby, the domain sizes are in good agreement with the results from STEM analysis showing only particles below 5.8 nm for $Ag5/SiO_2$ 600/1. Within the uncertainty of the fitted results, all lattice parameters are in agreement with the reported reference of 4.086 Å[54] for Ag^0. Besides, a diffuse signal at 37 – 39° 2Θ assigned to Ag_2CO_3 is visible. With a decreasing calcination temperature, the Ag_2CO_3

moieties are increasing, further, as a function of time (18 weeks, absence of light) the Ag_2CO_3 is continuously growing and crystallizing (Figure S23).

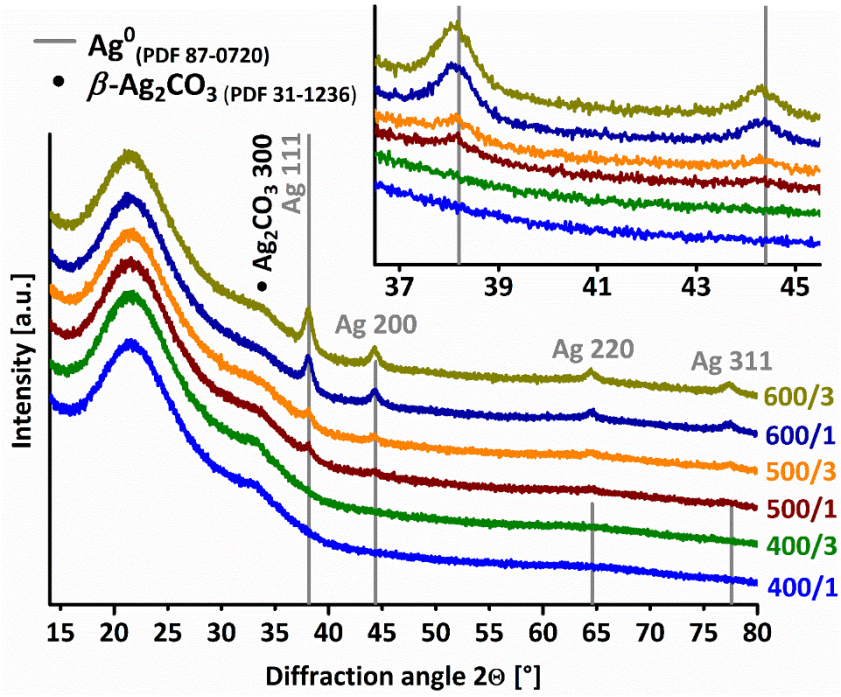

Figure 10. PXRD of Ag5/SiO_2 calcined at 400 °C, 500 °C and 600 °C with 1 h and 3 h dwell time. Inset represents a zoom of the Ag 111 and Ag 200 reflections.

For this study an α-Al_2O_3 supported Ag reference sample was synthesized and labeled Ag15/α-Al_2O_3. In contrast to the applied SiO_2 support, $AgNO_3$ based impregnation on α-Al_2O_3 (experimental details are described in the supporting information) led to the opposite effect resulting on large particles with a broad size distribution, ranging from nanoparticles of only a few nanometers up to particles of several micrometers (Figure S24 and Figure S25). Therefore, according to current patent literature[37], a Ag oxalate source was used for the synthesis of a reference sample. This approach led to well dispersed Ag nanoparticles of 100 – 300 nm with a few particles being in the range of 20 – 40 nm (STEM analysis, Figure S26), but without particles < 20 nm. Therefore, the Ag oxalate based Ag15/α-Al_2O_3 sample can be applied as a reference for larger Ag particles[37] and, based on the Ag PS, can be circumscribed from Ag5/SiO_2 samples with Ag particles < 6 nm. The quantitative XRD analysis using the Rietveld method determined the Ag loading for Ag15/α-Al_2O_3 to 14.0 wt.-%, being in good agreement with nominal loading of 15.5 wt.-% and the results from ICP-OES of 12.4 wt.-%. With STEM-EDX, however, the Ag loading is overestimated (29.1 wt.-%) since the reverse effect as observed for the silica supported Ag nanoparticles occurs, i.e. the main excitation occurs in the Ag particles due to their larger size.

Further, the crystalline domain size of Ag15/α-Al_2O_3 was calculated to 39.4 nm (Figure S27) with a calculated lattice parameter of 4.08603±0.00009 Å, being in very good agreement with the reference value.[54]

With STEM analysis additional Ag PS of 100 – 300 nm were observed (Figure S26). It seems reasonable that these Ag particles consist of multiple Ag domains, very likely formed by sintering of smaller Ag particles of around 40 nm as calculated from PXRD, probably during the calcination procedure. Furthermore, PXRD analysis revealed no or an insignificant (XRD amorphous) amount of Ag_2CO_3 even after six months. This might be interpreted as strong tendency of Ag nanoparticles to activate and stabilize oxygen since formally, the Ag_2CO_3 formation is based on the reaction of Ag_2O with CO_2. The stabilized oxygen species on Ag nanoparticles below 6 nm, in contrast to big or bulk-like Ag particles, being larger than 20 nm (smallest size detected *via* STEM analysis), might be of rather oxidic character, without forming any Ag_2O phase. This gives a first indication about the nature and reactivity of Ag nanoparticles and a pronounced size effect.

2.4.2 Catalytic testing

Prior to testing the catalytic performance in the oxidation of CO to CO_2, it is indispensable to proper activate the catalysts. As observed by PXRD, Ag nanoparticles show a strong tendency to form Ag_2CO_3. During the activation phase, the surface of the active material is cleaned by e.g. the decomposition of unwanted species like carbonates and oxides, potentially blocking reaction sites. Due to the decomposition temperature of Ag_2CO_3 at 175 °C – 225 °C[55] and Ag_2O of around 200°C[45], the lowest meaningful pre-treatment temperature is 200 °C. All pre-treatments were performed with 21 % O_2 in He. For the following CO oxidation test a three-cycle run is applied, whereby the 1st cycle is used as additional pre-treatment step for cleaning the Ag particle surface and to reduce remaining $AgNO_3$. The 2nd and 3rd cycle represent the actual CO oxidation performance test. In addition, the 3rd cycle provides also information about the stability of the catalysts.

To investigate the influence of the pre-treatment conditions on the catalytic performance, the catalysts were activated at 200 °C for 12 h (200/12), 230 °C for 3 h (230/3), 300 °C for 3 h (300/3) or 300 °C for 12 h (300/12). For a direct comparison of the catalytic activity the temperatures reaching 10 % CO conversions are identified ($T_{10\%}$). With a stepwise increase of the temperature and dwell time, all catalysts tested were significantly increasing in their catalytic performance. Figure 11 shows the impact on the $T_{10\%}$ of the Ag5/SiO_2 400/1 and 600/1 catalysts for three different pre-treatment conditions (all $T_{10\%}$ values are listed in Table 2)

The 400/1 sample shows a huge dependency of the $T_{10\%}$ values upon different pre-treatments. In particular, the first catalytic cycle deviates from the second and third cycle. This effect is more significant for the milder pre-treatment (230/3 ΔT_{c1-c3} = 91 °C, 300/3 ΔT_{c1-c3} = 27 °C), which is most likely explained by the transformation of the residual $AgNO_3$ (around 6 %) to catalytically active Ag^0. The activity of the second and third cycle of sample 400/1 is thereby much higher for all pre-treatments (lower $T_{10\%}$ values) except for 300/12. Here, the pre-treatment leads already to first deactivation and sintering events for the 400/1 sample which can be seen in the increased $T_{10\%}$ from cycle one to cycle two. Luo *et al.*[56] have already shown that for

unsupported 2 nm sized Ag nanoparticles the corresponding Tammann temperature is below 100 °C, which makes sintering for the present silica supported nanoparticles in a comparable size range a likely deactivation mechanism. The 600/1 sample shows, upon cycling within a given pre-treatment of at least 230 °C, stable $T_{10\%}$ values ($\Delta T_{c1\text{-}c3} = 1 - 4$ °C), supporting a complete calcination (no $AgNO_3$, Figure 8B). The higher activity with higher pre-treatment temperatures can be ascribed to more complete surface purification (e.g. from Ag_2CO_3) strongly emphasizing the importance of a dedicated pre-treatment for Ag catalysts, especially for Ag nanoparticles. This interpretation is supported by the behavior of the aged and Ag_2CO_3-rich $Ag5/SiO_2$ samples (stored for 18 weeks, Figure S23), which show after a pre-treatment at 300/12 a reduced activation upon cycling (Figure S28). For the aged sample 400/1 the first cycle after 300/12 pre-treatment is additionally needed to purify the sample from Ag_2CO_3 leading to further activation of the catalyst.

Also, the effect of a pronounced oxygen desorption upon higher pre-treatment temperature should be taken into consideration. It is well-known in CO oxidation that catalysts can also be "poisoned" by adsorbed atomic oxygen (O_{ad}). Thereby, CO is prohibited to adsorb in close proximity to O_{ad}, which is a prerequisite for a successful oxidation process. The desorption of O_{ad} frees adsorption sites now also available for CO.[48] This would lead to an increased rate for CO oxidation upon harsher pre-treatment conditions and is in agreement with the results for $Ag5/SiO_2$ catalysts. However, since the fresh 400/1 sample shows first sintering effects at conditions of 300/12, for the following tests and quantifications the pre-treatment conditions are fixed to conditions of 300/3 as suitable upper limit, since it results in the highest activity without deactivation.

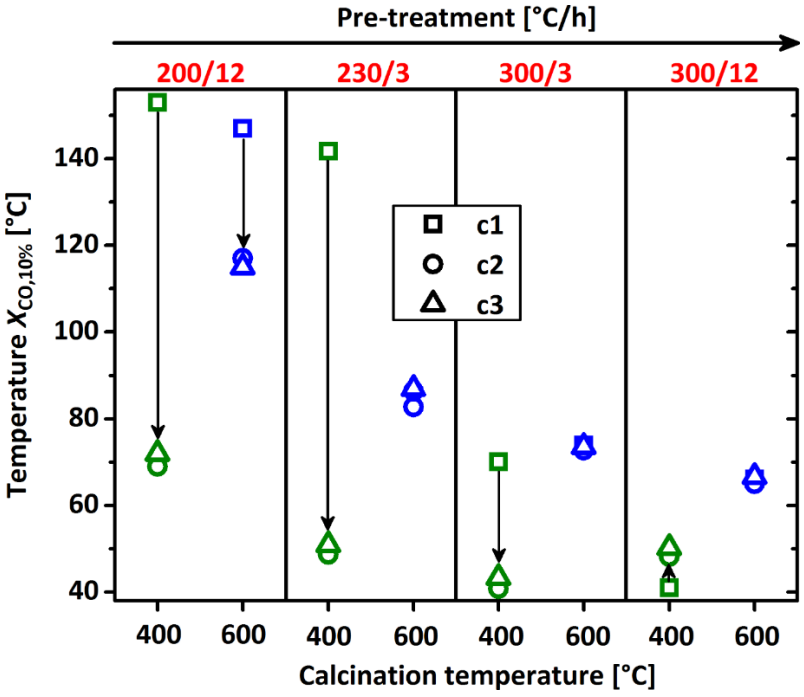

Figure 11. Temperatures needed for 10 % CO conversion ($X_{CO,10\%}$) for cycles one to three (c1 – c3) for $Ag5/SiO_2$ catalysts calcined at 400 °C and 600 °C with 1 h dwell for pre-treatment conditions 200/12, 230/3, 300/3 and 300/12 (see Table 2).

For comparison, reference Ag15/α-Al_2O_3 was additionally measured in CO oxidation after 300/3 pre-treatment (Table 2 and Figure S29). The catalyst shows a stable performance with $T_{10\%}$ values of 137 °C for cycles two and three. Although the sample contains the threefold amount of Ag, it is almost half as active as sample Ag5/SiO_2 600/1, underlining the high activity of Ag5/SiO_2 catalysts.

Table 2. Overview of temperature for 10 % CO conversion ($T_{10\%}$) for different pre-treatments for cycle one to three for catalysts Ag5/SiO_2 calcined at 400 °C and 600 °C for 1 h and reference Ag15/α-Al_2O_3

pre-treatment conditions	cycle number	$T_{10\%}$ [°C]		
		Ag5/SiO_2 400/1	Ag5/SiO_2 600/1	Ag15/α-Al_2O_3
200/12	1	153	147	-
	2	69	117	-
	3	72	115	-
230/3	1	142	83	-
	2	48	86	-
	3	51	87	-
300/3	1	70	74	132
	2	41	73	137
	3	43	74	137
300/12	1	41	66	-
	2	48	65	-
	3	50	67	-

To gain further insights into the activation procedure of the 400/1 sample during cycle one, respectively between cycle one and two, its CO oxidation performance, tested for three cycles (c1 – c3), is compared to the non-calcined $AgNO_3/SiO_2$ precursor. Figure 12A shows the light-off curves of the precursor, dried at 110 °C and pre-treated at conditions of 300/3. A distinct discrepancy between the first and second cycle is observed, accompanied by a pronounced activation of the sample. The catalyst ignites as soon as $AgNO_3$ starts to decompose (see also Figure 8A). After the pre-treatment (300/3) obviously only a minor fraction of $AgNO_3$ is converted/thermolyzed to Ag^0 nanoparticles, explaining the low conversion for the beginning of the first cycle. The effect of an increased activity is, strongly weakened, but still visible for the third cycle. The activation of the precursor within the cycles is also monitored by a shift of the $T_{10\%}$ values (indicated in Figure 12 as dashed line). A direct comparison to the light-off curves of the 400/1 sample in Figure 12B emphasizes a similar activation behavior of these samples. As a consequence, the activation of the 400/1 sample (with 6 % $AgNO_3$) within the cycling is coupled to the pre-treatment conditions and is explained by the transformation of the residual $AgNO_3$ to Ag^0 particles or clusters. Further, stable $T_{10\%}$ values of the 400/1 sample for the second and third cycle after milder (230/3, 300/3) pre-treatment evidences a complete conversion of the $AgNO_3$ within the first cycle (Figure 11). The harsh pre-treatment of 300/12 resulted already in a $AgNO_3$-free catalyst, indicated by the absence of any activation upon cycling. Since after calcination at conditions of 600/1 no residual $AgNO_3$ is detected (Figure 8B) no activation between the first

and third cycle is observed after the 300/3 pre-treatment (Figure 11 and Figure S30), which underlines the described correlation.

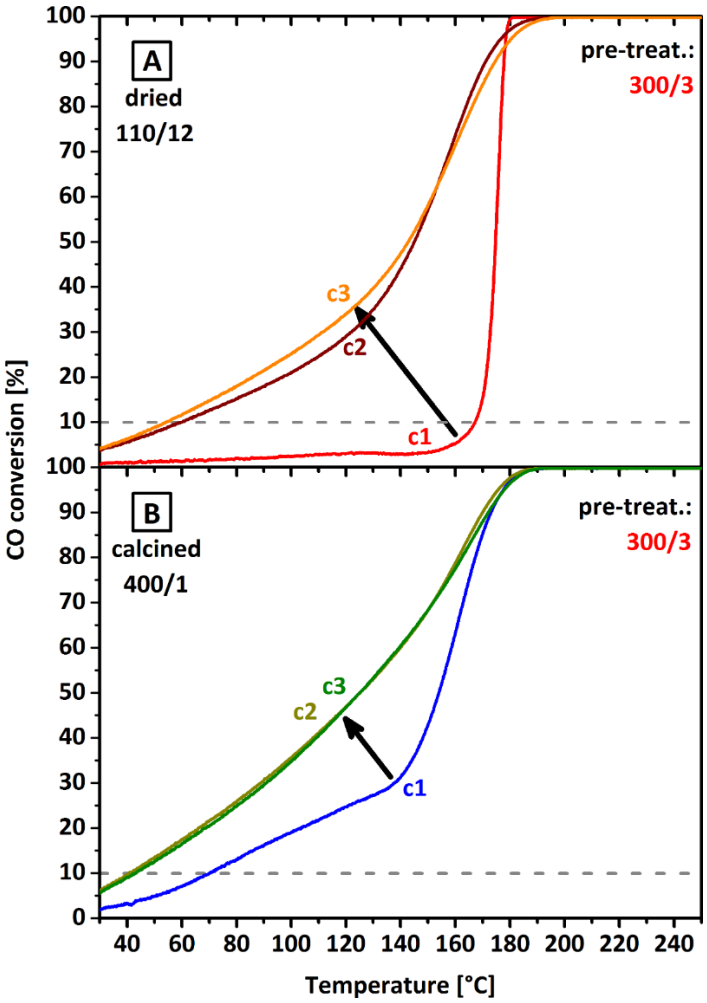

Figure 12. CO oxidation cycles (c1 – c3) for $AgNO_3/SiO_2$ precursor dried at 110 °C for 12 h (110/12) (A) and $Ag5/SiO_2$ catalyst calcined at 400 °C for 1 h (400/1) (B). Both samples were pre-treated at 300 °C for 3 h (300/3).

The *in-situ* autocatalytic conversion of residual $AgNO_3$ to Ag^0 induced by the CO oxidation feed has a significant impact on the catalytic performance. In comparison to the thermolysis/calcination approach (above 500 °C) the *in-situ* creation of Ag nanoparticles is a rather mild and elegant method to create and stabilize even smaller particles or clusters, showing CO oxidation activity already at 30 °C (Figure 12B). For the investigation of the emerging PS during the *in-situ* reduction of $AgNO_3$ during CO oxidation, the Ag PS distributions of freshly synthesized $Ag5/SiO_2$ samples 400/1 and 600/1 were compared to their spent counterparts after CO oxidation (Figure 13). The fraction of particles below 6 nm was determined to be less than 1% for the samples before and after catalysis, thereby supporting their high sintering stability. The PS distributions of the 400/1 sample before and after three cycles of CO oxidation are presented in Figure 13A. The fresh sample exhibits a median PS of 2.0 nm with a fraction of 6.4 % on Ag clusters smaller than 1 nm (ca. less than 50 Ag atoms per particle). During the CO oxidation cycles the median PS is further decreased

to 1.7 nm, also indicated by the increased moieties of Ag clusters to 14.2 %. The higher fraction of Ag clusters is attributed to their *in-situ* formation upon CO oxidation and conversion of residual $AgNO_3$. Figure 13B shows the PS distribution of the 600/1 catalyst. The fresh sample has a median PS of 2.3 nm, thereby being slightly larger compared to the fresh 400/1 sample. Also, the fraction of Ag clusters below 1 nm, determined to 1.7 %, is smaller. After CO oxidation the median of the present PS (2.4 nm) and the fraction of Ag clusters (1.6 %) are almost unchanged compared to the fresh sample, which is in very good agreement to the stable catalytic activity and $T_{10\%}$ values (see insets Figure 13). The 400/1 catalyst shows, in contrast, a significant increase in CO oxidation activity upon cycling ($T_{10\%}$ decreased by 27 °C). This is in direct correlating to the *in-situ* formation of Ag clusters, strongly evidencing its huge impact on catalysis.

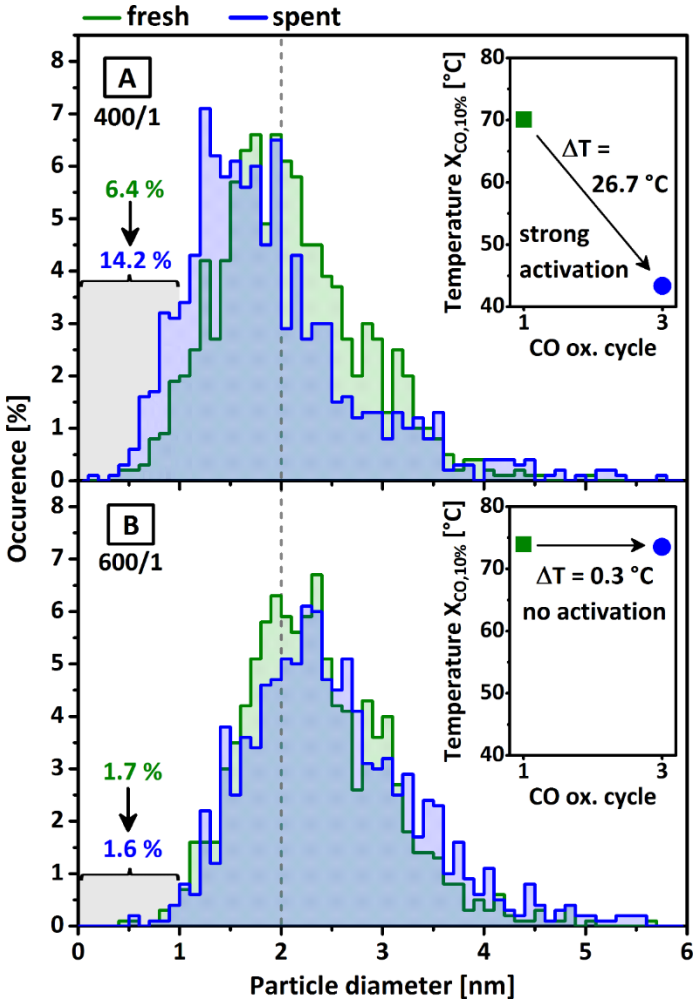

Figure 13. PS distributions from STEM (0.1 nm bin size) for Ag5/SiO_2 catalysts calcined at 400/1 (A) and 600/1 (B). Shown are fresh (green) and spent samples (blue) after three cycles of CO oxidation after 300/3 pre-treatment, as well as cumulative percentages for the fractions < 1.0 nm for fresh to spent samples. Insets show $T_{10\%}$ for 1st (green) and 3rd cycle (blue).

These findings are not consistent with the results of Lim *et al.*[18] claiming that Ag particles below 3 nm are no good catalysts for CO oxidation and Qu *et al.*[17] reporting that catalysts with Ag PS of 6 – 8 nm are the most active for CO oxidation. Those results are indicating a structure sensitivity with inferior catalytic activity

for nanoparticles below 3 nm and are in contrast to our work. This discrepancy is likely explained by an inappropriate pre-treatment and the low reaction temperatures applied in their studies.

To exclude different reaction mechanisms for samples Ag5/SiO_2 the reaction order at 100 °C for selected catalysts was calculated after 300/3 pre-treatment and performing one CO oxidation cycle to 250 °C for a final $AgNO_3$ removal and Ag cluster formation (Figure 14 and Figure S31 for complete test). In general, for all samples the reaction order is below one and higher for CO than for O_2, which indicates a higher dependence on the $\rho(CO)$ than on $\rho(O_2)$. Values for catalysts 500/1, 600/1 and 600/3 range between $n(O_2) = 0.30 – 0.32$ and $n(CO) = 0.63 – 0.68$. This indicates a higher coverage with oxygen in comparison to CO as general feature. For sample Ag5/SiO_2 400/1 the reaction orders are lower with $n(O_2) = 0.09$ and $n(CO) = 0.41$. This implies that the reaction rates are almost independent of the $\rho(O_2)$ and that the activation of O_2 is facile. Since Ag tends to form also subsurface oxygen species, the particle and/or cluster size might serve as descriptor for this behavior and vice versa, small clusters stabilize oxygen rather near the surface. This discrepancy between sample 400/1 and the samples calcined at higher temperatures is interpreted as a result of the highly active Ag clusters. They are *in-situ* created during the first CO oxidation cycle for the 400/1 sample and their distinctness is also visible in the different kinetic parameters, i.e. reaction orders.

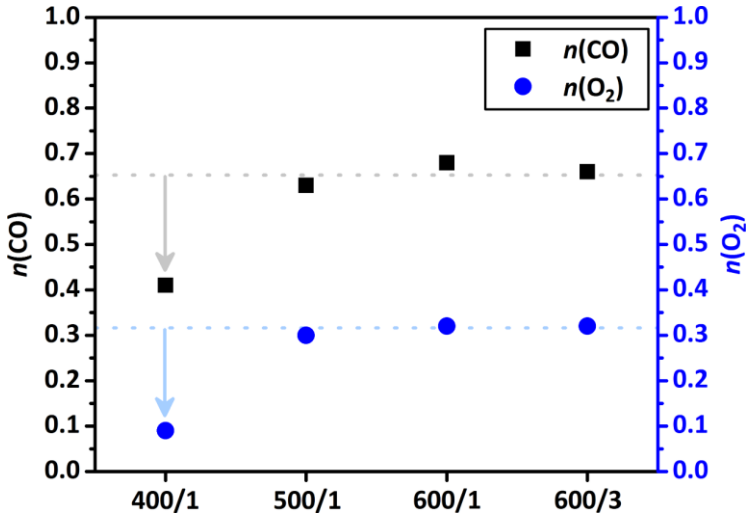

Figure 14. Reaction orders *n* for CO and O_2 for CO oxidation at 100 °C after 300/3 pre-treatment conditions and one CO oxidation cycle to 250 °C of Ag5/SiO_2 catalysts calcined at different conditions.

2.4.3 Evaluation of the silver – oxygen interaction

A suitable technique to extract information on the intriguing silver – oxygen (Ag–O) chemistry, for which several surface and subsurface oxygen species are discussed, is thermal desorption spectroscopy of oxygen (O_2-TDS).[27, 57] We developed an adapted TDS setup dedicated for the investigation of powder samples.[58]

Figure 15 shows the TDS curves of oxygen for the Ag5/SiO_2 600/1 sample and the Ag15/α-Al_2O_3 reference sample. The samples were pre-treated in synthetic air for 12 h at 210 °C and atmospheric pressure. The desorption was performed under high vacuum conditions and a heating rate of 25 °C·min^{-1}. The peak maximum of the oxygen desorption event for Ag15/α-Al_2O_3 is located at around 166 °C with a small event at around 550 °C, probably correlated to the bimodal PS distribution as observed *via* STEM analysis (Figure S26) or to a rather subsurface desorption event at higher temperatures. The Ag5/SiO_2 600/1 sample shows a peak maximum centered at 360 °C, strongly shifted to higher temperatures in comparison to Ag15/α-Al_2O_3. The intensities directly indicate the high dispersion of the Ag nanoparticles on SiO_2 in comparison to the rather bulk-like Ag particles on the low surface area α-Al_2O_3 support with ca. three times higher loading. The desorbed oxygen amount per Ag of the first events for Ag15/α-Al_2O_3 and Ag5/SiO_2 600/1 is 12.5 times higher for the Ag nanoparticles with a Ag:O_2 ratio of around 200. Besides, a second desorption event above 540 °C evidences additional oxygen species with an even stronger stabilization. The temperature difference of almost 200 °C of the main desorption events is attributed to the stability of the oxygen species in/on the Ag. The Ag nanoparticles (median PS 2.3 nm) are able to stabilize the atomic oxygen species much stronger. This effect is tentatively interpreted as $Ag^{\delta+}O_x$ with strong ionic character of the O_x, respectively $Ag^{\delta+}$. This higher oxophilicity (and rather ionic character of the Ag–O interaction) of the Ag5/SiO_2 samples is in accordance with the higher tendency to form Ag_2CO_3 as already discussed earlier.

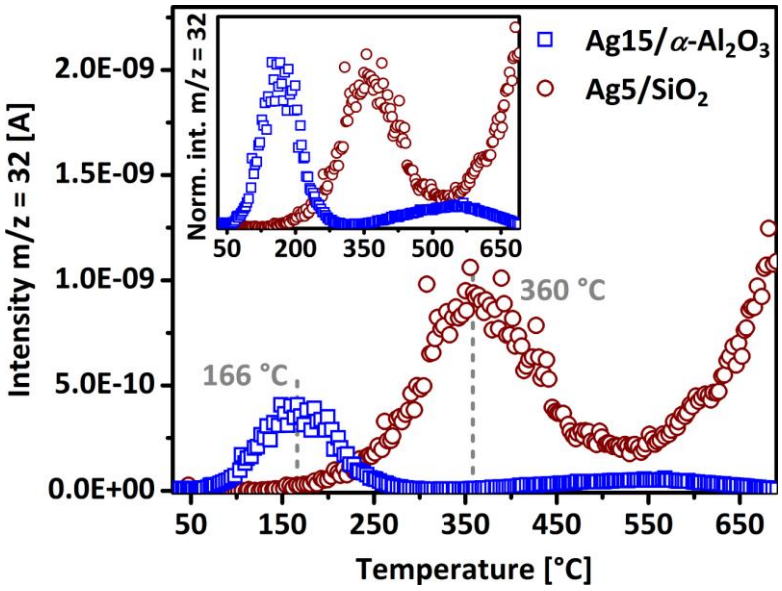

Figure 15. O_2-TDS for Ag15/α-Al_2O_3 (blue) and Ag5/SiO_2 (red) catalysts *ex-situ* calcined at 600 °C for 1 h and pre-treated at 200 °C for 12 h.

The *in-situ* generation of Ag nanoparticles and clusters is additionally investigated by TDS. To clarify the origin of the desorbed oxygen, the $AgNO_3$/SiO_2 precursor was *in-situ* calcined at 600 °C for 1 h using non-

labeled $^{16}O_2$ and completely labeled $^{18}O_2$ as part of synthetic air. The corresponding oxygen desorption spectra are shown in Figure 16. For both calcination conditions high desorption maxima are detected with around 630 °C for the non-labeled experiment and around 600 °C for the labeled one. The slightly shifted desorption maxima are explained by the different flow conditions during the calcination. However, despite using only labeled $^{18}O_2$ for the latter case, the dominant oxygen species desorbing is completely unlabeled (m/z = 32). In addition, the partially labeled $^{18}O^{16}O$ (m/z = 34) desorption signal is increased upon $^{18}O_2$ calcination. For completely labeled $^{18}O_2$ no difference in the corresponding desorption signals is observed. The mixed labeled $^{16}O^{18}O$ event originates very likely from a dissociatively activated $^{18}O_2$ distributed in/on Ag. Those results clearly identify the oxygen containing precursor-anion (here: NO_3^-) as main source of the oxygen desorption event from Ag nanoparticles. Only a minor fraction of oxygen from the gas phase is incorporated during the calcination process. Besides, the *in-situ* generated Ag particles exhibit an increased binding strength to oxygen (desorption maxima above 600 °C), which seems to be in line with the according PS distribution and a distinct fraction of around 15 % Ag clusters below 1 nm (Figure S32).

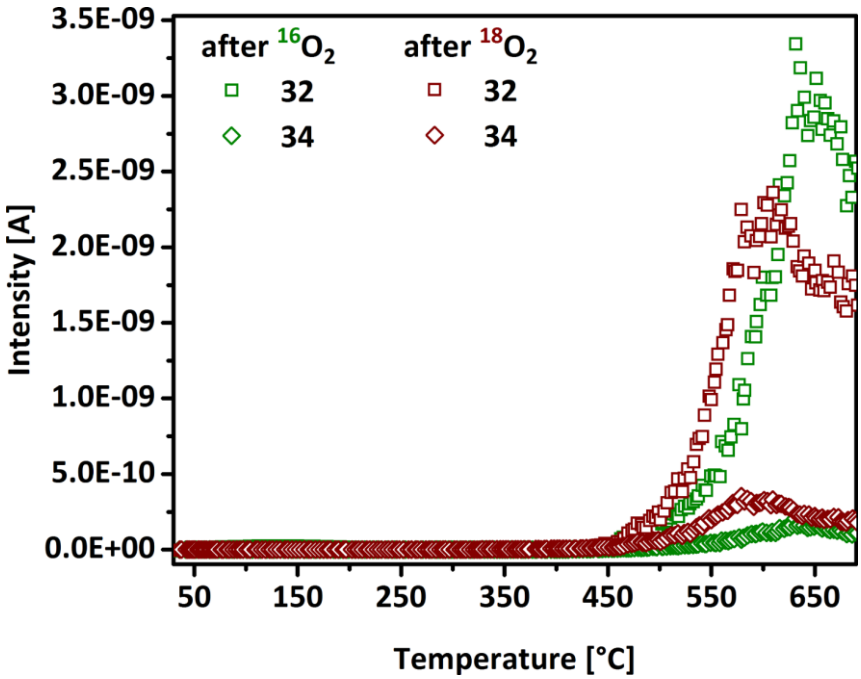

Figure 16. O_2-TDS for Ag5/SiO_2 *in-situ* calcined with synthetic air (green) and $^{18}O_2$ labeled synthetic air (red). m/z = 32 ($^{16}O_2$) are shown as squares and m/z = 34 ($^{18}O^{16}O$) as diamonds.

Comparing *ex-situ* and *in-situ* generated Ag nanoparticles/clusters and their corresponding desorption events (Figure 15 and Figure 16) a shift for the main desorption event of more than 200 °C is revealed. Both samples origin from the same synthesis batch and a similar PS distribution is gained (median PS 2.3 nm and 2.0 nm). The main differences of these samples and corresponding desorption events are therefore likely related to the fraction of Ag cluster, which is 15 % for *in-situ* vs. 2 % for the *ex-situ* treatment, and the contact

to the environment, leading to a CO_2 induced carbonate formation. A stronger Ag–O interaction for Ag clusters would explain a more pronounced high temperature desorption event but not the absence of the event at 360 °C. Figure S33 shows the O_2 (m/z = 32) and CO_2 (m/z = 44) desorption signals of the *ex-situ* calcined sample. Interestingly, the desorption events seem to be coupled and the O_2 signal follows the CO_2 one. The stability of the carbonate might influence also the oxygen desorption temperature. To estimate the impact of the formed carbonates, the *in-situ* calcined sample was exposed to CO_2 prior to the desorption. The resulting O_2-TDS (Figure S34) shows a shift of the main desorption to around 370 °C, which is in good agreement to the desorption event for the *ex-situ* calcined sample. This evidences a desorption window for oxygen stabilized in/on Ag nanoparticles and clusters from 350 °C to 630 °C, dependent on the character of the formed carbonate, which is also connected to the cluster fraction (PS dependent carbonate formation, see also Figure S23). Further, we tentatively interpret this effect as a carbonate induced mobilization of oxygen in/on the Ag nanoparticles. Thereby, the strength of the Ag–O interaction is reduced which leads to a shift to lower temperatures in the corresponding O_2-TDS curve. This phenomenon further contributes to the understanding of the high reactivity of *in-situ* generated nanoparticles and clusters.

To further investigate the ability of these systems to activate O_2, microcalorimetry experiments were conducted (Figure 17). The Ag15/α-Al_2O_3 sample and the $AgNO_3/SiO_2$ precursor were both *in-situ* calcined at 600 °C for 1 h prior to the O_2 dosing at 200 °C. The integral heat of adsorption of the Ag15/α-Al_2O_3 sample is in the range of 120 kJ·mol^{-1}, decreases upon titrating to a plateau at around 70 kJ·mol^{-1} and finally reaches values below 30 kJ·mol^{-1}. Based on DFT calculation for the adsorption energy (E_{ads}) of oxygen on various Ag surfaces (details are found in the SI) the experimental results are interpreted as dissociatively activated oxygen species, with heats of adsorption (Q_{ads}) in the range of 120 – 70 kJ·mol^{-1}, followed by molecular oxygen adsorbed on defects and grain boundaries (Q_{ads} in the range of 60 – 20 kJ·mol^{-1}). The SiO_2 supported Ag nanoparticles show no interaction with the dosed O_2 at 200 °C. As shown by TDS analysis (Figure 16), this is explained by the already stable oxygen saturated state forming $Ag^{\delta+}O_x$ species during *in-situ* calcination (mainly from $AgNO_3$), that are consequently unable to further activate molecular oxygen. Subsequently, to remove oxygen species in and on Ag, both samples were pre-treated in hydrogen at 400 °C.

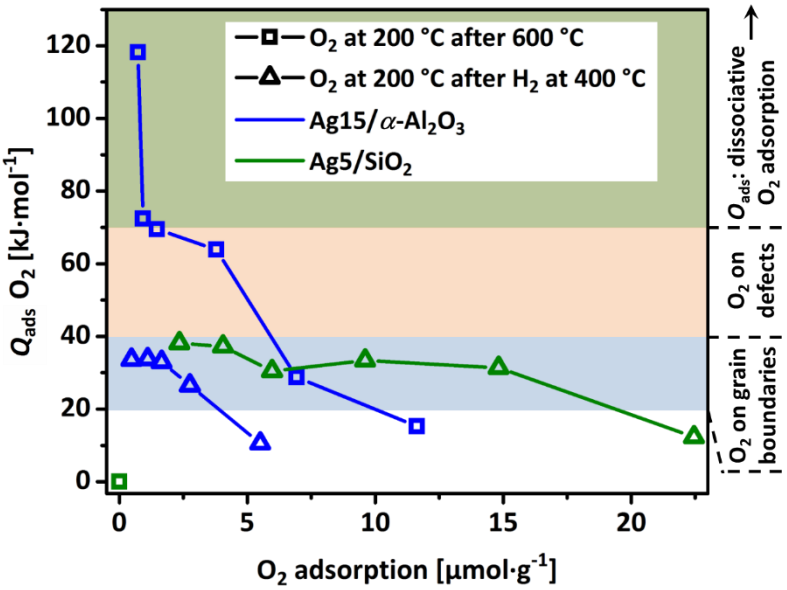

Figure 17. Microcalorimetric oxygen adsorption on Ag15/α-Al_2O_3 and Ag5/SiO_2 *ex-situ* calcined at 600/1 conditions. O_2 adsorption was performed at 200 °C after a pre-treatment at 10^{-8} mbar and 600 °C and additional 400 °C with H_2. On the right the corresponding adsorption sites are shown based on DFT calculations.

Temperature programmed reduction (TPR) experiments under 0.25 % H_2 atmosphere were already performed to monitor the consumption of different kind of oxygen species by H_2 under the formation of water (Figure S35), showing that 400 °C is a reasonable temperature for a complete reduction of Ag. H_2O events at higher temperatures a related to support effects. Titrating the reduced samples again with O_2 led qualitatively to comparable results for both samples, with Q_{ads} values in the range of 30 to 40 kJ·mol^{-1}. The Ag nanoparticles offer more adsorption sites for oxygen, which are according to DFT calculations for both samples in the regime of molecular oxygen on different surfaces. These results show that the oxygen species, also the stabilized oxygen on Ag nanoparticles, were successfully removed by the reducing treatment. Besides, it is clearly shown that for a dissociative activation of oxygen, oxygen species in and on Ag, not too ionic and stable, have to be already present. If not, oxygen is only molecularly adsorbed, since the oxygen-free Ag^0 particles have a closed d-band and are inactive.[59] After the microcalorimetry experiments a median PS of 2.5 nm (99.9 % below 7.2 nm, Figure S36) is found *via* STEM analysis, confirming that the *in-situ* created sample is comparable to Ag5/SiO_2 600/1 and representative for the series of Ag nanoparticles stabilized on SiO_2. However, the results obtained by the integral methods of oxygen TDS and microcalorimetry offer valuable insights in the nature of the Ag–O interaction, but a surface quantification of Ag, or an identification of the number of reaction sites on Ag, is due to the subsurface contributions very difficult.

To further evaluate the strength of the Ag–O interaction on the surface, we have to introduce a probe molecule, which interacts with the partially oxidized $Ag^{\delta+}O_x$ and is unable to develop a Ag subsurface chemistry. For this purpose, ethylene (C_2H_4) is identified since the $Ag^{\delta+}O_x$ surface behaves like a selective "chromatographic column" and C_2H_4 adsorbs easily. Besides, it is well known that metallic Ag is not able to

interact with C_2H_4 since its electronic configuration of s^1d^{10} does not allow transferring electrons to the Ag d-band.[22, 60, 61] This theory was confirmed for a Ag5/SiO_2 600/1 sample reduced at 400 °C in 5 % H_2, resulting in a metallic supported Ag catalyst. This sample showed no heat evolution upon C_2H_4 dosing *via* microcalorimetry and therefore no interaction with C_2H_4. For the partially oxidized $Ag^{\delta+}$, electron density from the Ag^0 d-band is removed which enables the donation of π-electrons. This interaction allows C_2H_4 to be a suitable sensor for the titration of all kinds of Ag^+ sites from Ag_2O, $AgNO_3$ and $Ag^{\delta+}$ sites from partially oxidized $Ag^{\delta+}O_x$. Furthermore, the C_2H_4 interaction strength with $Ag^{\delta+}O_x$ is also an indirect measurement for the strength of Ag–O interaction, since the binding strength of C_2H_4 depends on the strength of interaction of oxygen with Ag and the corresponding acceptance of π-electrons. For ruling out any interaction of C_2H_4 and the SiO_2 support, a pure SiO_2 sample which was equally treated than the Ag5/SiO_2 samples (blind impregnation with H_2O) was also measured. Due to the absence of any heat evolution upon C_2H_4 dosing the support is interpreted as inert.

Figure 18 illustrates the results of the microcalorimetric C_2H_4 adsorption experiments and the corresponding integral heat evolutions. At first, the $AgNO_3/SiO_2$ precursor was *in-situ* activated at 300/3 and subsequently C_2H_4 was adsorbed. The Q_{ads} are in the range of 85 – 90 kJ·mol^{-1} and decrease gradually upon dosing. The adsorption of the C_2H_4 molecules was reversible (qualitatively and quantitatively under vacuum treatment, 90 µmol·g^{-1}) and for this sample very likely related to $Ag^{\delta+}O_x$ from Ag nanoparticles and Ag^+ adsorption centers from residual $AgNO_3$. For a possible discrimination between the nature of the Ag–O interaction of Ag clusters (below 1 nm) and Ag nanoparticles (1 – 6 nm) the precursor $AgNO_3/SiO_2$ was additionally *in-situ* reduced using CO as reduction agent, comparable to one CO oxidation cycle (see also Figure 12). As shown before, the reductive CO atmosphere *in-situ* reduces the Ag^+ species of the residual $AgNO_3$ under the formation of Ag nanoparticles and clusters. The resulting C_2H_4 adsorption led to Q_{ads} in the range of 100 kJ·mol^{-1}, which is a difference in the maximum Q_{ads} of 13 kJ·mol^{-1} compared to the adsorption without the reduction in CO atmosphere. Further, the amount of adsorption centers was reduced, which matches very well with loss of Ag^+ sites on the expense of $Ag^{\delta+}O_x$ sites (38 µmol·g^{-1}, see also Figure 9). For the readsorption on the reduced sample after vacuum treatment, the highest detected Q_{ads} is in the range of 80 – 85 kJ·mol^{-1} which indicates the irreversibility of the $Ag^{\delta+}O_x$–C_2H_4 interaction (integral heat evolutions above 90 kJ·mol^{-1}). The *ex-situ* calcined 600/1 sample without Ag clusters showed upon C_2H_4 titration also Q_{ads} in the range of 85 – 90 kJ·mol^{-1}. This implies that the *in-situ* created Ag clusters exhibit $Ag^{\delta+}O_x$ species which are more ionic/oxidic than the Ag nanoparticles. The amount of irreversible sites was in the range of 10 % (3.7 µmol·g^{-1} of 38 µmol·g^{-1}) and in reasonable agreement with the amount of Ag clusters of the 400/1 samples after CO oxidation. Again, the sample with the irreversible adsorption sites from the microcalorimetry study was investigated *via* STEM for a PS analysis. Figure 19 shows the corresponding

histogram of the PS distribution, being in very good agreement with the PS distribution of the 400/1 sample (see also Figure 13). This strongly evidences a direct correlation between the number of Ag clusters and the number of irreversible adsorption sites. These adsorption sites, binding the oxygen species stronger (more oxidic), might also be responsible for the lowered reaction orders and the higher ability in activating oxygen within a catalytic cycle. Finally, an inverse trend for the strength of the Ag–O interaction and the corresponding PS and ionicity is manifested by complementary techniques (PXRD, STEM, TDS and microcalorimetry): bulk-like (20 – 300 nm) < Ag nanoparticles (1 – 6 nm) < Ag clusters (below 1 nm).

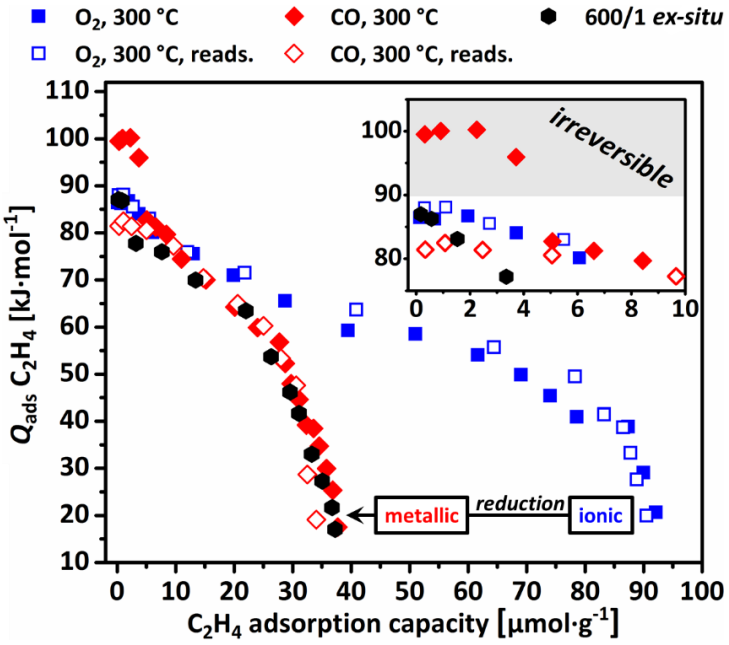

Figure 18. Microcalorimetric integral heat of adsorbed C_2H_4 (Q_{ads} C_2H_4) at 40 °C on $AgNO_3/SiO_2$ together with the corresponding C_2H_4 adsorption capacity after *in-situ* pre-treated at conditions of 300/3 in synthetic air (blue squares), subsequent CO oxidation feed exposure at 300 °C (red diamonds) together with the respective readsorptions (empty symbols). As comparison sample $Ag5/SiO_2$ *ex-situ* calcined at 600/1 after 300/3 pre-treatment conditions is shown as black hexagons.

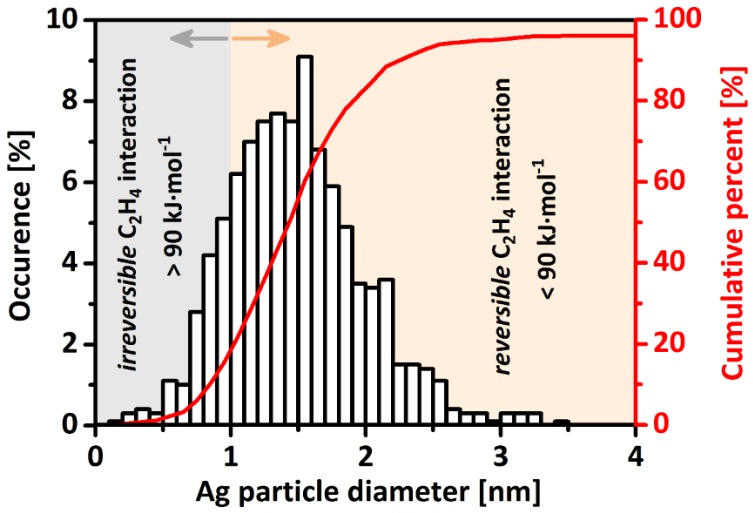

Figure 19. PS distribution from STEM with 0.1 nm bin size for spent $AgNO_3/SiO_2$ after *in-situ* 300/3 synthetic air treatment, CO reduction at 300 °C and C_2H_4 microcalorimetry as presented in Figure 18.

2.4.4 Correlation of silver surface area and catalytic activity

For a better comparison and investigation of catalytic relations it is necessary to determine the specific surface area of a catalyst. Conventional analysis of Ag surface areas is done by oxygen involving methods[62-64] which are from our point of view due to the complex surface and subsurface Ag–O chemistry very challenging. Therefore, we used the already introduced concept of partially oxidized Ag samples to interact with C_2H_4 as probe molecule of choice as for the microcalorimetric study. In comparison to the microcalorimetric setup (static and semi-quantitative), we combined this idea with a temporal analysis of products approach at atmospheric pressure (atmTAP[51]). The C_2H_4 is dosed at 40 °C into a high-speed transient fixed bed operating under plug flow conditions as described in the experimental section. By using this setup, the calculated C_2H_4 adsorption capacities are determined under conditions comparable to standard catalytic test reactors creating highly reliably correlations.

Figure 20 illustrates the principle of measurement. By comparing the reactor residence time of C_2H_4 with the non-adsorbing reference Ar, the amount of adsorbed C_2H_4 can be calculated from the mass balance. Let the signal for C_2H_4 as a function of time t be denoted by $S(t)$ and the total volumetric flow rate by F_V. From the mass balance it follows that the number of moles of adsorbed molecules N_{ad} per gram catalyst is given by eq 1:

$$N_{ad}/m_{cat} = c_{C2H4}/F_V \cdot m_{cat} \cdot \int_0^{\infty} 1 - S(t)/S(\infty)\, dt \qquad \text{(eq 1)}$$

where c_{C2H4} is the molar concentration of C_2H_4 and $S(\infty)$ is the steady-state signal reached after the mean breakthrough time. Since c_{C2H4} is very low, indeed below 0.5 %, we can neglect the change of F_V due to adsorption and consider it a constant. The resulting amounts of adsorbed C_2H_4 are presented in Figure 21A showing the average over three measurements for each sample. All measurements were performed on $Ag5/SiO_2$ samples pre-treated at 300/3 conditions. Samples without remaining $AgNO_3$ like 500/1, 500/3, 600/1 and 600/3 are all in the same range with an average C_2H_4 adsorption capacity of 28.3 $\mu mol \cdot g_{cat}^{-1}$, 25.9 $\mu mol \cdot g_{cat}^{-1}$, 30.8 $\mu mol \cdot g_{cat}^{-1}$ and 31.5 $\mu mol \cdot g_{cat}^{-1}$, respectively. These results indicate that samples calcined at 500 °C and 600 °C have a comparable number of adsorption sites for C_2H_4. The slightly increased number of adsorption sites for the samples calcined at 600 °C are in line with the PS distributions (Figure 13, Figure S37 and overview in Table 1).

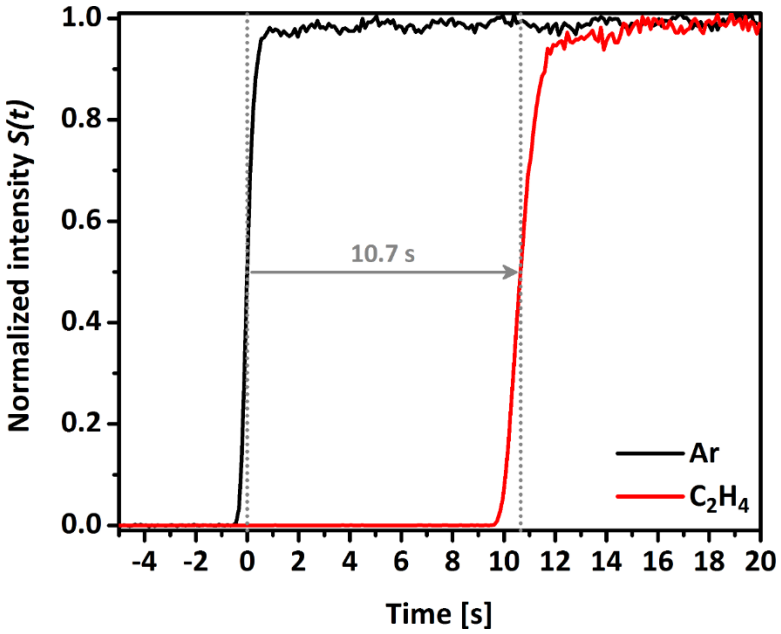

Figure 20. Ar and C_2H_4 breakthrough curves over a Ag5/SiO_2 catalyst with p_{C2H4} of 3.93 mbar and F_V of 100 ml·min^{-1} at 40°C.

Samples calcined at 400 °C show a significantly higher C_2H_4 adsorption capacity of in average 71.7 µmol·g_{cat}^{-1} for 400/0, 50.9 µmol·g_{cat}^{-1} for sample 400/1 and 51.2 µmol·g_{cat}^{-1} for sample 400/3. For 400/0 the remaining $AgNO_3$ contributed strongly to the high adsorption value. This is also visible in the change from measurement one to three, namely the decrease of C_2H_4 adsorption capacity from 76.7 µmol·g_{cat}^{-1} to 70.8 µmol·g_{cat}^{-1} to 67.6 µmol·g_{cat}^{-1} (Figure S38). This decrease was induced by the thermolysis during the intermediate 230 °C heat treatment applied for desorbing the C_2H_4 in between each of the three measurements. It further led to the formation of nanoparticles and clusters which have a smaller number of adsorption sites than atomically dispersed Ag^+, thereby decreasing the overall adsorption capacities (in line with the microcalorimetric C_2H_4 adsorption). This change is less pronounced for sample 400/1, with only a weak decrease from 51.9 µmol·g_{cat}^{-1} to 50.6 µmol·g_{cat}^{-1} and 50.4 µmol·g_{cat}^{-1}, whereas the difference of measurement two to three is within the measurement error of the setup of approximately ±0.3 µmol·g_{cat}^{-1}. Furthermore sample 400/1 and 400/3 are resulting in the same adsorption capacities, indicating that for sample 400/1 no remaining $AgNO_3$ was present for the second and third analysis.

Based on the adsorption measurements, the Ag surface can be estimated. Under the assumption of a full oxygen coverage of the Ag surface, it is assumed that one C_2H_4 molecule binds to one Ag_2O site, consequently meaning that one C_2H_4 titrates two Ag atoms. Thereby, we can determine the number of Ag atoms present on the surface. Using a covalent radius for Ag of 144 pm[45], the following Ag surface areas are calculated based on the number of Ag atoms. The determined adsorption capacities as well as the calculated apparent Ag surface area are presented in Table 3.

The Ag15/α-Al_2O_3 reference was measured using surface titration experiments *via* microcalorimetry, since the surface area values are too small for the atmTAP approach. The C_2H_4 adsorption (Figure S39) is determined to 2.17 µmol·g_{cat}^{-1} and is further compared to the catalytic CO oxidation performances (see values Table 2).

Table 3. C_2H_4 adsorption capacities determined by atmTAP, corresponding apparent Ag surface areas and CO oxidation rates at a temperature of 100 °C

sample	C_2H_4 ads. capacity [µmol·g^{-1}]	Ag surface area [m^2·g^{-1}]	$Rate_{100°C}$ CO ox. cycle 3 [µmol·g^{-1}·s^{-1}]
Ag5/SiO_2 400/1	50.9	4.00	158.3
Ag5/SiO_2 400/3	51.2	4.02	154.9
Ag5/SiO_2 500/1	28.3	2.22	69.3
Ag5/SiO_2 500/3	25.9	2.03	61.6
Ag5/SiO_2 600/1	30.8	2.42	77.0
Ag5/SiO_2 600/3	31.5	2.59	67.9
Ag15/α-Al_2O_3*	2.17	0.17	2.9

*determined by microcalorimetric C_2H_4 adsorption

As presented in Figure 21B the calculated surface areas are related to the rate in CO oxidation at 100 °C for cycle three after 300/3 pre-treatment conditions, as performed for the atmTAP measurements. A linear correlation can be drawn for samples up to Ag surface areas of 2.6 m^2·g^{-1} taking nearby various Ag5/SiO_2 samples, also pure SiO_2 support and the reference Ag15/α-Al_2O_3 sample into account. As discussed above, these samples, Ag nanoparticles vs. bulk-like Ag, exhibit different Ag–O interactions, but are free of Ag clusters. By comparing the high Ag surface area catalysts of around 4 m^2·g^{-1}, the linear correlation does not fit. The calculated rate is about 35 µmol·g^{-1}·s^{-1} higher than extrapolated by the linear correlation. Since these samples prone to form Ag clusters, the discrepancy is explained by the nature of the Ag clusters also indicated by the irreversible sites for C_2H_4 adsorption (Figure 18). Since CO oxidation is only possible upon activation of oxygen by the catalyst, the Ag–O interaction strength is also relevant for CO oxidation. Therefore, it is reasonable that the linear correlation does not include the Ag clusters, which are dominating the catalytic reactions. This is also visible by a change of reaction orders and finally resulting in a Ag particle/cluster size effect for the CO oxidation reaction.

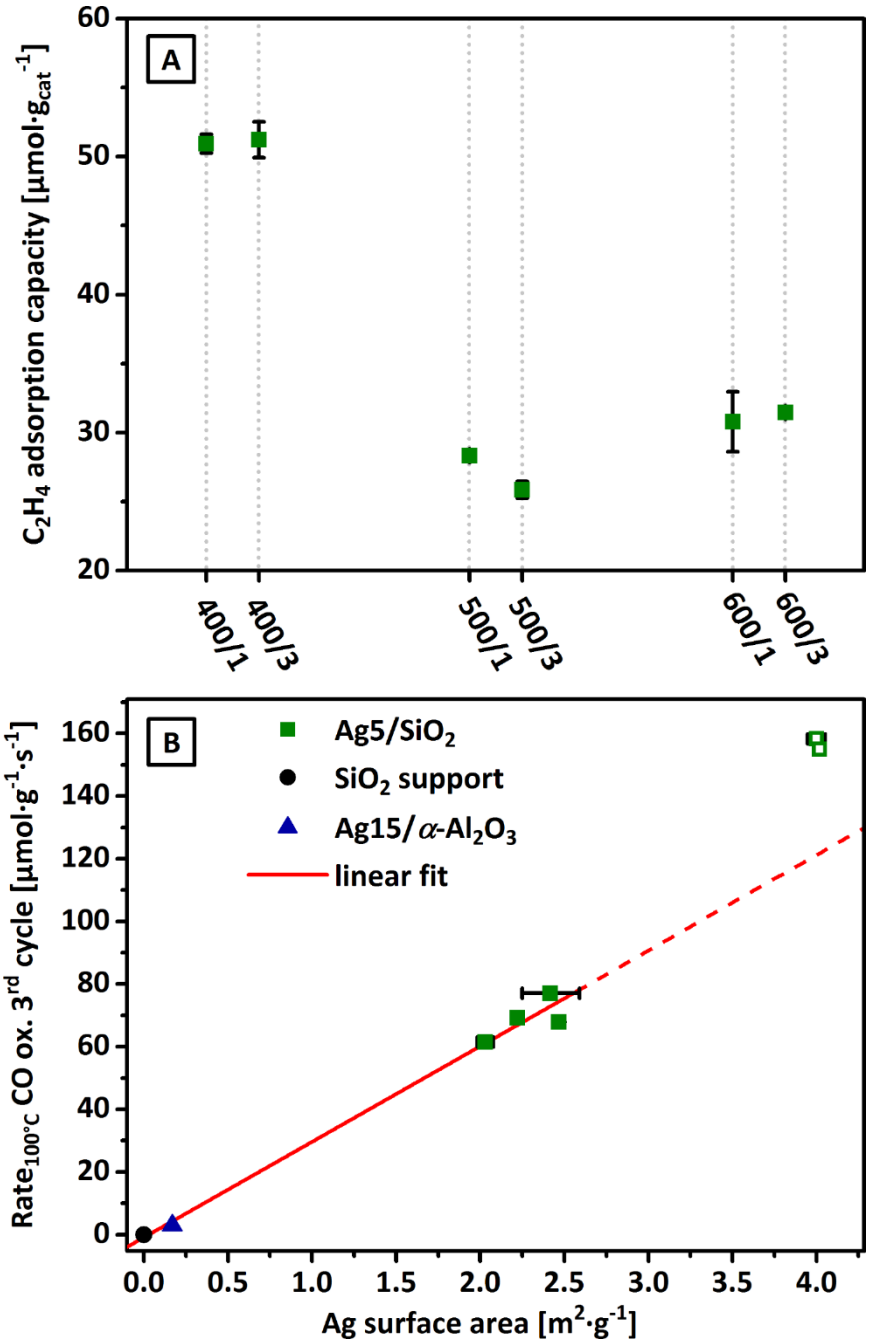

Figure 21. (A) C_2H_4 adsorption capacities of Ag5/SiO_2 catalysts calcined at 400 °C, 500 °C and 600 °C for 1 h and 3 h dwell time and (B) resulting apparent Ag5/SiO_2 Ag surface areas (green squares) correlated with CO oxidation rate at 100 °C for the 3rd cycle together with the pure support without Ag loading (black circle). Additionally, Ag15/α-Al_2O_3 apparent Ag surface area determined from microcalorimetric C_2H_4 adsorption is shown (blue triangle). The corresponding linear fit is presented as red line with a coefficient of determination of 0.986.

2.5 Conclusion

We report on an improved synthesis approach for a set of SiO_2 supported Ag nanoparticles with a narrow PS distributions and median PS of around 2 nm based on an advanced incipient wetness impregnation technique. Ag nanoparticles showed a high tendency to form Ag_2CO_3, as demonstrated by PXRD, which was absent for bulk-like Ag particles of a Ag15/α-Al_2O_3 reference sample. Catalysts Ag5/SiO_2, exhibiting solely

Ag nanoparticles and clusters, were highly active in CO oxidation, after a dedicated pre-treatment which is related to the Ag_2CO_3 formation. Performing detailed investigations concerning the pre-treatment conditions we were able to demonstrate that Ag nanoparticles need a significantly harsher pre-treatment compared to bulk-like Ag particles, e.g. higher temperature and/or longer dwell times. This pre-treatment dependence might also be the reason for differentiated findings in literature concerning Ag nanoparticles and their catalytic performance. Further, Ag clusters were *in-situ* created and showed a significantly higher activity in CO oxidation.

Investigations on the correlation of Ag PS and the strength of the Ag–O interaction were performed. TDS experiments showed significantly higher desorption temperatures of stable oxygen species for Ag nanoparticles. The formation of high temperature stable oxygen species with a strong Ag–O interaction on Ag nanoparticles and clusters were confirmed by microcalorimetric oxygen and C_2H_4 adsorption experiments. The strength of the Ag–O interaction is attributed to the higher ionicity of the $Ag^{\delta+}O_x$ species directly correlating with the tendency of carbonate formation. Especially, the Ag clusters, also responsible for different reaction orders upon comparison to Ag nanoparticles, showed, using C_2H_4 titration, an in parts irreversible adsorption behavior. This finding supports a PS effect for Ag clusters in CO oxidation.

A newly introduced method for the determination of the accessible Ag surface area was applied based on the C_2H_4 adsorption capacity. Thereby, a linear correlation of the CO oxidation rate with the Ag surface area of bulk-like Ag and Ag nanoparticles was demonstrated. Ag clusters exhibited a superior CO oxidation activity compared to nanoparticles and bulk Ag particles and deviated from the linear correlation, which can be directly attributed to the discussed Ag–O interaction and a distinct cluster size effect for Ag smaller than 1 nm in size.

2.6 References

[1] G. W. Keulks, C. C. Chang, *J. Phys. Chem.* **1970**, *74*, 2590-2595.

[2] M. Qian, M. A. Liauw, G. Emig, *Appl. Catal. A* **2003**, *238*, 211-222.

[3] M. O. Ozbek, I. Onal, R. A. van Santen, *J. Catal.* **2011**, *284*, 230-235.

[4] R. M. Lambert, F. J. Williams, R. L. Cropley, A. Palermo, *J. Mol. Catal. A: Chem.* **2005**, *228*, 27-33.

[5] V. I. Bukhtiyarov, I. P. Prosvirin, R. I. Kvon, S. N. Goncharova, B. S. Bal'zhinimaev, *J. Chem. Soc., Faraday Trans.* **1997**, *93*, 2323-2329.

[6] J. K. Lee, X. E. Verykios, R. Pitchai, *Appl. Catal.* **1989**, *50*, 171-188.

[7] J. C. Wu, P. Harriott, *J. Catal.* **1975**, *39*, 395-402.

[8] G. A. Somorjai, A. M. Contreras, M. Montano, R. M. Rioux, *Proceedings of the National Academy of Sciences* **2006**, *103*, 10577.

[9] J. Grunes, J. Zhu, G. A. Somorjai, *Chem. Commun. (Cambridge, U. K.)* **2003**, 2257-2260.

[10] S. V. Tsybulya, G. N. Kryukova, S. N. Goncharova, A. N. Shmakov, B. S. Balzhinimaev, *J. Catal.* **1995**, *154*, 194-200.

[11] S. N. Goncharova, E. A. Paukshtis, B. S. Bal'zhinimaev, *Appl. Catal. A* **1995**, *126*, 67-84.

[12] D. J. Sajkowski, M. Boudart, *Catal. Rev.* **1987**, *29*, 325-360.

[13] X. E. Verykios, F. P. Stein, R. W. Coughlin, *J. Catal.* **1980**, *66*, 368-382.

[14] J. E. van den Reijen, S. Kanungo, T. A. J. Welling, M. Versluijs-Helder, T. A. Nijhuis, K. P. de Jong, P. E. de Jongh, *J. Catal.* **2017**, *356*, 65-74.

[15] A. P. Fotopoulos, K. S. Triantafyllidis, *Catal. Today* **2007**, *127*, 148-156.

[16] Y. Lei, F. Mehmood, S. Lee, J. Greeley, B. Lee, S. Seifert, R. E. Winans, J. W. Elam, R. J. Meyer, P. C. Redfern, D. Teschner, R. Schlögl, M. J. Pellin, L. A. Curtiss, S. Vajda, *Science* **2010**, *328*, 224-228.

[17] Z. Qu, W. Huang, M. Cheng, X. Bao, *J. Phys. Chem. B* **2005**, *109*, 15842-15848.

[18] D. C. Lim, I. Lopez-Salido, Y. D. Kim, *Surf. Sci.* **2005**, *598*, 96-103.

[19] C. T. Campbell, J. R. V. Sellers, *Faraday Discuss.* **2013**, *162*, 9-30.

[20] C. T. Campbell, *Acc. Chem. Res.* **2013**, *46*, 1712-1719.

[21] L. Lefferts, J. G. van Ommen, J. R. H. Ross, *Appl. Catal.* **1987**, *34*, 329-339.

[22] T. E. Jones, R. Wyrwich, S. Böcklein, T. C. R. Rocha, E. A. Carbonio, A. Knop-Gericke, R. Schlögl, S. Günther, J. Wintterlin, S. Piccinin, *J. Phys. Chem. C* **2016**, *120*, 28630-28638.

[23] T. C. R. Rocha, A. Oestereich, D. V. Demidov, M. Havecker, S. Zafeiratos, G. Weinberg, V. I. Bukhtiyarov, A. Knop-Gericke, R. Schlogl, *Phys. Chem. Chem. Phys.* **2012**, *14*, 4554-4564.

[24] M. Rocca, L. Savio, L. Vattuone, U. Burghaus, V. Palomba, N. Novelli, F. Buatier de Mongeot, U. Valbusa, R. Gunnella, G. Comelli, A. Baraldi, S. Lizzit, G. Paolucci, *Phys. Rev. B* **2000**, *61*, 213-227.

[25] E. A. Carbonio, T. C. R. Rocha, A. Y. Klyushin, I. Pis, E. Magnano, S. Nappini, S. Piccinin, A. Knop-Gericke, R. Schlogl, T. E. Jones, *Chem. Sci.* **2018**.

[26] G. Rovida, F. Pratesi, M. Maglietta, E. Ferroni, *Surf. Sci.* **1974**, *43*, 230-256.

[27] D. Herein, A. Nagy, H. Schubert, G. Weinberg, E. Kitzelmann, R. Schlögl, in *Z. Phys. Chem. (Muenchen, Ger.), Vol. 197*, **1996**, p. 67.

[28] T. C. R. Rocha, M. Hävecker, A. Knop-Gericke, R. Schlögl, *J. Catal.* **2014**, *312*, 12-16.

[29] W.-X. Li, C. Stampfl, M. Scheffler, *Phys. Rev. Lett.* **2003**, *90*, 256102.

[30] T. C. R. Rocha, A. Oestereich, D. V. Demidov, M. Havecker, S. Zafeiratos, G. Weinberg, V. I. Bukhtiyarov, A. Knop-Gericke, R. Schlogl, *Phys. Chem. Chem. Phys.* **2012**, *14*, 4554-4564.

[31] C. Rehren, G. Isaac, R. Schlögl, G. Ertl, *Catal. Lett.* **1991**, *11*, 253-265.

[32] G. I. N. Waterhouse, G. A. Bowmaker, J. B. Metson, *Appl. Surf. Sci.* **2003**, *214*, 36-51.

[33] R. Schlögl, *Angew. Chem., Int. Ed.* **2015**, *54*, 3465-3520; *Angew. Chem.* **2015**, 127, 3531-3589

[34] R. Schlögl, S. B. Abd Hamid, *Angew. Chem. Int. Ed.* **2004**, *43*, 1628-1637; *Angew. Chem.* **2004**, *116*, 1656-1667.

[35] P. Harriott, *J. Catal.* **1971**, *21*, 56-65.

[36] G. Busca, *Phys. Chem. Chem. Phys.* **1999**, *1*, 723-736.

[37] T. Rosendahl, T. Mäurer, C. K. Dobner, A. Lehr, J. Wanka; WO 20130/61294 A1, **2013**, BASF SE, Ludwigshafen (GER).

[38] X. Liang, J. Li, M. Yu, C. N. McMurray, J. L. Falconer, A. W. Weimer, *ACS Catal.* **2011**, *1*, 1162-1165.

[39] Z. Ma, S. Dai, in *Heterogeneous Gold Catalysts and Catalysis*, The Royal Society of Chemistry, **2014**, pp. 1-26.

[40] D. Yan, F. Wang, Y. Zhao, J. Liu, J. Wang, L. Zhang, K. C. Park, M. Endo, *Mater. Lett.* **2009**, *63*, 171-173.

[41] A. Cao, R. Lu, G. Veser, *Phys. Chem. Chem. Phys.* **2010**, *12*, 13499-13510.

[42] J. A. Farmer, C. T. Campbell, *Science* **2010**, *329*, 933.

[43] T. Yamamoto, S. Nagase, H. Tanabe; US 5077256 A, **1991**, Nippon Shokubai Kagaku Kogyo C., Ltd., Osaka (JPN).

[44] J. E. Bongaarts, G. R. Meima, J. W. Geus; US 4786743 A, **1988**, The Dow Chemical Company, Midland (USA).

[45] W. M. Haynes, *CRC Handbook of Chemistry and Physics, 96th Edition*, CRC Press, **2015**.

[46] E. Marceau, X. Carrier, M. Che, O. Clause, C. Marcilly, in *Handbook of Heterogeneous Catalysis*, Wiley-VCH Verlag GmbH & Co. KGaA, **2008**.

[47] H. Yang, C. Ma, X. Zhang, Y. Li, J. Cheng, Z. Hao, *ACS Catal.* **2018**, *8*, 1248-1258.

[48] H.-J. Freund, G. Meijer, M. Scheffler, R. Schlögl, M. Wolf, *Angew. Chem.* **2011**, *123*, 10242-10275; *Angew. Chem. Int. Ed.* **2011**, *50*, 10064-10094.

[49] A. Coelho, *TOPAS: General Profile and Structure Analysis Software for Powder Diffraction Data; Bruker AXS GmbH: Karlsruhe, Germany* **2014**, *version 5*.

[50] S. Brunauer, P. H. Emmett, E. Teller, *J. Am. Chem. Soc.* **1938**, *60*, 309-319.

[51] L. Scharfenberg, R. Horn, *Chem. Ing. Tech.* **2017**, *89*, 1350-1359.

[52] A. V. Chichagov, A. B. Belonozhko, A. L. Lopatin, T. N. Dokina, O. L. Samokhvalova, T. V. Ushakovskaya, Z. V. Shilova, *Kristallographiya* **1990**, 35, 610-616.

[53] Z. Qu, M. Cheng, W. Huang, X. Bao, *J. Catal.* **2005**, *229*, 446-458.

[54] E. R. Jette, F. Foote, *J. Chem. Phys.* **1935**, *3*, 605-616.

[55] N. Koga, S. Yamada, T. Kimura, *J. Phys. Chem. C* **2013**, *117*, 326-336.

[56] W. Luo, W. Hu, S. Xiao, *J. Phys. Chem. C* **2008**, *112*, 2359-2369.

[57] A. J. Nagy, G. Mestl, D. Herein, G. Weinberg, E. Kitzelmann, R. Schlögl, *J. Catal.* **1999**, *182*, 417-429.

[58] Development of a TDS setup for powder samples, Scientific Instruments, manuscript in preparation

[59] X. Bao, M. Muhler, T. Schedel-Niedrig, R. Schlögl, *Phys. Rev. B* **1996**, *54*, 2249-2262.

[60] V. I. Bukhtiyarov, A. Knop-Gericke, in *Nanostructured Catalysts: Selective Oxidations*, The Royal Society of Chemistry, **2011**, pp. 214-247.

[61] J. L. Solomon, R. J. Madix, J. Stöhr, *J. Chem. Phys.* **1990**, *93*, 8379-8382.

[62] J. J. F. Scholten, J. A. Konvalinka, F. W. Beekman, *J. Catal.* **1973**, *28*, 209-220.

[63] G. C. Chinchen, C. M. Hay, H. D. Vandervell, K. C. Waugh, *J. Catal.* **1987**, *103*, 79-86.

[64] M. A. Vannice, in *Kinetics of catalytic reactions*, Springer, **2005**.

2.7 Supporting information

Table S4. SEM/EDX analysis of supported Ag (pre-)catalysts with standard deviations

sample	O [wt.-%]	Si [wt.-%]	Ag [wt.-%]
$AgNO_3/SiO_2$	54.22 ± 3.58	43.30 ± 3.93	2.48 ± 0.77
$Ag5/SiO_2$_400/1	58.24 ± 0.99	39.18 ± 0.59	2.58 ± 0.44
$Ag5/SiO_2$_500/1	55.88 ± 1.75	41.07 ± 0.80	3.05 ± 0.58
$Ag5/SiO_2$_600/1	53.53 ± 1.40	43.24 ± 1.46	3.23 ± 0.33

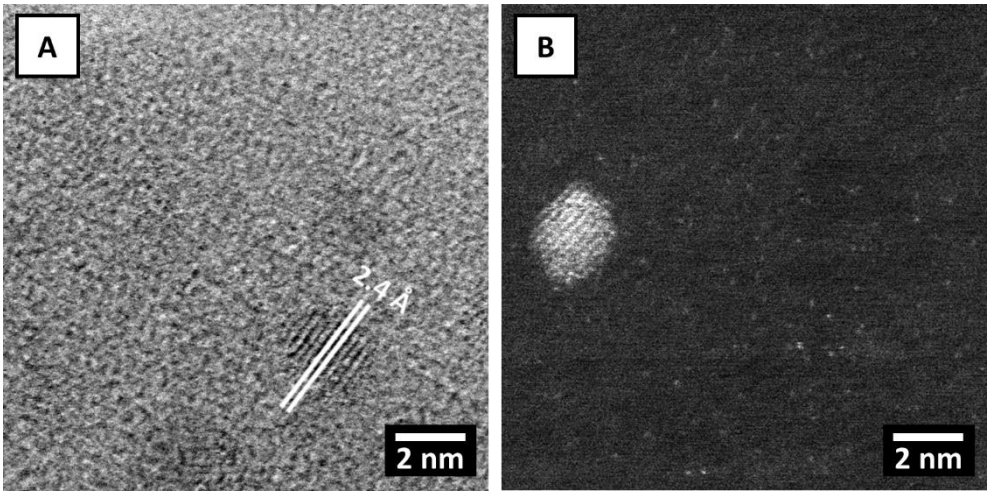

Figure S22. STEM images of $AgNO_3/SiO_2$ dried at 110/12. For the BF image (A) the d-spacing of the particle was measured to be 2.40 Å, being in good agreement with reference for Ag 111 (2.36 Å)[CH]. Bright particles in ADF image (B) refer to Ag.

[CH] A. V. Chichagov, A. B. Belonozhko, A. L. Lopatin, T. N. Dokina, O. L. Samokhvalova, T. V. Ushakovskaya, Z. V. Shilova, *Kristallographiya* **1990**, *35*, 610-616.

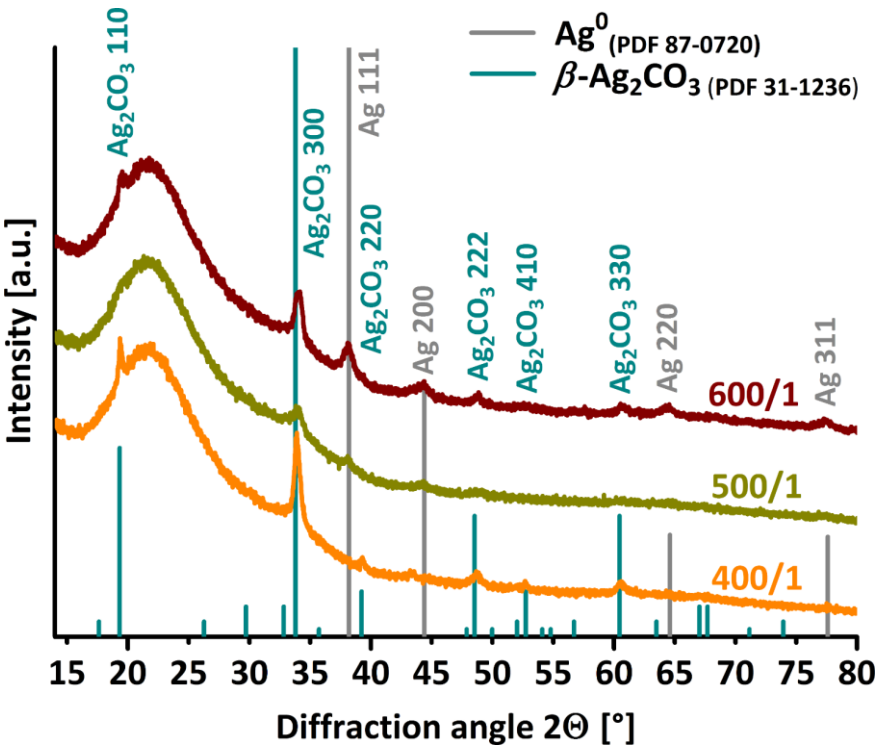

Figure S23. PXRD of 18 weeks aged Ag5/SiO_2 samples 400/1 (orange), 500/1 (yellow) and 600/1 (red). Beside the Ag^0 reflections (PDF 87-0720, grey), pronounced Ag_2CO_3 related reflections are observed (PDF 31-1236, dark cyan).

The approach for the synthesis of a α-Al_2O_3 supported catalyst using $AgNO_3$ dissolved in H_2O as impregnation solution was identical to the one for Ag5/SiO_2 catalysts, with the difference of using an impregnation solution according to a final Ag loading of 15.5 wt.-%. Corresponding STEM and SEM images are shown in Figure S24 and Figure S25.

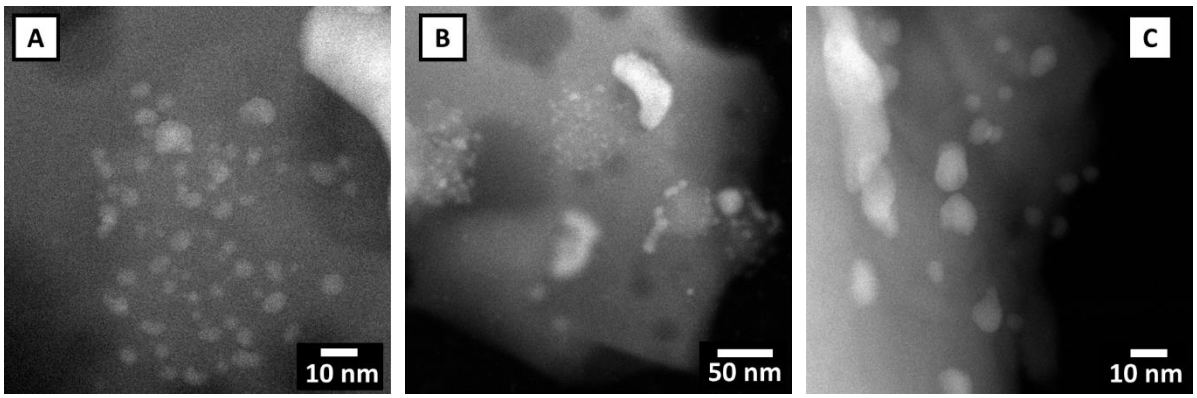

Figure S24. STEM-ADF images of Ag15/α-Al_2O_3 synthesized using $AgNO_3$ as Ag source. Bright spots refer to metallic Ag.

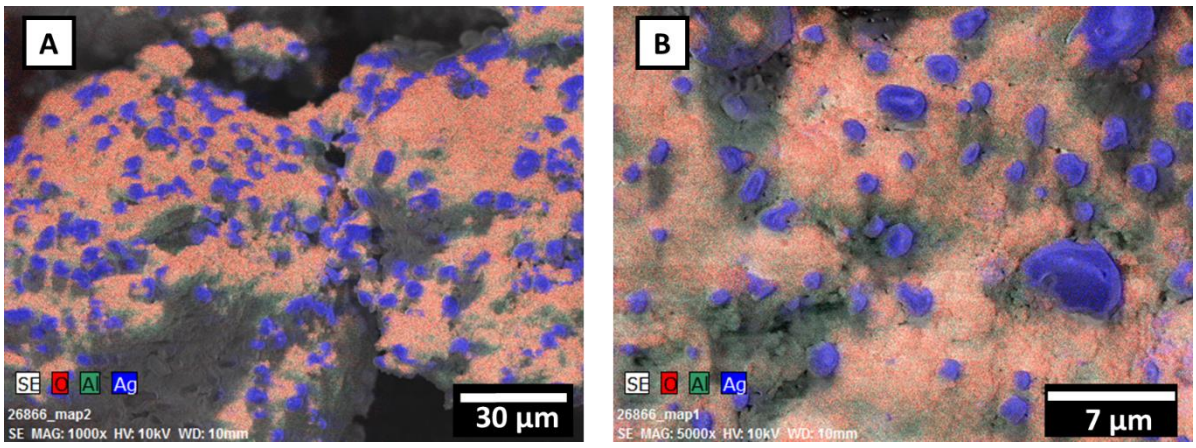

Figure S25. SEM-EDX mapping of oxygen (red), alumina (green) and silver (blue) with 1k (A) and 5k (B) magnification for Ag15/α-Al_2O_3 synthesized using $AgNO_3$ as Ag source.

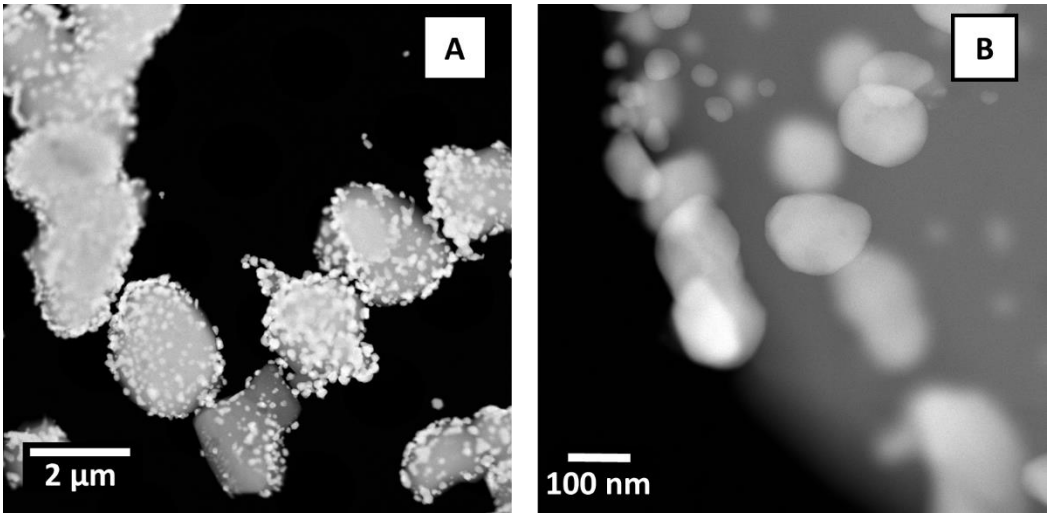

Figure S26. STEM image of reference sample Ag15/α-Al_2O_3 based on a Ag oxalate impregnation approach. Main PS is detected to be in the range of 100 – 300 nm, with a few nanoparticles of around 20 – 40 nm in size.

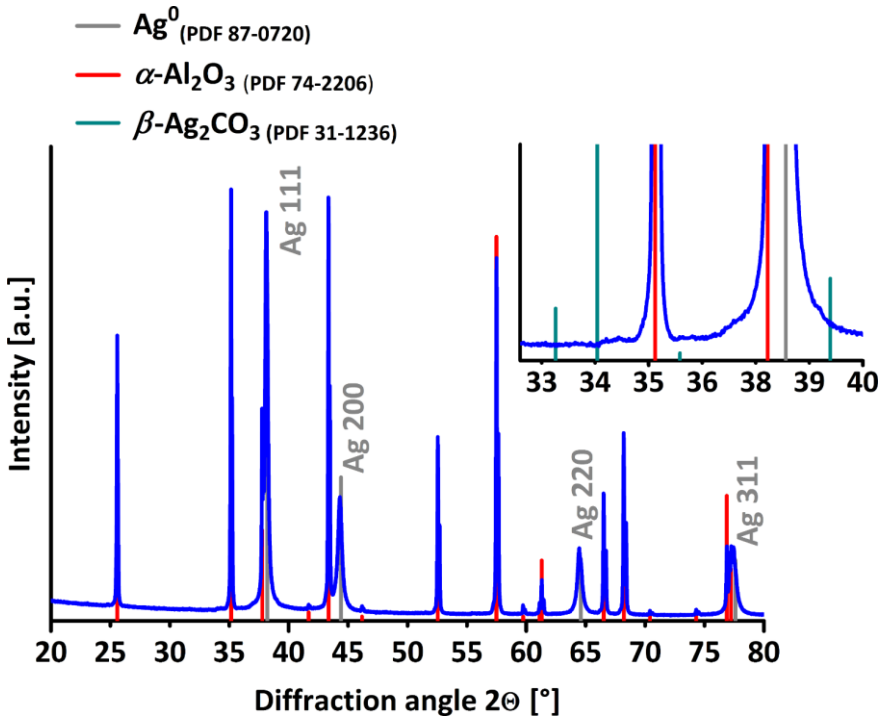

Figure S27. PXRD of reference catalyst Ag15/α-Al_2O_3 (blue) using Ag oxalate as Ag source. Also shown are references for Ag^0 (grey, PDF 87-0720), α-Al_2O_3 (red, PDF 74-2206) and β-Ag_2CO_3 (dark cyan, PDF 31-1236).

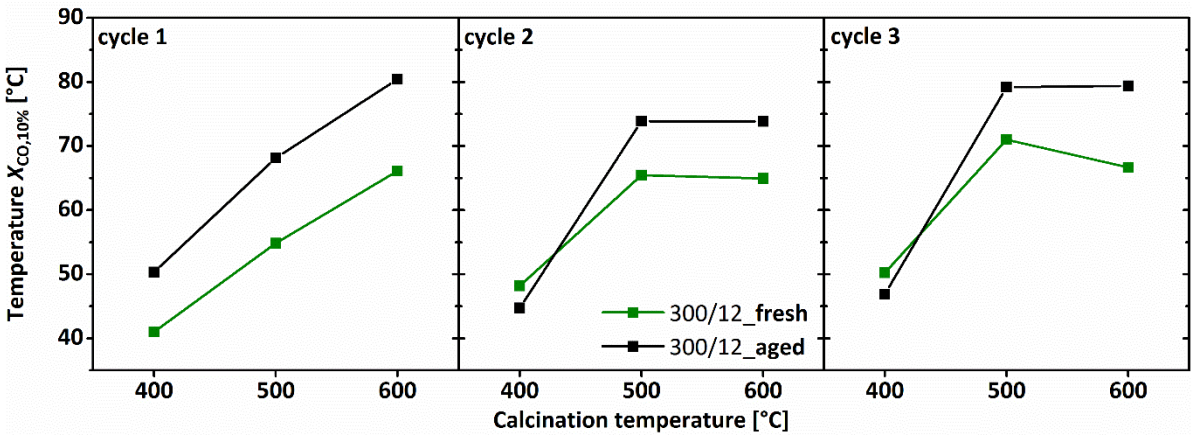

Figure S28. Temperature for 10 % CO conversion ($X_{CO,10\%}$) vs. calcination temperature of catalysts with a dwell time of 1 h and 400 °C, 500 °C and 600 °C calcination temperature for cycle one to three. Catalysts were *in-situ* pre-treated at 300 °C for 12 h. Shown are fresh samples (green) and aged samples (black) after 18 weeks. The increased activity for aged sample calcined at 400 °C for cycle two and cycle three is based on the reduced sintering induced by the 300/12 pre-treatment conditions. Less energy reaches the particle since the thermal energy of the pre-treatment is used to decompose the formed Ag_2CO_3, not being present for the fresh sample.

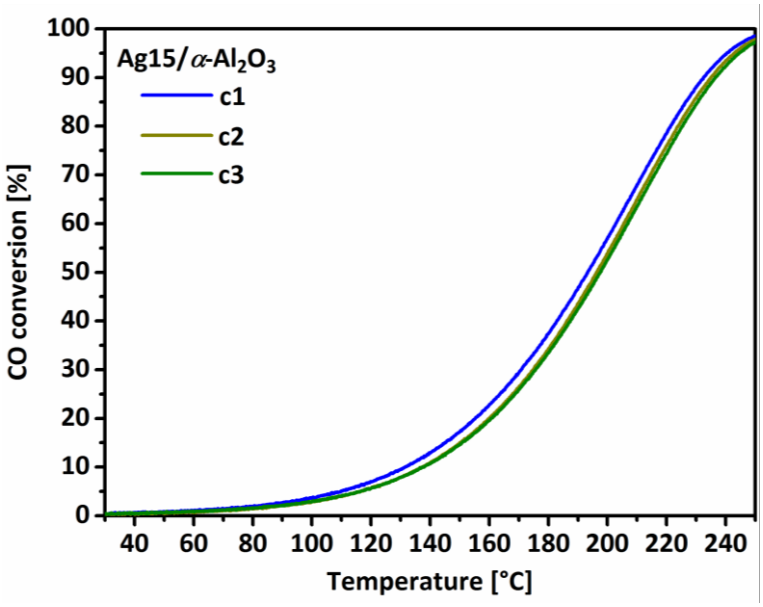

Figure S29. CO oxidation of Ag-oxalate based Ag15/α-Al_2O_3 reference, pre-treated at conditions of 300/3. Shown are cycles one to three (c1 – c3).

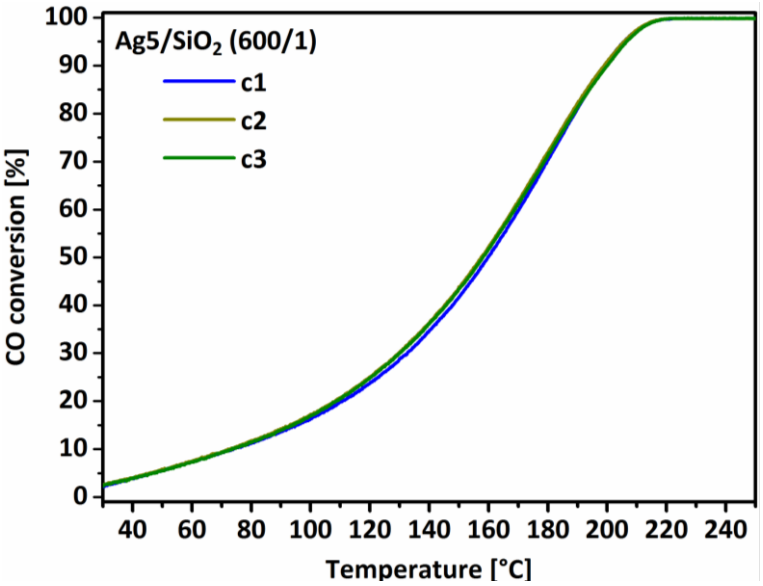

Figure S30. CO oxidation of Ag5/SiO_2 catalyst calcined at conditions of 600/1 and pre-treated at 300/3. Shown are cycles one to three (c1 – c3).

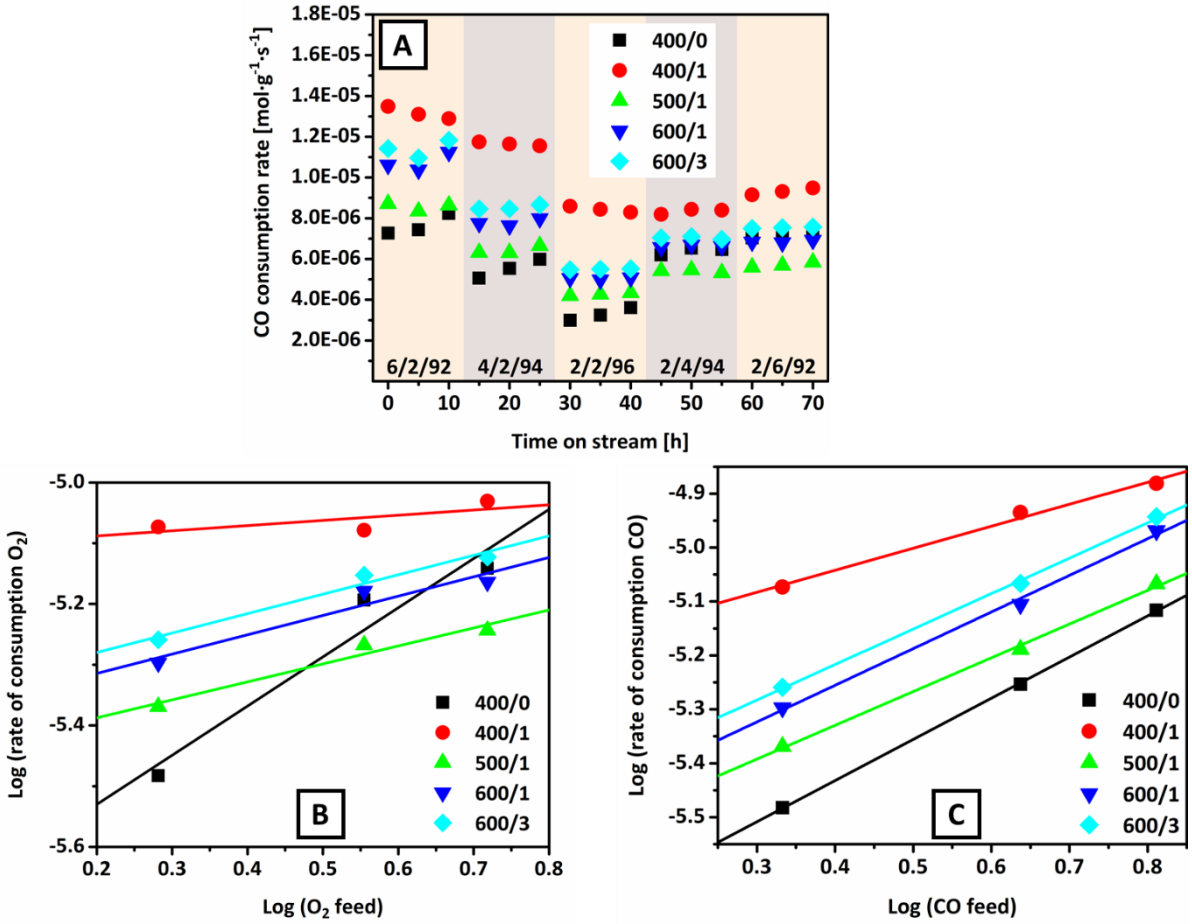

Figure S31. CO oxidation test for determination of O_2 and CO reaction order. The complete test is shown in (A) with CO consumption rate and time on stream for different feed compositions for CO [%] / O_2 [%] / N_2 [%] concentrations. Also shown are the corresponding plots of the logarithmic rates versus the logarithmic concentration of oxygen (B) and CO (C).

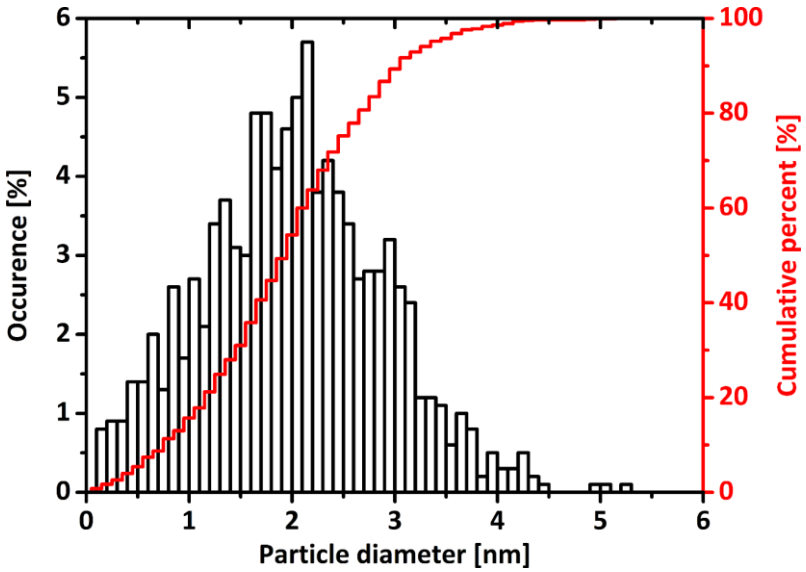

Figure S32. PS distribution from STEM with 0.1 nm bin size for dried sample Ag5/SiO_2 after *in-situ* calcination at 600/1 conditions in the TDS setup. Median PS is 2.0 nm with a maximum PS of 5.2 nm.

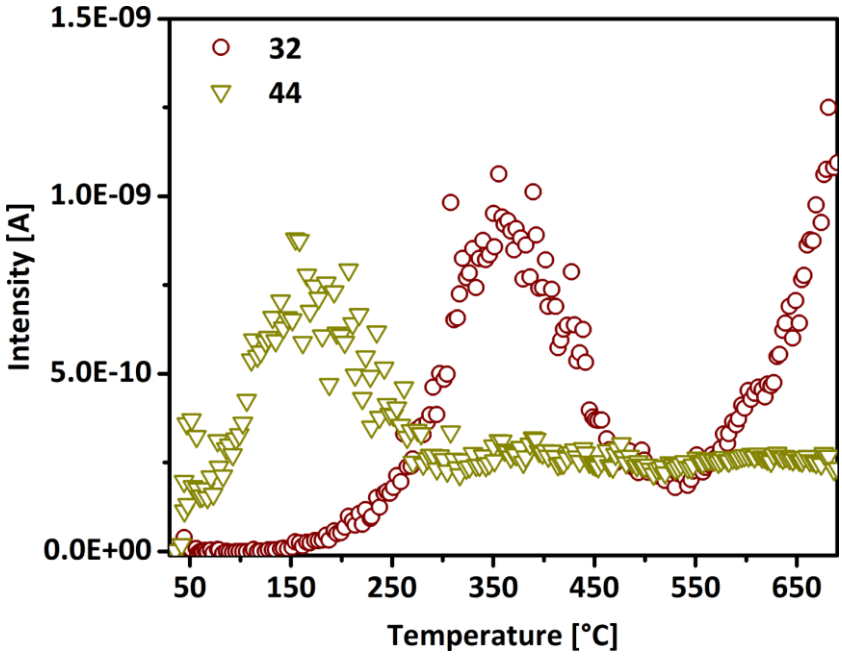

Figure S33. TDS of an *ex-situ* calcined (600/1) $Ag5/SiO_2$ catalyst with m/z = 44 (yellow) and 32 (red).

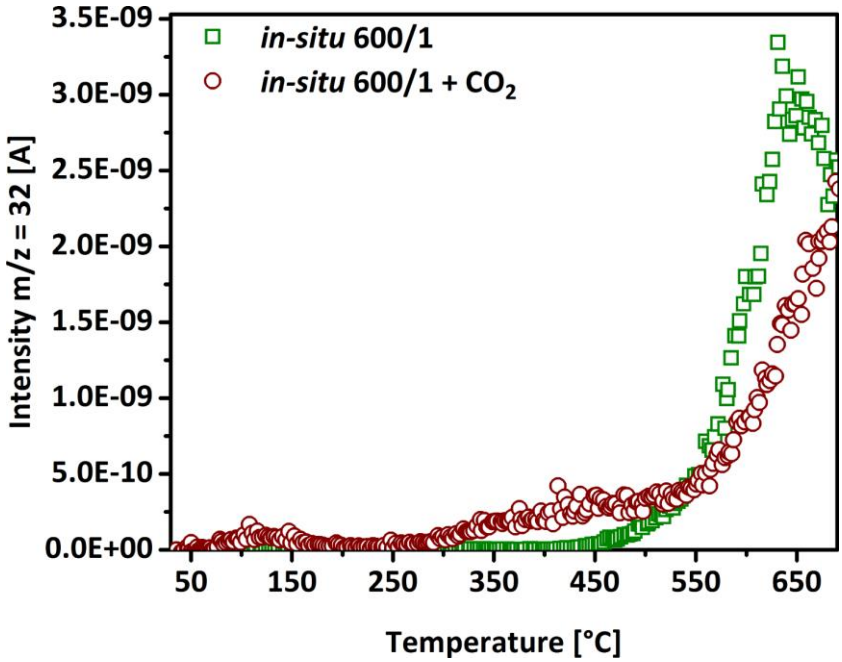

Figure S34. O_2-TDS of *in-situ* calcined (600/1) $AgNO_3/SiO_2$ (green) and *in-situ* calcined sample with additional CO_2 exposure (red).

Temperature programed reduction (TPR) was performed in 0.25 % H_2 diluted in Ar with 80 ml·min^{-1} up to 790 °C with a heating rate of 5 °C·min^{-1} using a fixed bed reactor (TPDRO-1100, CE INSTRUMENTS) with 100 mg sample mass in a quartz plug-flow U-tube reactor. The H_2 consumption was monitored with a thermal conductivity detector (X-Stream XE, EMERSON/ROSEMOUNT) and a mass spectrometer to also analyze the evolution of additional species like CO, CO_2, H_2O, NO and O_2. The results are shown in Figure S35.

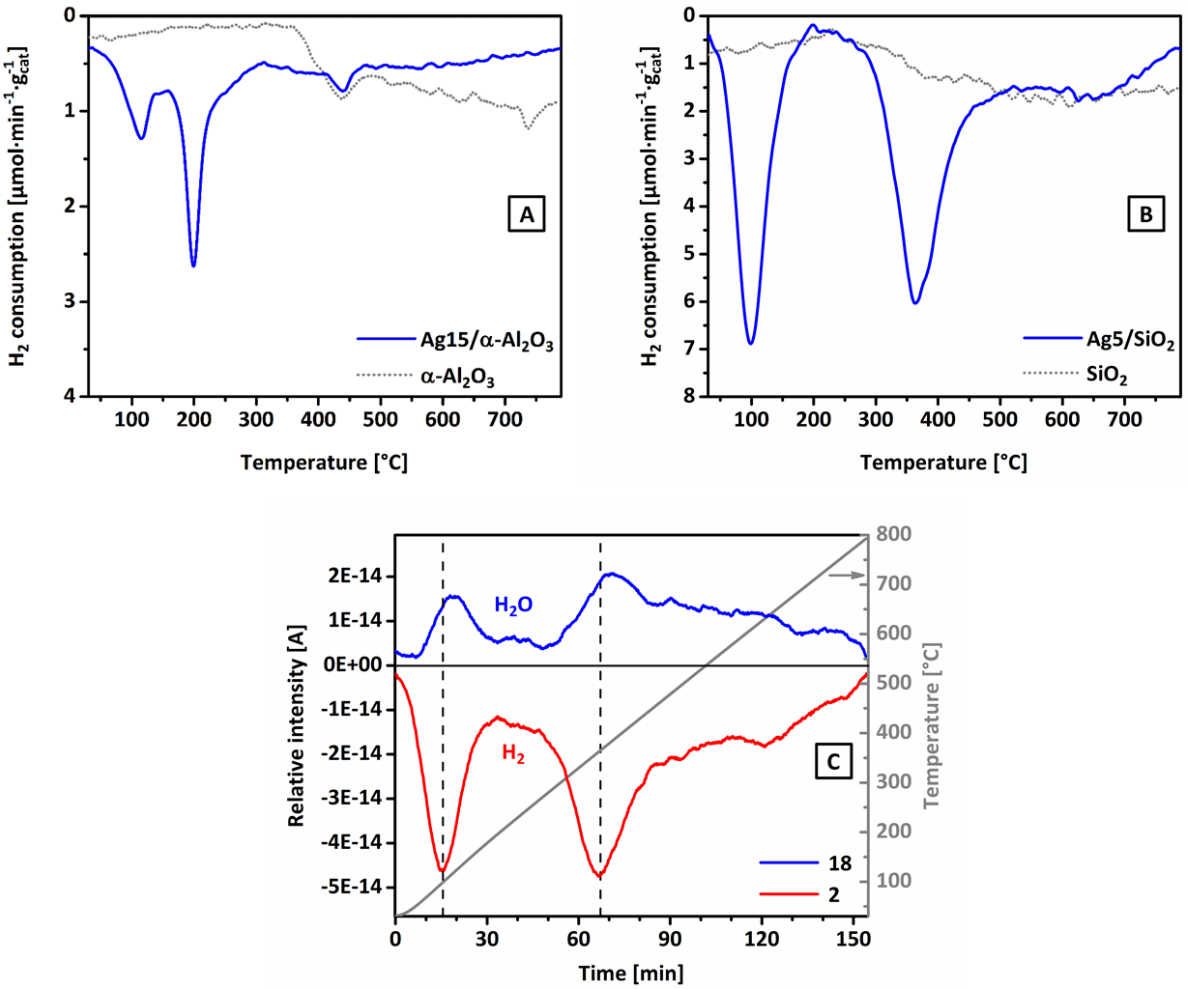

Figure S35. H_2-TPR of sample Ag15/α-Al_2O_3 (A) and Ag5/SiO_2 (B) after pre-treated at 200/12. Catalysts are shown in blue with corresponding supports in grey dots. Also shown are the to (B) corresponding mass changes for mass m/z = 18 (blue, H_2O) and m/z = 2 (red, H_2) with temperature in grey. Hydrogen consumption is correlated to water evolution, which indicates the reaction of hydrogen and oxygen. No other masses could be correlated to the shown hydrogen consumption.

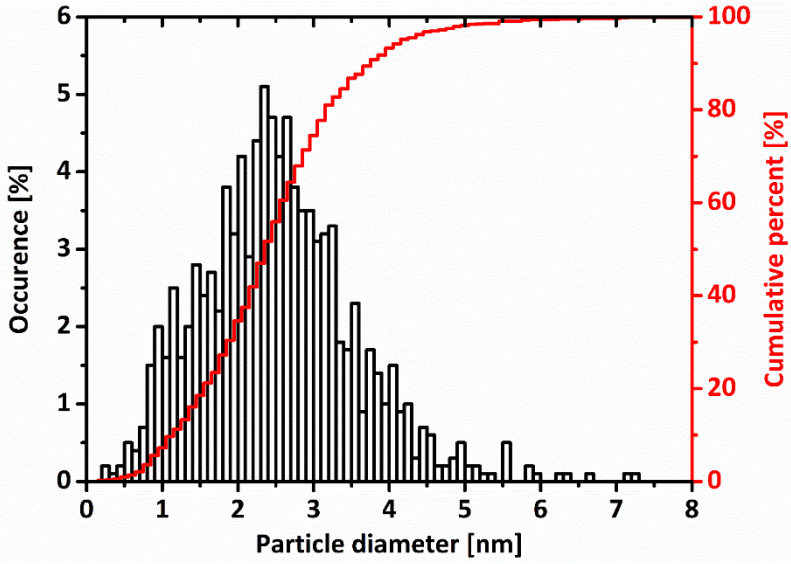

Figure S36. PS distribution from STEM with 0.1 nm bin size for dried sample Ag5/SiO_2 after *in-situ* 600/1 treatment at 10^{-8} mbar and H_2 reduction at 400/1. After both treatments a subsequent microcalorimetric O_2 adsorption measurement at 200 °C was performed.

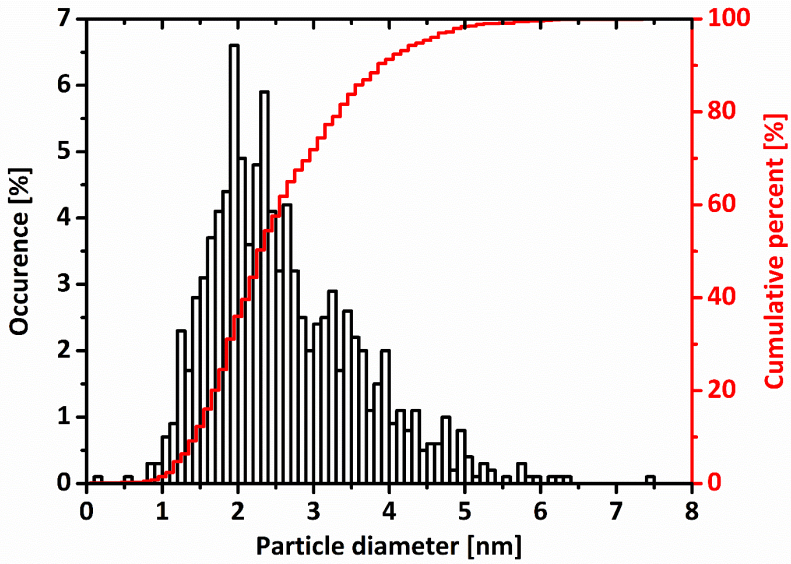

Figure S37. PS distribution from STEM with 0.1 nm bin size for sample Ag5/SiO_2 500/1. Median PS was calculated to 2.4 nm.

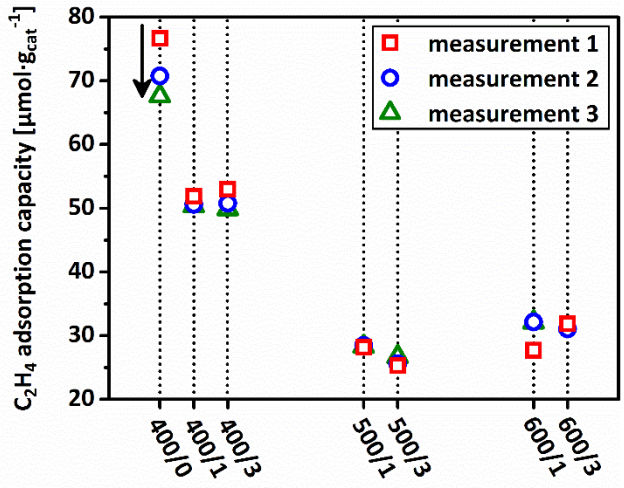

Figure S38. C_2H_4 adsorption capacities of $Ag5/SiO_2$ catalysts calcined at 400 °C, 500 °C and 600 °C with a dwell time of 0 h (only for 400 °C), 1 h and 3 h. Shown are the three individual measurements for each sample.

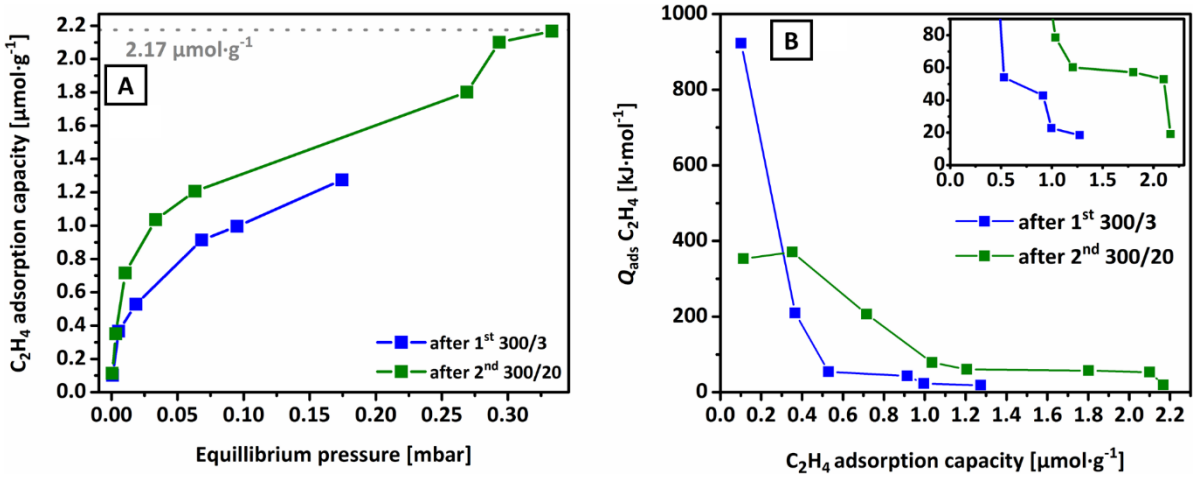

Figure S39. Microcalorimetric C_2H_4 adsorption for catalyst $Ag15/\alpha\text{-}Al_2O_3$. After synthetic air pre-treatments at conditions of 300/3 (blue lines) followed by 300/20 a distinct plateau is detected (green line) with a C_2H_4 adsorption capacity of 2.17 µmol·g^{-1} (A) which is used for Ag surface area determination. The corresponding high integral heat evolutions (B) evolve due to very long interaction times between C_2H_4 and the Ag catalyst which creates small heat evolution events over a long time, thereby increasing the integral heat.

DFT calculations:

The Quantum ESPRESSO package [QE] was employed for all DFT calculations using ultrasoft pseudopotentials and the Perdew, Burke, and Ernzerhof [PBE] exchange and correlation potential. Complete details of the approach and investigated structures have been previously described, see [JR]. Briefly, adsorption energies were computed using five layer silver slabs separated by ~10 a.u. of vacuum using a kinetic energy (charge density) cutoff of 30 Ry (300 Ry). A **k**-point mesh equivalent to 12×12 for the 1×1 surface unit cell was employed with Marzari-Vanderbilt [MV] cold smearing using a smearing parameter of 0.02 Ry. The energy of oxygen was taken from a calculation on a triplet O_2 molecule at the Γ point with a 40^3 a.u.^{3} cubic cell.

[QE] P. Giannozzi, S. Baroni, N. Bonini, M. Calandra, R. Car, C. Cavazzoni, D. Ceresoli, L. G. Chiarotti, M. Cococcioni, I. Dabo, A. D. Corso, S. d. Gironcoli, S. Fabris, G. Fratesi, R. Gebauer, U. Gerstmann, C. Gougoussis, A. Kokalj, M. Lazzeri, L. Martin-Samos, N. Marzari, F. Mauri, R. Mazzarello, S. Paolini, A. Pasquarello, L. Paulatto, C. Sbraccia, S. Scandolo, G. Sclauzero, P. A. Seitsonen, A. Smogunov, P. Umari, M. R. Wentzcovitch, QUANTUM ESPRESSO: a modular and open-source software project for quantum simulations of materials, *J. Phys. Condens. Matter* **2009**, *21*, 395502.

[PBE] J. P. Perdew, K. Burke, M. Ernzerhof, Generalized Gradient Approximation Made Simple, *Phys. Rev. Lett.* **1996**, *77*, 3865-3868.

[JR] T. E. Jones, T. C. R. Rocha, A. Knop-Gericke, C. Stampfl, R. Schlögl, S. Piccinin, Thermodynamic and spectroscopic properties of oxygen on silver under an oxygen atmosphere, *Phys. Chem. Chem. Phys.* **2015**, *17*, 9288-9312.

[MV] N. Marzari, D. Vanderbilt, A. De Vita, M. C. Payne, Thermal Contraction and Disordering of the Al(110) Surface, *Phys. Rev. Lett.* **1999**, *82*, 3296-3299.

3 Reactivity of Ag nanoparticles in ethylene epoxidation: How model catalysts unravel the selective state of Ag

3.1 Abstract

In the present work, we report on the investigation of model catalysts consisting of Ag nanoparticles below 6 nm and their performance in the ethylene epoxidation reaction under industrially relevant conditions. The dependence of the catalytic performance on the oxygen concentration in/on Ag is demonstrated. Applying a combination of thermal desorption spectroscopy and kinetic investigations the relevant oxygen species responsible for the CO_2 formation and inhibition of the overall catalytic activity are identified. The abundance of those species strongly depends on the pre-treatment and reaction conditions. Isotope experiments using $^{18}O_2$ and $C^{18}O_2$ are conducted to gain insight on the nature and location of oxygen in/on the Ag nanoparticles. By comparison to a conventional Ag/α-Al_2O_3 catalyst, it is evidenced that a low oxygen concentration in/on Ag leads to the highest selectivity. This study provides fundamental understanding on the performance of supported Ag particles in the ethylene epoxidation independent of their particle size.

3.2 Introduction

An intuitive approach to maximize the conversion of a catalyst is the increase of its active surface area to provide more catalytically relevant reaction sites. This is e.g. accessed by nanostructuring which leads to an increase in reactivity per employed mass relative to macroscopic crystals of the same substance.[1] Besides, the formation of nanoparticles of typically 1 – 10 nm in size entail certain phenomena that are summarized as particle size effect.[2, 3] This property has already been observed for quite a number of supported metal based catalysts like Co[4], Ni[5], Pd[6], Pt[7], Cu[8], Ag[9] and Au[10]. The overall consent is that the particle size (PS) effect strongly depends on the kind of reaction as well as the active material, thereby leading to beneficial or disadvantageous effects. A widely discussed PS effect is observed for Ag in the partial oxidation of ethylene to ethylene epoxide (EO). After more than 40 years of research[11, 12] it is still under debate if an unfavorable Ag particle size effect exists and whether it contributes to the reduction of the overall selectivity. Further, it remains unclear whether only the activity or also the selectivity towards EO is influenced by the Ag particle size.

An overview of selected results dealing with the influence of the Ag particle size for supported Ag catalysts in the epoxidation of ethylene is shown in Figure 40. Wu and Harriott[12] studied supported Ag on silica in the range of 3 – 50 nm Ag PS and observed highest conversions of ethylene, $X(C_2H_4)$, at around 5 – 6 nm, but with very low selectivity to ethylene epoxide, S(EO), which steadily increased with increasing PS.

Verykios *et al.*[13] investigated larger Ag PS starting from 30 nm, observing the same phenomenon for $S(EO)$ and a minimum in $X(C_2H_4)$ in the range of 50 – 70 nm Ag PS. This is in reasonable agreement with the observations of Wu and Harriott. However, since Verykios *et al.* normalized their rates per square meter "free-metallic-silver surface area" determined by selective oxygen chemisorption, any comparison in terms of $X(C_2H_4)$ has to be interpreted with caution. Investigations of Cheng and Clearfield[14] resulted in a maximum of $S(EO)$ and $X(C_2H_4)$ at around 50 nm, with a decrease in $S(EO)$ for larger PS being in contrast to the mentioned previous studies. However, Lee *et al.*[15] observed again a steady increase in $S(EO)$ for increasing PS, but this time from 6 – 50 nm and in the range of 50 – 100 nm $S(EO)$ remained unchanged. The $X(C_2H_4)$ showed a maximum at 40 – 50 nm in the case of corundum supported Ag and a plateau starting at around 60 nm for silica supported Ag. The Ag on corundum support performed similar to results by Cheng and Clearfield. Goncharova *et al.*[16] were able to show a steady increase in $S(EO)$ from 10 – 100 nm, which is congruent to the reported results by Wu and Harriott and Verykios *et al.*, and a maximum in $X(C_2H_4)$ at around 50 nm in agreement with Cheng and Clearfield. The listed results were obtained during a period of 20 years and it took another 17 years until the group of Petra de Jongh[11] investigated the PS of Ag regarding its influence on the ethylene epoxidation reaction. In contrast to the previous investigations, the $S(EO)$ at a constant low conversion of 2.8 % were compared, resulting in constant $S(EO)$ values. As a consequence, no particle size effect on the selectivity in the range of 20 – 200 nm Ag PS was observed. The achieved $X(C_2H_4)$ were again in agreement with previous reported studies, reaching its maximum for a Ag PS of 60 – 70 nm.

Since the synthesis of Ag particles below 10 nm is difficult to accomplish, only a limited number of studies are available. Demidov and co-workers[17] investigating the model catalyst Ag/HOPG which stayed inactive for an average Ag PS of 8 nm. In contrast, 40 nm Ag particles on HOPG showed the formation of ethylene epoxide. These results stand contradictory to the report of Fotopoulus *et al.*[18], where a catalyst with 9 nm Ag particles on MCM-41 showed a $X(C_2H_4)$ of up to 65 % with $S(EO)$ of 30 – 35 %. Such reasonable performances were comparable to the reference Ag/α-Al_2O_3 catalyst with Ag particle sizes below 60 nm.

The essence of more than 40 years of research regarding the PS effect of Ag in the ethylene epoxidation reaction is unclear. The trends of the $S(EO)$ and $X(C_2H_4)$ curves illustrated in Figure 40 are arbitrary with respect to the Ag PS regimes. A maximum for $X(C_2H_4)$ for Ag PS around 50 – 60 nm, as well as a poor $S(EO)$ for small Ag particles seem to be consent. But, however the origin of the multiply observed effects for different catalysts is still not unraveled and rather contradictory.

An explanation for the inconsistent situation in terms of a Ag PS effect might be the broad PS distributions achieved so far. Furthermore, the achieved Ag PS were above the relevant range of up to 6 nm for which a dependence on catalytic performance should be observable.[9, 19-22] Besides, related oxidation reactions might

also be helpful and serve as orientation for any PS effect. Lei *et al.*[9] used Ag cluster-based catalysts supported on silicon wafer in the range of 0.5 – 3.5 nm. Those small clusters and particles were active and selective in epoxidation of propylene with high turnover rates. Comparable results were achieved in chapter 2 for supported Ag catalysts in the oxidation of CO. *In-situ* synthesized Ag clusters < 1 nm showed exceptionally high CO oxidation rates compared to Ag nanoparticles of 1 – 6 nm. Further, the Ag clusters and particles showed much higher CO oxidation rates than a Ag/α-Al_2O_3 reference catalyst with 40 nm crystalline domain size.

Since both studies showed that Ag nanoparticles are able to perform oxidation reactions, the motivation of this study was to transfer these performances to the epoxidation of ethylene and to unravel the long-standing question of a Ag PS effect, respectively. Applying the in chapter 2 introduced synthesis strategy, SiO_2 supported Ag nanoparticles up to 6 nm with a narrow PS distribution are investigated. To ensure the relevance of the conducted study for any catalytic discussion, the samples are tested under industrially relevant conditions of high pressure. The performances of the Ag/SiO_2 catalysts are compared to a conventional Ag/α-Al_2O_3 catalyst. All samples are thoroughly analyzed before and after the catalytic testing with powder X-ray diffraction (PXRD) and transmission electron microscopy (TEM). Further, thermal desorption spectroscopy (TDS) allows to identify the relevant Ag-O interactions related to the catalytic results. To finally discriminate between different oxidation effects of the supported catalysts, ethylene epoxide decomposition tests are applied.

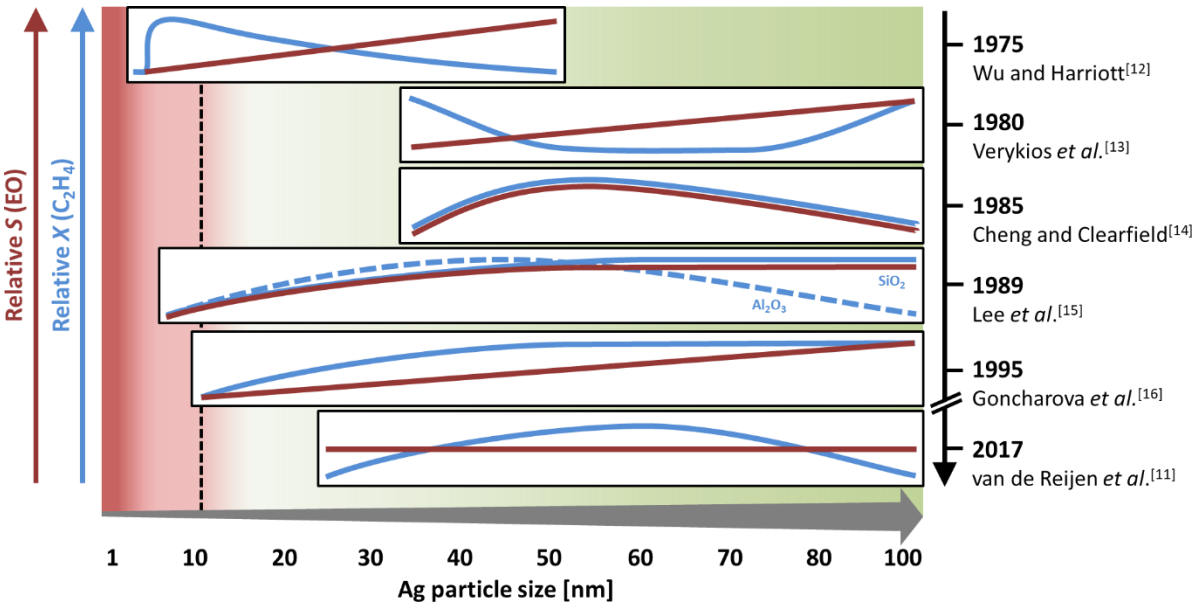

Figure 40. Overview of the catalytic activity of supported Ag catalysts in the epoxidation of ethylene. The reports are arranged regarding their investigated Ag particle size up to 100 nm schematically showing their conversion of ethylene X(C_2H_4), their selectivity to ethylene epoxide S(EO) and the year of appearance.

3.3 Experimental section

Synthesis of Ag/SiO_2 and $Ag/\alpha\text{-}Al_2O_3$ is performed using a vacuum assisted impregnation technique, which was applied to achieve a controlled distribution on the support. For the silica (Aerosil 300, DEGUSSA, hydrophilic fumed silica powder, primary particles: spherical, 7 – 40 nm, no porosity) supported catalyst $AgNO_3$ was dissolved in water according to 5 wt.-% Ag loading (labeled as $Ag5/SiO_2$) and used as impregnation solution. The amount of H_2O needed for impregnation was determined by identifying the "solvent capacity volume". The impregnated support was dried, transferred into 100 – 200 µm sieve fraction and subsequently calcined at 600 °C for 1 h in a rotating tube furnace with a constant flow of 21 % O_2 in Ar (300 ml·min^{-1}) with a heating rate of 2 °C·min^{-1}.

For the synthesis of the industrial reference sample, 15 wt.-% Ag was loaded on α-Al_2O_3 using an Ag oxalate based precursor according to patent literature, labeled as $Ag15/\alpha\text{-}Al_2O_3$.[23] The α-Al_2O_3 support was then double impregnated with the silver oxalate-ethylenediamine solution followed by a calcination under air.

Ethylene epoxidation was performed in a stainless steel plug flow reactor (inner diameter 4 mm) at 17.5 bar absolute pressure and a gas composition of 7/8/50/35 for $O_2/Ar/N_2/C_2H_4$ at a GHSV of 4850 h^{-1}. The temperature was stepwise raised with 1 °C·min^{-1} heating rate and a dwell time for each temperature step of 6 h. The composition of the exhaust gases was analyzed online using a gas chromatograph (AGILENT 7890N) equipped with a flame ionization detector (FID) and thermal conductivity detector (TCD).

Powder X-ray diffraction (PXRD) patterns were recorded using a BRUKER AXS D8 ADVANCE II THETA/THETA diffractometer in Bragg-Brentano geometry using Ni filtered Cu $K_{\alpha 1+2}$ radiation and a position sensitive LYNXEYE silicon strip detector. The sample powder was filled into the recess of a cup-shaped sample holder, the surface of the powder bed being flush with the sample holder edge (front loading). The resulting diffractograms were analyzed by full pattern fitting using the TOPAS software[24] to extract lattice parameters, crystallite sizes and Ag loading.

Scanning transmission electron microscopy (STEM) imaging was performed using a double Cs corrected JEM-ARM200CF (JEOL) operated at 200 kV and equipped with ADF (annular dark-field) and BF (bright-field) detectors. Samples were prepared by direct deposition of dry powder onto a QUANTIFOIL Au holey grid. For the resulting histograms, the diameter of 1000 particles was measured for each sample.

Thermal desorption spectroscopy (TDS) was applied for the temperature programmed desorption of oxygen. Therefore, a self-constructed setup which enables the testing of powder samples was used. The setup was equipped with mass flow controllers, an IR-light furnace (BEHR IRF 10) and a mass spectrometer (PFEIFFER VACUUM QME 200). The powder sample was placed on a small quartz-glass boat which is placed

in a quartz tube (inner diameter of 14 mm, outer diameter of 20 mm, length of 450 mm) located inside of furnace and connected to the system using Ultra Torr vacuum fittings. Prior to the desorption experiment the samples were pre-treated at 1 bar in 25 % O_2 in Ar at a flow of 100 ml·min^{-1} for 12 h at 210 °C, which cleaned the surface of the sample and saturates the Ag with oxygen (surface and bulk). The gases were detected using the mass spectrometer leak valve. Afterwards the system was stepwise brought to 9·10^{-7} mbar and directly connected to the mass spectrometer. The desorption experiment was conducted at a heating rate of 25 °C·min^{-1} up to 700 °C. All masses and the temperature were monitored online.

Inductive coupled plasma – optical emission spectroscopy (ICP-OES) was used to determine the Ag loading of the catalysts. Therefore, the sample was solubilized using LiF, nitric acid and water at 230 °C, diluted with water and analyzed with a PERKIN ELMER ICP OES Optima 8300.

3.4 Results and discussion

Table 5. Overview of investigated catalysts with nominal and experimentally determined Ag loading (ICP-OES and PXRD), Ag domain size (PXRD full pattern fitting) support BET surface area (SA_{BET}) and internal number

catalyst	Ag loading [wt.-%] (nom.)	Ag loading [wt.-%] (exp.)	Ag domain size [nm]	SA_{BET} supports [$m^2 \cdot g^{-1}$]	FHI #
Ag5/SiO_2	5.0	4.4[*1]	6.5±0.7	328	29714
Ag15/α-Al_2O_3	15.5	12.4[*1] 13.9[*2]	39.4±4.2	1.0	29934

[*1]: ICP-OES, [*2]: PXRD (Rietveld)

3.4.1 Sample preparation and characterization

According to the established synthesis protocol in chapter 2, 5 wt.-% Ag supported on SiO_2 (Ag5/SiO_2) was prepared. In addition, a reference sample with 15.5 wt.-% Ag supported on α-Al_2O_3 (Ag15/α-Al_2O_3) was synthesized, following Rosendahl *et al.*[23] The corresponding PXRD are shown in Figure 10. The Ag15/α-Al_2O_3 catalyst exhibits slightly broadened Ag reflections in comparison to Ag powder reference (Figure 10, green pattern), together with reflections of α-Al_2O_3. The broadening is explained by the reduced domain size which was determined to 39.4±4.2 nm by full pattern fitting. Ag5/SiO_2 shows a pronounced broadening of the Ag reflections, a direct indication of the smaller domain sizes of 6.5±0.7 nm. The SiO_2 support is responsible for the diffuse reflection visible in the range of 30 – 40° 2Θ. The Ag lattice parameters are also determined for Ag5/SiO_2 and Ag15/α-Al_2O_3 as 4.089±0.012 Å and 4.08603±0.00009 Å, respectively. Within the uncertainty of the fitted results, the lattice parameters are in good agreement with reported reference of 4.086 Å[25] for Ag^0.

Complementary to PXRD, STEM analysis was performed in order to extract the PS information illustrated in Figure 42. For Ag15/α-Al_2O_3 (A and B) the Ag particles are well distributed over the support with dominant

particle sizes between 100 – 300 nm (Figure 42A) and a minor fraction of particles in the range of 20 – 40 nm (Figure 42B). The main particle sizes determined by STEM are larger than the domain sizes determined by PXRD, indicating that the fraction of larger particles have been formed by sintering. For Ag5/SiO_2 (C) the Ag particles are homogeneously distributed over the whole support with a very narrow size distribution. The corresponding histogram is presented in Figure 42D, with a median particle size of 2.3 nm and a standard deviation of 0.72 nm. The absence of Ag particles larger than 5.8 nm is in good agreement with the results from PXRD (domain sizes of 6.5±0.7 nm).

An overview of relevant parameters of the used catalysts is presented in Table 5. The Ag loading was experimentally determined by ICP-OES and resulted in 4.4 wt.-% Ag for the Ag5/SiO_2 sample and 12.4 wt.-% for Ag15/α-Al_2O_3. In addition, the quantitative PXRD analysis (Rietveld method) for Ag15/α-Al_2O_3 determined the Ag loading to 13.9 wt.-%. Generally, the quantitative assessments are in good agreement with the nominal values.

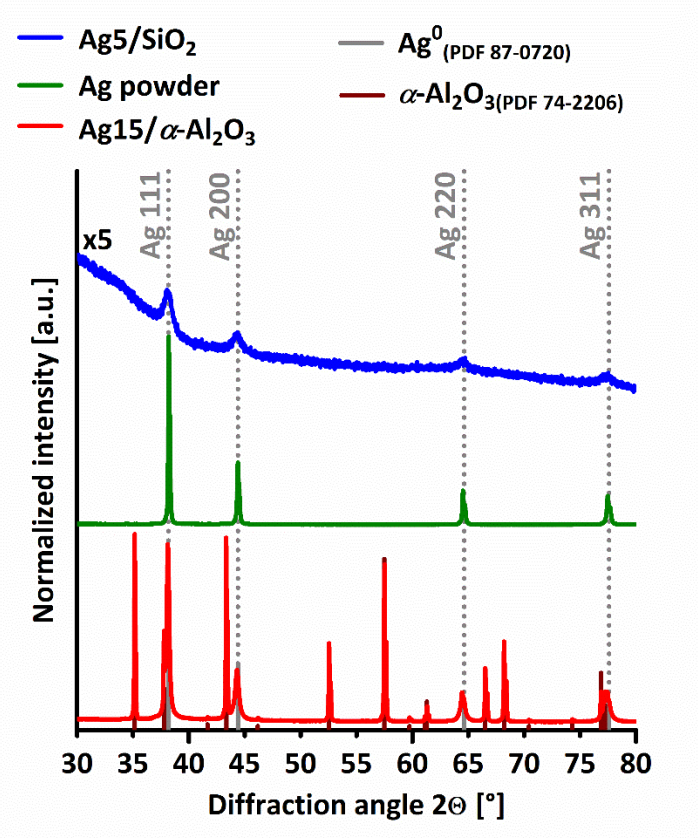

Figure 41. PXRD of Ag5/SiO_2 (blue, 5 times amplified), Ag powder as reference (green), Ag15/α-Al_2O_3 (red) and the database entries for Ag^0 (grey, PDF 87-0720) and α-Al_2O_3 (dark red, PDF 74-2206).

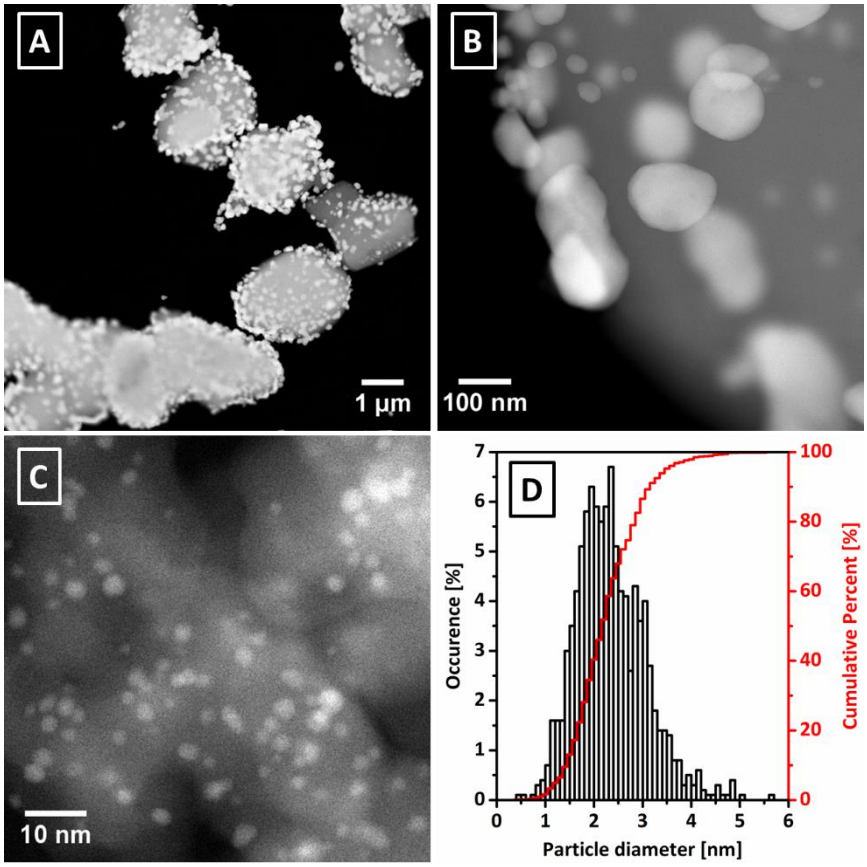

Figure 42. STEM-ADF images of catalyst Ag15/α-Al_2O_3 (A and B) and Ag5/SiO_2 (C). The bright spots refer to Ag particles. For catalyst Ag5/SiO_2 also the particle size distribution is shown (D).

3.4.2 Ethylene epoxidation tests

All catalysts were tested in the epoxidation of ethylene to ethylene epoxide (EO). The applied gas feed, temperatures and pressures are chosen equally to the industrial process (see also experimental part).[23] As surface purification step, a pre-treatment temperature of 210 °C is chosen, which corresponds to the decomposition temperature of Ag_2CO_3 of 175 °C – 225 °C[26] and Ag_2O of around 200 °C[27]. In the following, the pre-treatment atmospheres, which have been varied for Ag5/SiO_2 sample from N_2 to O_2 (synthetic air), is part of the label, i.e. Ag5/SiO_2-N_2 or Ag5/SiO_2-O_2 (not necessary for the reference catalyst only treated in N_2). For an improved clarity, the following figures contain only extracted results. Any further information is placed in the supporting information (Figure S51 – Figure S54).

Figure 43 shows the selectivity towards EO, S(EO), as a function of the oxygen conversion, $X(O_2)$, at various temperatures, dwelled for 6 h each, for the Ag5/SiO_2-N_2, Ag5/SiO_2-O_2 and the Ag15/α-Al_2O_3 reference catalyst. The performance of the Ag15/α-Al_2O_3 catalyst in steady-state follows a typical S to X behavior, meaning a lower selectivity at higher conversions indicated by the red line in Figure 43.

The Ag5/SiO_2-N_2 catalyst (Figure 43, blue) shows a pronounced activation period for which the S(EO) steadily increases with time and temperature, namely from 48 % at 150 °C to a maximum S(EO) of 62 % at

180 °C, which is also interpreted as successful activation. The $X(O_2)$ shows only minor changes up to 180 °C (around 5 – 8 %). An ongoing increase of the temperature leads to a decreasing $S(EO)$ and a strong increase in $X(O_2)$. In comparison, the performance of the Ag5/SiO_2-N_2 catalyst converges to the blue S–X line, which parallels to the one for catalyst Ag15/α-Al_2O_3. Calculating the formation rates of EO per mass catalyst (Figure S52 and Figure S54) the Ag5/SiO_2-N_2 catalyst is thereby even more active than the conventional reference (45 vs. 35 µmol·g_{cat}^{-1}·min^{-1} at 190 °C or per mass Ag about four times more active). However, as indicated by Figure S53, at elevated temperatures above 200 °C the Ag5/SiO_2-N_2 catalyst starts to loose activity. Hereby, the $S(EO)$ values are constant while the $X(O_2)$ decreases.

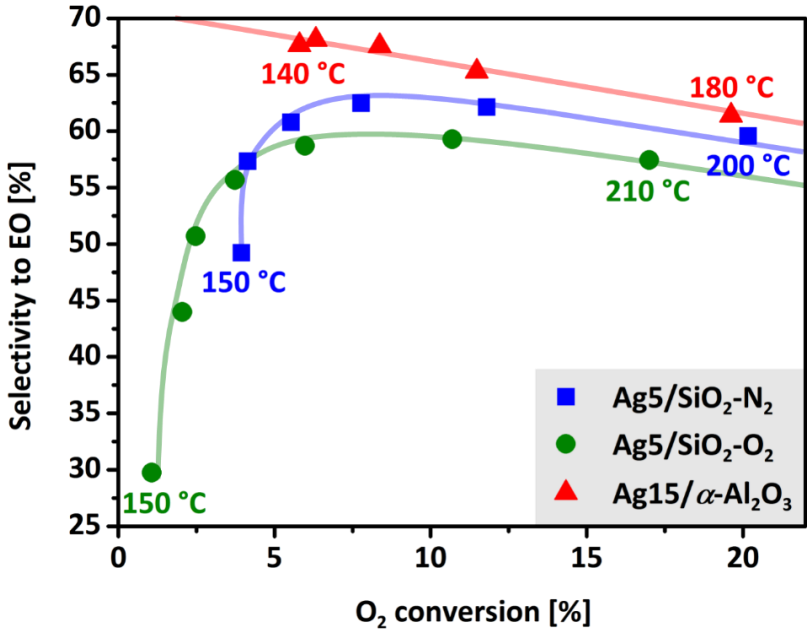

Figure 43. Selectivity to ethylene epoxide as function oxygen conversion for catalyst Ag15/α-Al_2O_3 (red triangle), Ag5/SiO_2-N_2 (blue squares) and Ag5/SiO_2-O_2 (green circles). Lines are a help to guide the eye.

Since the deactivation of the Ag5/SiO_2-N_2 catalyst starts at 200 °C, the same catalyst was tested again until 230 °C to trigger deactivation, and 180 °C to avoid deactivation. Figure S55 illustrates the corresponding PS distribution from STEM analysis. The spent Ag5/SiO_2-N_2 catalyst tested until 180 °C still exhibits the main PS at around 2 nm and 91 % of the particles are below 6 nm. Some of the Ag nanoparticles sintered, which is in line with the low Tammann temperature of less than 100 °C for unsupported 2 nm Ag nanoparticles.[28] This interpretation fits perfectly to the histogram of the spent Ag5/SiO_2-N_2 catalyst tested until 230 °C (Figure S55C). A broad PS distribution with a main PS at around 5 nm is observed. Such changes in the PS (from Figure S55A to C) are textbook examples of sintered particles starting to continuously grow in size. The PS analysis convincingly supports the discussed performance data of the Ag5/SiO_2-N_2 catalyst in Figure 43, which indeed shows the activity of Ag nanoparticles, highly active and selective for the epoxidation of ethylene.

Since we could demonstrate in chapter 2 that smaller Ag particles exhibit a stronger oxygen interaction, we tentatively interpret the activation phase of the Ag5/SiO_2-N_2 catalyst as also influenced by its Ag–O chemistry. To gain further experimental evidence, the Ag5/SiO_2 catalyst is pre-treated in synthetic air (Ag5/SiO_2-O_2, Figure 43, green) before testing. Upon the direct comparison to catalyst Ag5/SiO_2-N_2, the Ag5/SiO_2-O_2 catalyst shows at low temperatures a poor S(EO) and $X(O_2)$ discussed above as activation phase, however, this period is more pronounced and prolonged. The maximum S(EO) of 58 % in the activated state is reached at 190 °C and generally the Ag5/SiO_2-O_2 catalyst is less active (i.e. at 200 °C same S(EO) but only 50 % of the conversion). Finally, upon increasing the temperature, also the Ag5/SiO_2-O_2 catalyst reaches a typical S–X behavior (green line).

The evolution of the EO and CO_2 formation rates under isothermal conditions provides additional information about the ongoing processes (Figure S52 and Figure S53). As a function of time at a given temperature the CO_2 rates decrease continuously. Since the EO rates are slightly increased, an increase in S(EO) is yielded. This effect weakens upon increasing the temperature and is influenced by the pre-treatment. The Ag5/SiO_2-O_2 shows a more pronounced activation, also extended to higher temperatures. It seems that due to the pre-treatment in O_2 containing atmosphere, reaction sites, in particular those responsible for the EO formation, are blocked.

Besides, the Ag5/SiO_2-O_2 catalyst shows a significant shift of the sintering induced deactivation to higher temperatures compared to Ag5/SiO_2-N_2, which can be described as oxygen induced stabilization of the nanoparticles. In turn, this implies that residual oxygen in/on Ag might be responsible for the observed effects. This is supported by studies which show that the pre-treatment also pre-determines the existence of highly stable oxygen species in/on the Ag nanoparticles difficult to allocate for oxidation reactions.[14, 15, 29] It is hypothesized that an increased oxidic character of the oxygen in/on Ag, describable as possible surface passivation, is responsible for the inactivity in oxidation reactions as e.g. illustrated in Figure 40. The existence of highly temperature stable oxygen species for Ag nanoparticles below 6 nm (see chapter 2) might also influence the catalytic performance.

3.4.3 Impact of the oxygen concentration in/on Ag

For a better understanding on the effect of the oxygen concentration in/on Ag, oxygen thermal desorption spectroscopy (O_2-TDS) was applied. The calcined catalysts were *in-situ* pre-treated under Ar (Ag5/SiO_2-Ar, analogue to Ag5/SiO_2-N_2) or synthetic air. The corresponding desorption spectra are shown in Figure 44. Two regions in which oxygen desorbs can be clearly distinguished, with region I (200 °C – 500 °C) having a maximum at 350 °C and region II for T > 540 °C. The Ar pre-treatment strongly reduces the amount of desorbed O_2 in region I to 54 %. Region II stays almost unaffected, emphasized by the converging amount of

desorbed oxygen at around 620 °C. These different oxygen desorption signals also indicate a correlation between the different activation behaviors upon the different treatments of Ag5/SiO_2-N_2 and Ag5/SiO_2-O_2. The species desorbed in region I, more popular in Ag5/SiO_2-O_2, likely reacts with ethylene and contributes to the unselective full oxidation reaction to CO_2 (increased CO_2 formation rates Figure S52 and Figure S53). Further, this might be the origin of a possible blocking of the reaction sites and explain the lowered $X(O_2)$. The oxygen species attributed to region II might either be located deeper subsurface or on defect sites[30] and are not affected by the pre-treatments. The combination of TDS and catalytic data additionally leads to the hypothesis that for ethylene epoxidation low oxygen concentrations in/on Ag are beneficial in terms of selectivity and conversion.

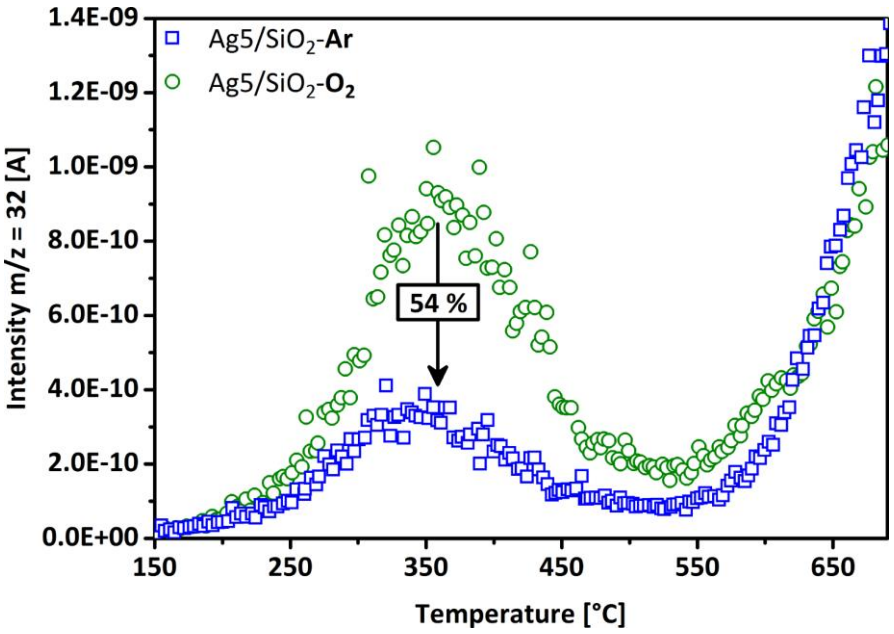

Figure 44. O_2-TDS for Ag5/SiO_2 pre-treated in pure Ar (blue) and synthetic air (green).

To gain further insights into the nature of oxygen species, isotope exchange experiments with $^{18}O_2$ inside the TDS setup were conducted. After pre-treating the Ag5/SiO_2 catalyst for 12 h at 210 °C in synthetic air, the exposure times of $^{18}O_2$ was adjusted to 0 min, 10 min and 60 min at 200 °C. Figure 45A shows the desorption signal of m/z = 34, which represents the mixed labeled oxygen ($^{16}O^{18}O$). As a function of time, the mixed labeled oxygen increases in region I and II with no change of m/z = 36 (see also Figure S56). This implies that the oxygen is dissociatively activated as atomic oxygen in/on Ag. The absence of the double labeled oxygen ($^{18}O^{18}O$) and the ongoing increase of the m/z = 34 signal with the exposure time in region II, indicates a migration of the atomic ^{18}O species from the surface to the subsurface region.

To further clarify the location of the atomic oxygen species, a second experiment with $C^{18}O_2$ was conducted. To avoid any carbonate formation on the surface by contact to the environment, the precursor sample $AgNO_3/SiO_2$ was *in-situ* calcined in synthetic air. The *in-situ* generated Ag5/SiO_2-O_2 catalyst was

subsequently exposed to $C^{18}O_2$ at 40 °C to create a labeled surface Ag_2CO_3. Since oxygen is able to migrate into the subsurface region of Ag, the surface limited carbonate formation is used to discriminate between terminally bound oxygen on the Ag surface and bridging/subsurface oxygen. The resulting carbonate is consequently partially labeled "$Ag_2C^{18}O_2{}^{16}O$". Temperature induced decomposition of the surface carbonates results in the release of CO_2, which is either mono- ($C^{18}O^{16}O$, m/z = 46) or double-labeled ($C^{18}O_2$, m/z = 48). The labeled character of the CO_2 contains information about the nature of interaction of the atomic ^{16}O stored in or on the Ag particle as illustrated in Figure 46. In the case of terminally bound oxygen on the Ag surface, the same probability of 50 % for the desorption of $C^{18}O^{16}O$ or $C^{18}O_2$ is expected due to an equivalent binding strength of oxygen to Ag. The corresponding desorption events are shown in Figure 45B. The dominant desorption species is identified as $C^{18}O_2$ (m/z = 48) with a significantly smaller desorption event for $C^{18}O^{16}O$ (m/z = 46). Besides, the desorption temperature is exceptionally low with desorption maxima at around 50 °C, as clear indication for surface carbonates. This leads to the conclusion that the present atomic oxygen species are dominantly (around 2/3) bridging and/or located subsurface. With other words, the surface is already poor in atomic oxygen, even after calcination and saturation with oxygen in synthetic air.

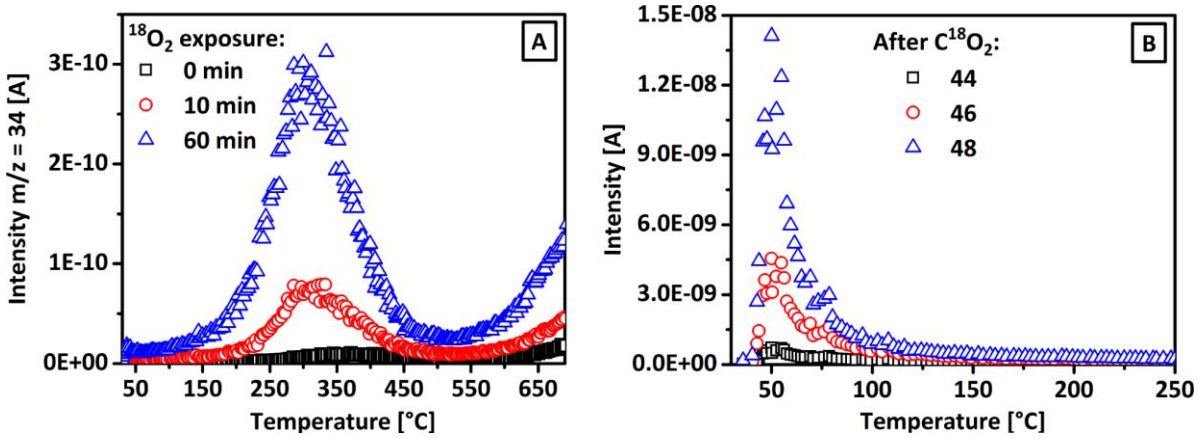

Figure 45. TDS analysis of partially labeled $^{18}O^{16}O$ (m/z = 34) desorbed from catalyst Ag5/SiO_2 after pre-treated in synthetic air without (black squares), with 10 min (red circles) and 60 min (blue triangles) exposure to $^{18}O_2$ (A). Sample $AgNO_3/SiO_2$ was *in-situ* calcination in synthetic air and subsequent exposed to labeled $C^{18}O_2$. The resulting desorption events for m/z = 44 (black squares), 46 (red circles) and 48 (blue triangles) are shown in (B).

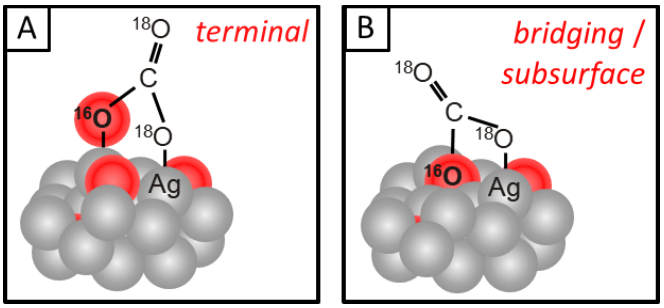

Figure 46. Scheme of possible surface Ag_2CO_3 formation on Ag nanoparticles *via* terminal (A) or bridging/subsurface oxygen (B).

The influence of oxygen on the catalytic performance is further evaluated by TDS experiments simulating the activation period. The *in-situ* created Ag5/SiO_2-O_2 catalyst was tested at 1 bar and reaction gas feed (C_2H_4:O_2 = 5:1) for 4 h at 230 °C in the TDS setup (Figure S57A). After reaching a steady-state conversion, the resulting O_2-TDS spectrum was recorded (Figure S58). A significantly reduced amount of oxygen desorbed from the catalyst is observed (green and yellow curves Figure 47). Additionally, the peak maximum for region I is shifted to 440 °C and the onset of region II to 610 °C. This shift to higher temperatures shows that for both regions the weaker bound oxygen species are efficiently removed while the stronger bound oxygen species partly remain during the ethylene epoxidation. In addition, a completely activated Ag5/SiO_2 catalyst tested under 17.5 bar was transferred to the TDS setup and an oxygen desorption experiment was conducted. The corresponding O_2 desorption signal is negligible (Figure 47, red curve identical to the baseline) and confirms the discussed findings above: The activation phase of the Ag5/SiO_2 catalyst is accompanied by the consumption of unselective oxygen species leading to a selective catalyst with a low oxygen concentration probably in the subsurface region.

To confirm the working hypothesis of an oxygen rich and comparably unselective Ag catalyst, an increasing/decreasing/increasing temperature testing recipe was intended to lead to different catalytic performances in terms of $X(O_2)$ and $S(EO)$. Figure S59 shows the applied temperature program to the Ag5/SiO_2-N_2 catalyst, the corresponding formation rates of EO/CO_2 and the $S(EO)$. Within the first increasing branch of the temperature, the development of the $S(EO)$ is impressively visualized starting at 150 °C with around 20 % and finally reaching 58 %. The second increasing branch (ca. 25 to 35 h TOS) shows only minor changes in terms of $S(EO)$ (58 to 62 %) as a function of the temperature, but significantly higher EO than CO_2 formation rates. Since 170 °C was three times selected as reaction temperature, Figure 48 highlights the changes as a function of time upon cycling. The continuously decreasing CO_2 formation rates, being accompanied by increasing EO formation rates and increase in $S(EO)$, serve exactly as the experimental evidence matching the above findings and working hypothesis.

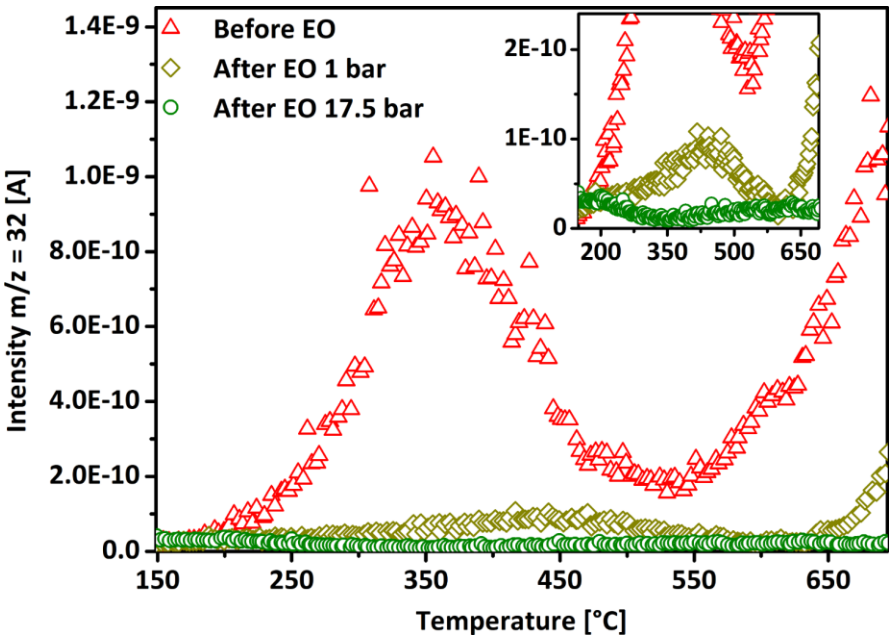

Figure 47. O_2-TDS for Ag5/SiO_2 pre-treated in synthetic air (red) and after subsequent ethylene epoxidation at 230 °C at 1 bar (yellow). Additionally, the desorption spectrum of catalyst Ag5/SiO_2-N_2 after reaching steady-state in ethylene epoxidation at 180 °C and 17.5 bar (Figure S59) is shown (green).

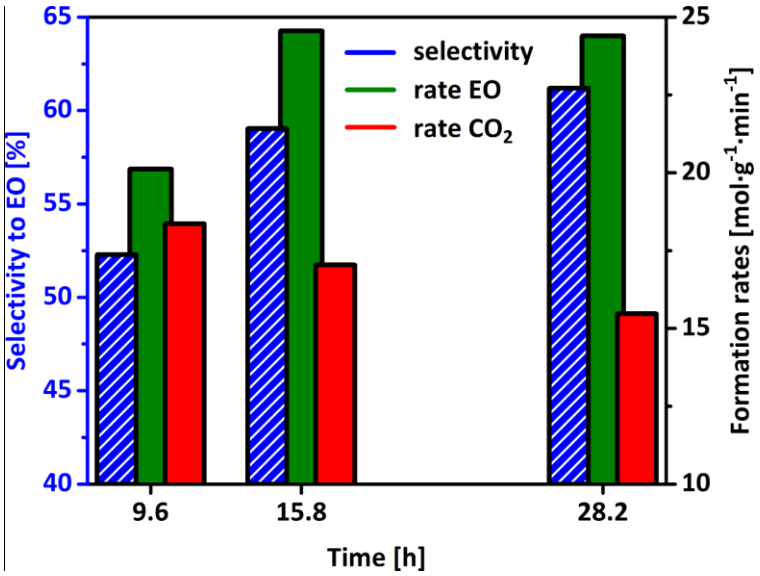

Figure 48. Extracted results from ethylene epoxidation at 17.5 bar using an increasing/decreasing/increasing temperature testing recipe using the range from 150 – 180 °C. Show are the selectivity to EO (blue) and formation rates of EO (green) and CO_2 (red) at three different testing stages with T = 170 °C (complete test is shown in Figure S59).

The oxygen poor state of Ag, responsible for high *S*(EO), is so far only confirmed for the Ag5/SiO_2 catalysts. To transfer the working concept to the conventional Ag15/α-Al_2O_3 reference, TDS investigations were performed. The oxygen desorption signals of the oxygen saturated state (12 h at 200 °C in synthetic air), with a subsequent *in-situ* ethylene epoxidation test for 4 h and an ethylene epoxidation test for 12 h without pre-treatment at 230 °C are shown in Figure S57. The desorption signal of the oxygen saturated Ag15/α-Al_2O_3 catalyst is illustrated in Figure S58 and reaches, as also shown in chapter 2, its maximum at comparably low

temperatures of 160 °C. A significantly decreased desorption event is observed upon catalysis for 4 h, which almost vanishes after the 12 h testing period. These results further evidence that the selective state of Ag independent of the Ag PS is oxygen poor. However, a small quantity of dissolved oxygen is needed in Ag ($Ag^{\delta+}O_x$) as shown in chapter 2, since Ag^0 metal with a closed *d*-band is not able to adsorb ethylene as well as to activate oxygen dissociatively as prerequisite for any catalytic activity.

Based on the shown catalytic investigation a kinetic analysis leads to the corresponding apparent activation energy (E_A). Figure 49 shows the Arrhenius plots of the $X(O_2)$. The corresponding E_A of EO and CO_2 formation are given in Figure S60 and Figure S61. Since the $Ag5/SiO_2$ catalysts are not completely in steady-state due to the progressing activation at low temperatures and sintering at high temperatures, the calculated E_A values are conservatively interpreted.

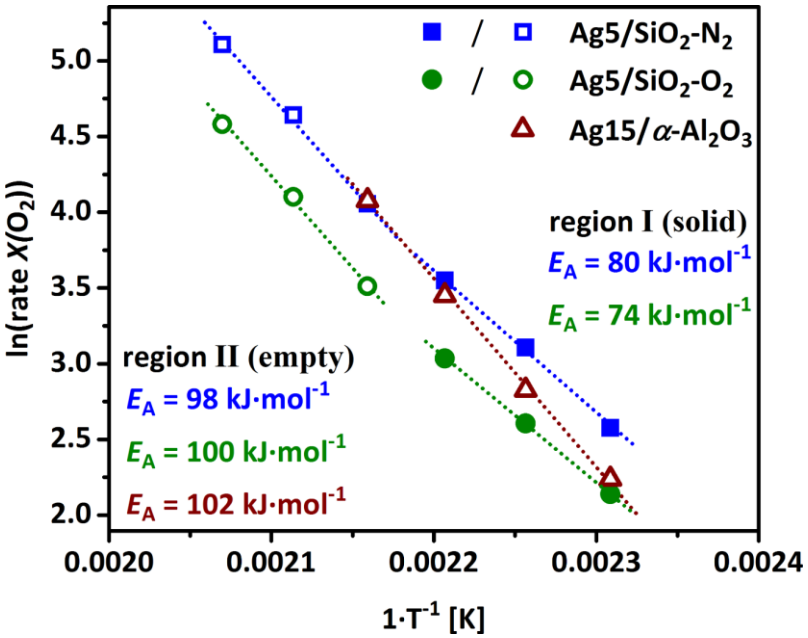

Figure 49. Arrhenius plot and resulting apparent activation energies (E_A) for oxygen conversions for catalysts $Ag5/SiO_2$-N_2, $Ag5/SiO_2$-O_2 and $Ag15/\alpha$-Al_2O_3. Calculated E_A are separated into different regions, whereby for $Ag5/SiO_2$ catalysts region I represents the low temperature conversions from 160 – 180 °C and region II from 190 – 210 °C. Fully equilibrated $Ag15/\alpha$-Al_2O_3 serves as reference for region II based on conversions corresponding to 160 – 190 °C. Error of the calculations are ±2 kJ·mol^{-1}.

For $Ag5/SiO_2$-N_2 and $Ag5/SiO_2$-O_2 two differing regimes are observed. Region I corresponds to the low temperature conversions in the range of 160 – 180 °C, still being in the activation phase. The corresponding E_A is calculated to 80 kJ·mol^{-1} for $Ag5/SiO_2$-N_2 and 74 kJ·mol^{-1} for $Ag5/SiO_2$-O_2, respectively. In Region II values from 190 – 210 °C are considered and the E_A are about 25 – 30 kJ·mol^{-1} higher compared to region I ($Ag5/SiO_2$-N_2 = 98 kJ·mol^{-1}, $Ag5/SiO_2$-O_2 = 100 kJ·mol^{-1}). It is assumed that catalysts $Ag5/SiO_2$-N_2 and $Ag5/SiO_2$-O_2 are (almost) completely activated since they achieved a linear $S - X$ region, and the E_A of around 100 kJ·mol^{-1} represents the final and oxygen poor state of the catalyst. It is also in line with the stable S(EO)

values at the end of the dwell at 210 °C. The equilibrated Ag15/α-Al_2O_3 reference systems shows only one regime in the Arrhenius plot with a corresponding E_A = 102 kJ·mol^{-1}. With respect to the deviations of ±2 kJ·mol^{-1}, the values for Ag15/α-Al_2O_3 and both Ag5/SiO_2 catalysts are in good agreement and the catalysts might be in a similar oxygen poor state. The reason for the low E_A values in region I for Ag5/SiO_2 catalysts is explained by the E_A of the EO and CO_2 formation (Figure S61). The E_A of the EO formation lies between 92±3 kJ·mol^{-1} and 98±3 kJ·mol^{-1} for Ag5/SiO_2 and Ag15/α-Al_2O_3 catalysts for the complete temperature range, meaning one region is observed. For catalyst Ag15/α-Al_2O_3, also the E_A of the CO_2 formation of 123±2 kJ·mol^{-1} is extracted from one linear fit. For the Ag5/SiO_2 catalysts the E_A of the CO_2 formation is divided into different regimes and two linear fits are needed. For region I (150 – 180 °C) an E_A of 62 – 72 kJ·mol^{-1} and for region II (180 – 210 °C) an E_A of around 100 kJ·mol^{-1} is calculated, which represent a significant increase. Since the low temperature region I is coupled to the activation period of the Ag5/SiO_2 catalysts, the low E_A values for CO_2 are related to the consumption of unselective oxygen species in/on Ag. As soon as the catalysts reach the selective, high temperature regime, the E_A for CO_2 is increased. This is supported by the E_A values of the Ag15/α-Al_2O_3 catalyst, which are in reasonable agreement with the values of the almost equilibrated Ag5/SiO_2 catalysts (see Figure 43).

3.4.4 Ethylene epoxide decomposition test

The differences in E_A for the $X(O_2)$ in region I, explained by different CO_2 formation rates, suggest that also different process might be involved. Besides the isomerization of ethylene epoxide to acetaldehyde and the following oxidation to CO_2, the complete oxidation to CO_2 might also be initiated without forming EO. To discriminate between Ag and the support on which these pathways might occur, an ethylene epoxide decomposition test was applied. By passing ethylene epoxide over the supports and the corresponding supported Ag catalysts, each contribution is validated. Figure 50 shows the results of the EO decomposition tests at 250 °C for Ag5/SiO_2, Ag15/α-Al_2O_3 and as reference materials SiO_2, α-Al_2O_3 and Ag powder (see also Table 6). All tested samples were pre-treated in synthetic air at 250 °C with a dwell of 10 min. Ag powder and Ag15/α-Al_2O_3 show EO conversion rates below 0.1 µmol·min^{-1}·g_{cat}^{-1} solely to acetaldehyde *via* isomerization. No full oxidation to CO_2 is detected. That means Ag powder and Ag particles with domain sizes larger than 40 nm seem to be a negligible source of isomerization, respectively CO_2 formation. The α-Al_2O_3 support converts about half of the Ag15/α-Al_2O_3 catalyst (0.046 µmol·min^{-1}·g_{cat}^{-1} vs. 0.084 µmol·min^{-1}·g_{cat}^{-1}), which confirms its chemically inert character as fundamental property of supports applied in the EO reaction. Significant EO conversions can be observed for Ag5/SiO_2 with selectivities of 90 % to CO_2 and 10 % to acetaldehyde. The fraction of 0.10 µmol·min^{-1}·g_{cat}^{-1} for the isomerization to acetaldehyde is thereby close to the amount detected for pure SiO_2 with 0.15 µmol·min^{-1}·g_{cat}^{-1}, evidencing that the isomerization also takes

place on SiO_2. Since the BET surface area of SiO_2 is 328 times higher, the EO isomerization per m^2 is around 100 times smaller compared to α-Al_2O_3, evidencing the general suitability of SiO_2 as support material. As a consequence, the Ag nanoparticles on SiO_2 are identified as major source of the CO_2 formation, from either EO or acetaldehyde combustion. To differentiate between the different kinds of Ag, the EO conversion rates normalized to their specific Ag surface area (SA_{Ag}, see chapter 2) have to be compared. Additionally, the support contributions of around 14 % for SiO_2 and around 46 % for α-Al_2O_3 is subtracted (Table 6). The specific EO conversion rates $X(EO)\cdot SA_{Ag}^{-1}$ show a distinct PS effect. From the Ag powder to Ag particles with around 40 nm and the Ag nanoparticles below 6 nm, the specific isomerization and/or combustion to CO_2 is incrementally increased. The Ag contribution of the Ag15/α-Al_2O_3 reference system is negligible since already absent before catalysis (Figure 43). We interpret the increased specific EO conversion rate of the Ag nanoparticles as related to the more stable oxygen species in/on Ag (see also Figure 44), since they are identified as being responsible for the pronounced activation period (Figure 43 and Figure 48). The low E_A during the activation period (up to about 70 $kJ\cdot mol^{-1}$) is very likely related to a CO_2 formation without EO isomerization. Consequently, the CO_2 formation and the high CO_2 E_A (about 120 $kJ\cdot mol^{-1}$) are related to the EO isomerization and combustion pathway.

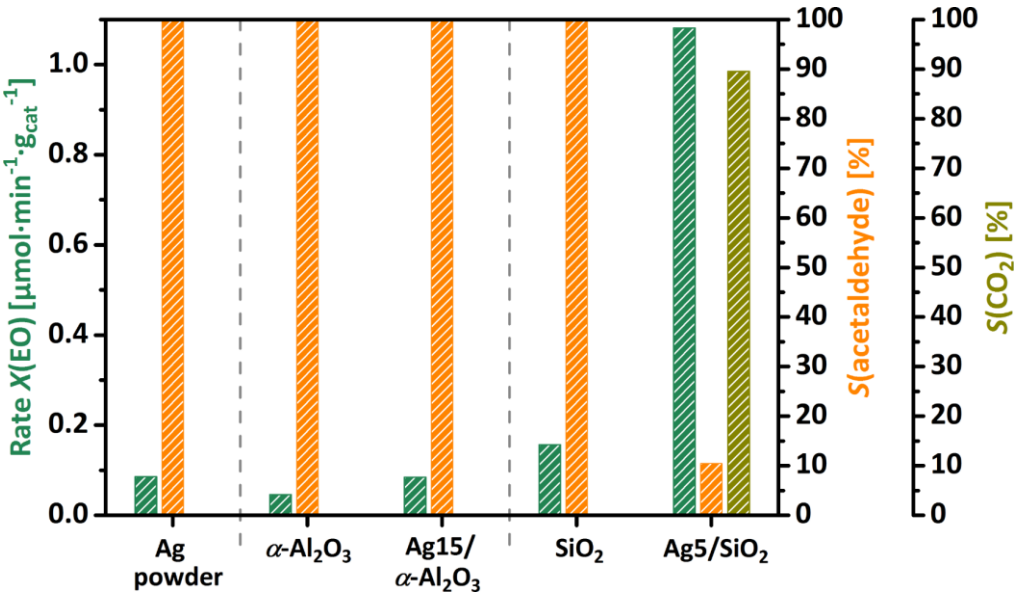

Figure 50. EO decomposition test with decomposition/isomerization rates per gram catalysts/support with corresponding selectivities to acetaldehyde and CO_2 for Ag powder, Ag15/α-Al_2O_3 and Ag5/SiO_2 catalysts with the corresponding supports α-Al_2O_3 and SiO_2.

Table 6. Overview of EO conversions and normalized EO conversions per surface area Ag (SA_{Ag}) of each catalyst determined by BET for Ag powder and C_2H_4 adsorption (see chapter 2) for supported catalysts. EO conversions are in addition corrected concerning the EO conversion fraction derived from the pure support ("support corrected")

	Ag powder	Ag15/α-Al_2O_3	Ag5/SiO_2
$X(EO)$ [$\mu mol \cdot min^{-1} \cdot g_{cat}^{-1}$]	0.086	0.084	1.08
$X(EO)_{support\ corrected}$ [$\mu mol \cdot min^{-1} \cdot g_{cat}^{-1}$]	0.086	0.038	0.924
SA_{Ag} [$m^2 \cdot g^{-1}$]	0.465	0.170	2.42
$X(EO) \cdot SA_{Ag}^{-1}$ [$\mu mol \cdot min^{-1} \cdot m^{-2}$]	0.185	0.224	0.382

3.5 Conclusion

Based on the advanced synthesis of supported Ag nanoparticles below 6 nm with a narrow size distribution (Ag5/SiO_2 model catalysts, chapter 2), we demonstrated its activity and selectivity in the ethylene epoxidation under industrially relevant conditions. Besides, the high strength of the Ag–O interaction allowed a resolution of the activation period, to finally extract the selective state of Ag. The concept of an oxygen poor and selective state of Ag was independent of the particle size and transferable to a Ag15/α-Al_2O_3 reference system, investigated accordingly.

The present findings correlate well with a suite of spectroscopic studies aiming at finding the oxygen species for selective oxidation. The standard discrimination in nucleophilic (combustion) and electrophilic[31] (selective) oxygen is oversimplified. The atomic oxygen, as shown by isotope exchange experiments, can easily submerge into the subsurface regime[32] and modify its electronic structure. The unreconstructed surface/subsurface oxygen is rarely abundant[33] and thus selective. This in full agreement with our present findings on Ag supported "real-world" catalysts and identifies one important descriptor for a selective catalyst as a minimization of atomic oxygen on the surface. Further, a small fraction of oxygen is enough to modify Ag electronically, meaning open the *d*-band as e.g. $Ag^{\delta+}O_x$. This $Ag^{\delta+}O_x$ state enables the activation of ethylene and oxygen resulting in an active and selective catalyst for the ethylene epoxidation reaction.

In general, the concept of highly dispersed nanoparticles creating more active sites is, particularly for Ag, not without pitfalls. The design challenge remains in the transformation of reactive sites into selective ones. The present case illustrates how the reaction of nanostructures with unexpected stability parameters, not predictable by any standard phase diagram, may possibly override the positive effect of higher dispersion. The intriguing Ag–O chemistry in combination with a PS dependent activation led to the controversially discussed role of Ag nanoparticles and a possible PS effect, which has now been understood and clarified.

3.6 References

[1] R. Schlögl, *Angew. Chem. Int. Ed.* **2015**, *54*, 3465-3520; *Angew. Chem.* **2015**, 127, 3531-3589.

[2] R. Schlögl, S. B. Abd Hamid, *Angew. Chem. Int. Ed.* **2004**, *43*, 1628-1637; *Angew. Chem.* **2004**, *116*, 1656-1667

[3] J. R. Anderson, *Science Progress (1933-)* **1985**, *69*, 461-484.

[4] J. P. den Breejen, P. B. Radstake, G. L. Bezemer, J. H. Bitter, V. Frøseth, A. Holmen, K. P. d. Jong, *J. Am. Chem. Soc.* **2009**, *131*, 7197-7203.

[5] A. Ueno, H. Suzuki, Y. Kotera, *J. Chem. Soc., Faraday Trans.* **1983**, *79*, 127-136.

[6] J. Hoffmann, I. Meusel, J. Hartmann, J. Libuda, H. J. Freund, *J. Catal.* **2001**, *204*, 378-392.

[7] N. I. Jaeger, A. L. Jourdan, G. Schulz-Ekloff, *J. Chem. Soc., Faraday Trans.* **1991**, *87*, 1251-1257.

[8] I. Kasatkin, P. Kurr, B. Kniep, A. Trunschke, R. Schlögl, *Angew. Chem. Int. Ed.* **2007**, *46*, 7324-7327.

[9] Y. Lei, F. Mehmood, S. Lee, J. Greeley, B. Lee, S. Seifert, R. E. Winans, J. W. Elam, R. J. Meyer, P. C. Redfern, D. Teschner, R. Schlögl, M. J. Pellin, L. A. Curtiss, S. Vajda, *Science* **2010**, *328*, 224-228.

[10] J. T. Miller, A. J. Kropf, Y. Zha, J. R. Regalbuto, L. Delannoy, C. Louis, E. Bus, J. A. van Bokhoven, *J. Catal.* **2006**, *240*, 222-234.

[11] J. E. van den Reijen, S. Kanungo, T. A. J. Welling, M. Versluijs-Helder, T. A. Nijhuis, K. P. de Jong, P. E. de Jongh, *J. Catal.* **2017**, *356*, 65-74.

[12] J. C. Wu, P. Harriott, *J. Catal.* **1975**, *39*, 395-402.

[13] X. E. Verykios, F. P. Stein, R. W. Coughlin, *J. Catal.* **1980**, *66*, 368-382.

[14] S. Cheng, A. Clearfield, *J. Catal.* **1985**, *94*, 455-467.

[15] J. K. Lee, X. E. Verykios, R. Pitchai, *Appl. Catal.* **1989**, *50*, 171-188.

[16] S. N. Goncharova, E. A. Paukshtis, B. S. Bal'zhinimaev, *Appl. Catal. A* **1995**, *126*, 67-84.

[17] D. V. Demidov, I. P. Prosvirin, A. M. Sorokin, T. Rocha, A. Knop-Gericke, V. I. Bukhtiyarov, *Kinet. Catal.* **2011**, *52*, 855-861.

[18] A. P. Fotopoulos, K. S. Triantafyllidis, *Catal. Today* **2007**, *127*, 148-156.

[19] M. Boudart, *Adv. Catal.* **1969**, *20*, 153.

[20] R. van Hardeveld, F. Hartog, *Adv. Catal.* **1972**, *22*, 75-113.

[21] C. T. Campbell, J. R. V. Sellers, *Faraday Discuss.* **2013**, *162*, 9-30.

[22] C. T. Campbell, Z. Mao, *ACS Catal.* **2017**, *7*, 8460-8466.

[23] T. Rosendahl, T. Mäurer, C. K. Dobner, A. Lehr, J. Wanka; WO 20130/61294 A1, **2013**, BASF SE, Ludwigshafen (GER)

[24] A. Coelho, *TOPAS: General Profile and Structure Analysis Software for Powder Diffraction Data; Bruker AXS GmbH: Karlsruhe, Germany* **2014**, *version 5*.

[25] E. R. Jette, F. Foote, *J. Chem. Phys.* **1935**, *3*, 605-616.

[26] N. Koga, S. Yamada, T. Kimura, *J. Phys. Chem. C* **2013**, *117*, 326-336.

[27] W. M. Haynes, *CRC Handbook of Chemistry and Physics, 96th Edition*, CRC Press, **2015**.

[28] W. Luo, W. Hu, S. Xiao, *J. Phys. Chem. C* **2008**, *112*, 2359-2369.

[29] R. W. Clayton, S. V. Norval, in *Catalysis: Volume 3, Vol. 3* (Eds.: C. Kemball, D. A. Dowden), The Royal Society of Chemistry, **1980**, pp. 70-97.

[30] W. W. Smeltzer, E. L. Tollefson, A. Cambron, *Can. J. Chem.* **1956**, *34*, 1046-1060.

[31] T. C. R. Rocha, A. Oestereich, D. V. Demidov, M. Hävecker, S. Zafeiratos, G. Weinberg, V. I. Bukhtiyarov, A. Knop-Gericke, R. Schlögl, *Phys. Chem. Chem. Phys.* **2012**, *14*, 4554-4564.

[32] T. E. Jones, T. C. R. Rocha, A. Knop-Gericke, C. Stampfl, R. Schlögl, S. Piccinin, *Phys. Chem. Chem. Phys.* **2014**, *16*, 9002-9014.

[33] E. A. Carbonio, T. C. R. Rocha, A. Y. Klyushin, I. Píš, E. Magnano, S. Nappini, S. Piccinin, A. Knop-Gericke, R. Schlögl, T. E. Jones, *Chem. Sci.* **2018**, *9*, 990-998.

3.7 Supporting information

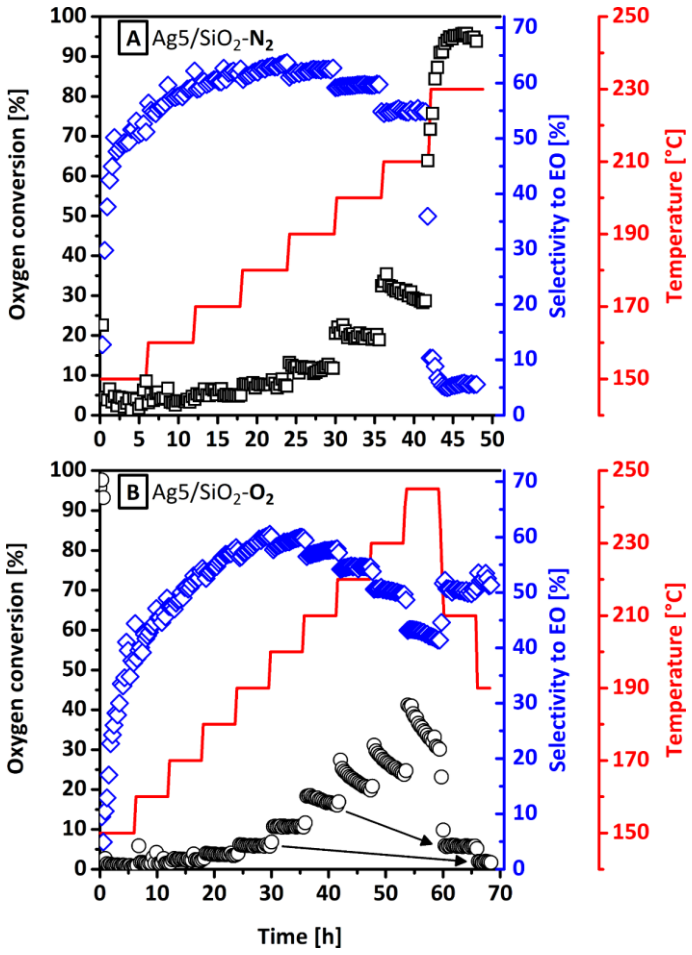

Figure S51. Ethylene epoxidation test of catalyst Ag5/SiO_2 after pre-treated in pure nitrogen (A, Ag5/SiO_2-N_2) or synthetic air (B, Ag5/SiO_2-O_2).

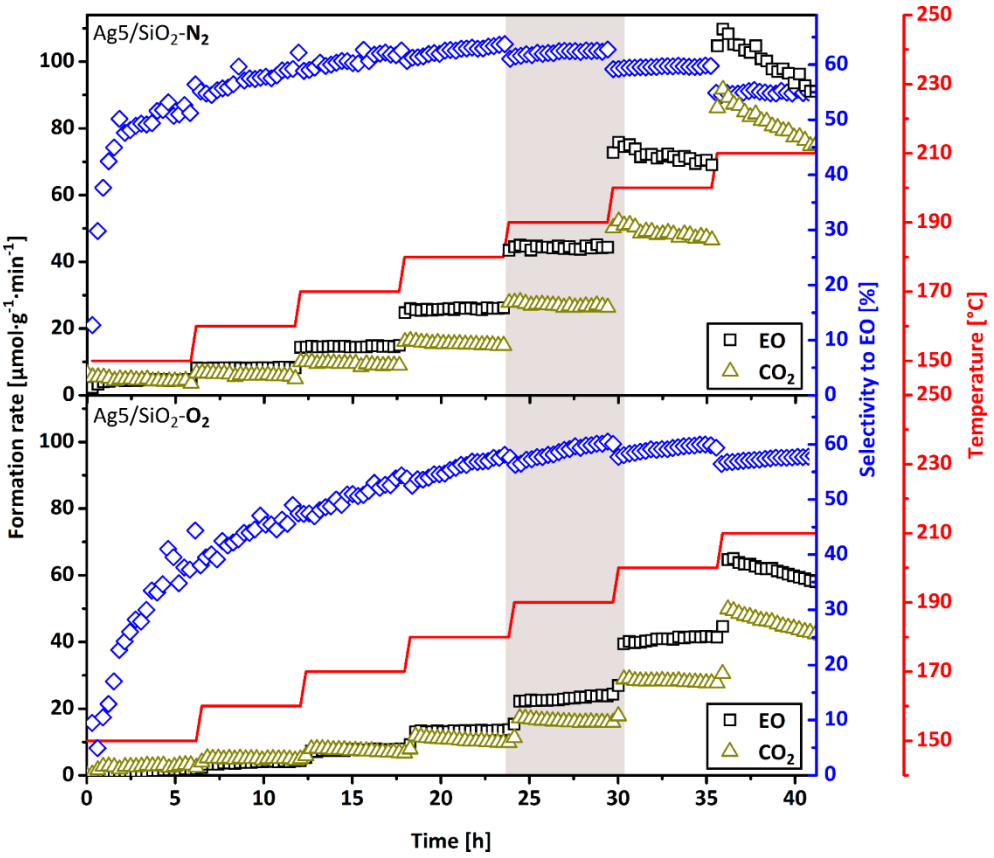

Figure S52. Complete ethylene epoxidation test for catalysts Ag5/SiO_2-N_2 (after N_2 pre-treatment) and Ag5/SiO_2-O_2 (after pre-treatment in synthetic air).

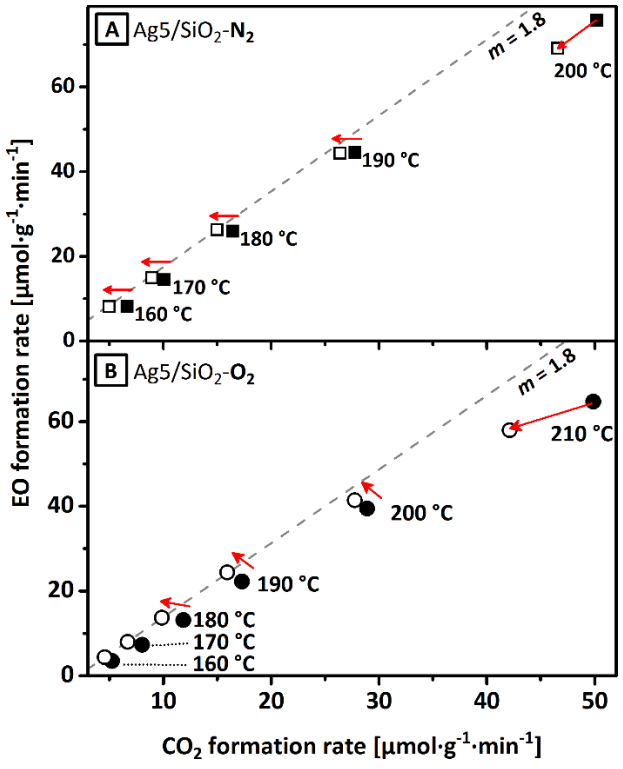

Figure S53. EO formation rate as a function of CO_2 formation rate for catalyst Ag5/SiO_2 after pre-treatment in pure nitrogen (A, Ag5/SiO_2-N_2) and synthetic air (B, Ag5/SiO_2-O_2). Filled symbols represent the starting point of isothermal dwell, empty points represent the end points after 6 h dwell time. Red arrows indicate the evolution during dwell time.

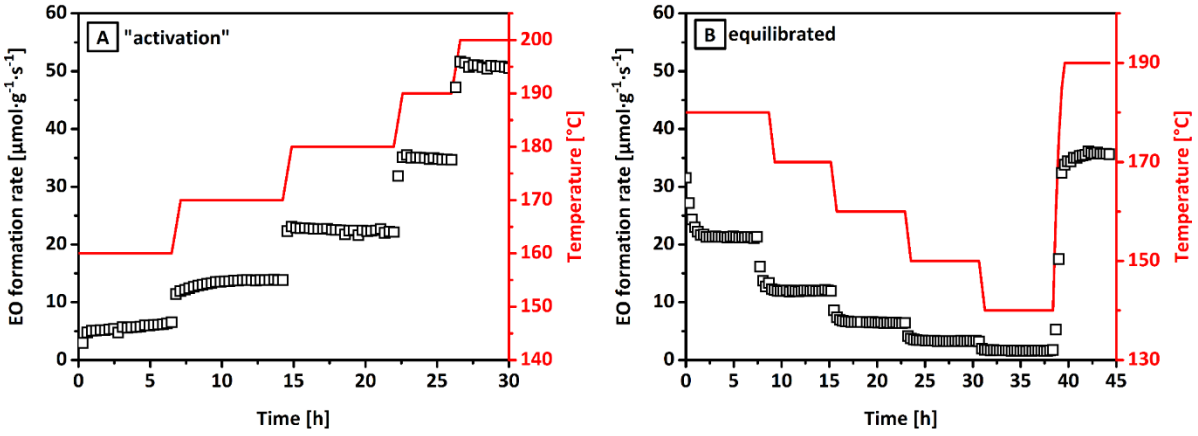

Figure S54. Ethylene epoxidation test of catalyst Ag15/α-Al_2O_3 after pre-treatment in nitrogen. The catalyst is activated in reaction feed (A) and subsequently tested at the equilibrated state (B).

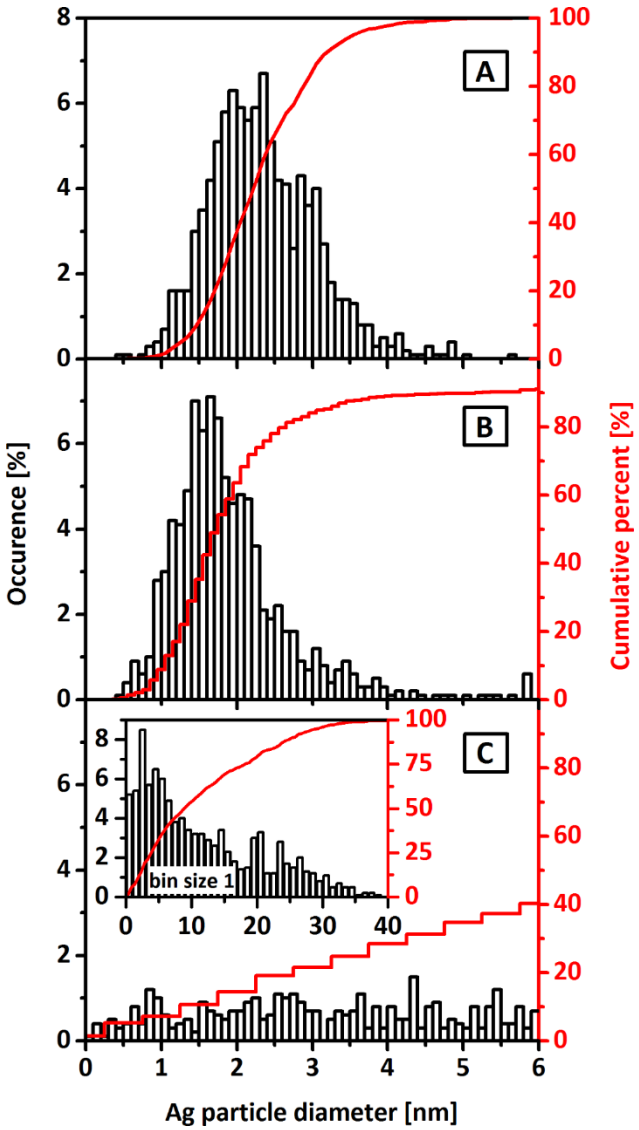

Figure S55. Ag particle size distribution from STEM with 0.1 nm bin size for a fresh Ag5/SiO_2 catalyst (A, identical to Figure 42D), catalyst Ag5/SiO_2-N_2 (pre-treated in N_2) after ethylene epoxidation after 180 °C (B) and 230 °C (C) with an inset showing the complete particle size distribution with a bin size of 1.0 nm.

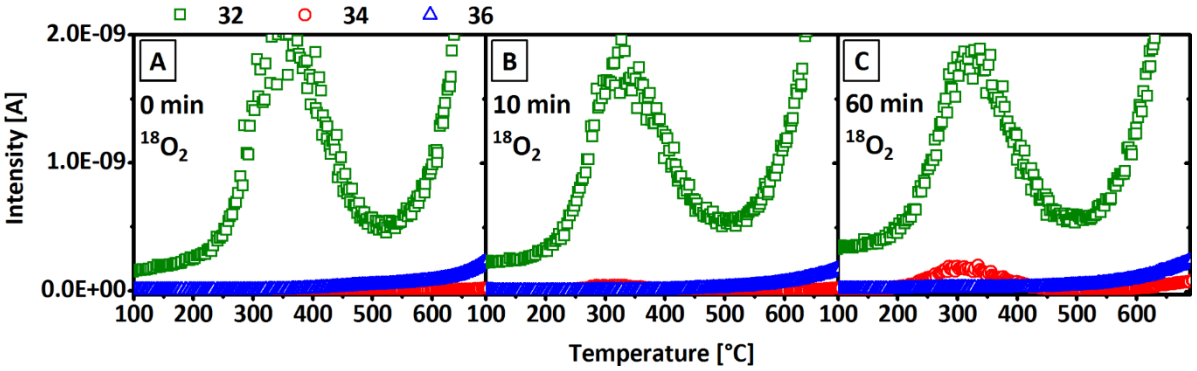

Figure S56. O_2-TDS of catalyst Ag/SiO_2 after a pre-treatment in synthetic air at 200 °C for 12 h without (A) and including 10 min (B) and 60 min (C) exposure to $^{18}O_2$. Shown are m/z = 32 (green), 34 (red) and 36 (blue).

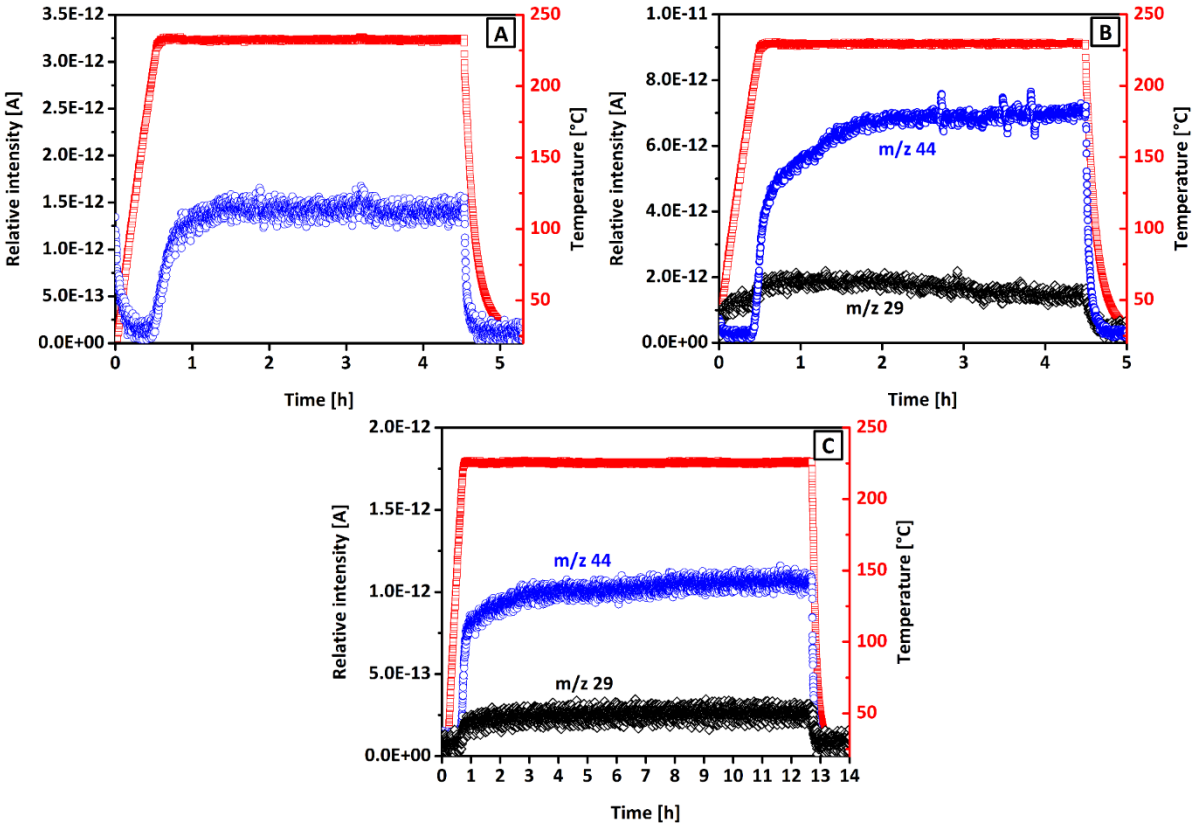

Figure S57. Ethylene epoxidation at ambient pressure at 230 °C. Sample $Ag5/SiO_2$ (A) was dwelled for 4 h and the corresponding m/z = 44 (blue) is shown. Sample $Ag15/\alpha\text{-}Al_2O_3$ (B), also dwelled for 4 h, is shown with m/z = 44 (blue) and 29 (black). Both catalysts were pre-treated in synthetic air for 12 h. Additionally, sample $Ag15/\alpha\text{-}Al_2O_3$ was tested for 12 h without pre-treatment (C). (Relative intensities are not comparable)

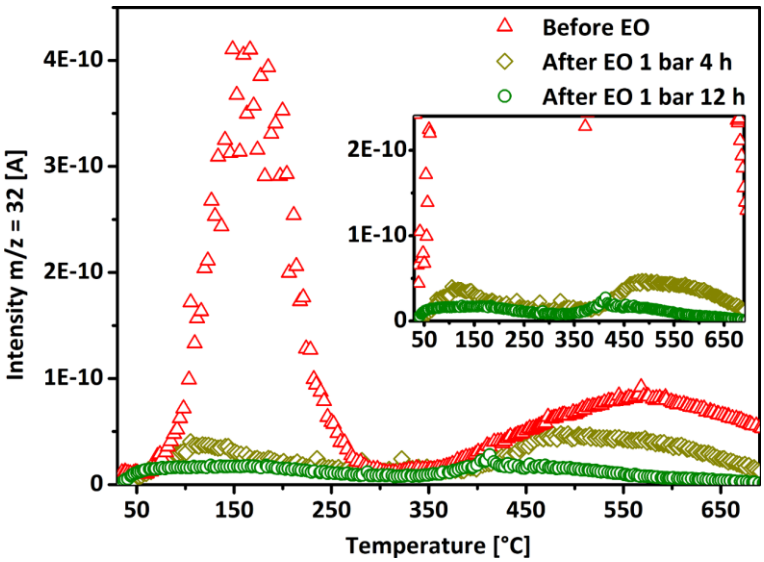

Figure S58. O_2-TDS for catalyst Ag15/α-Al_2O_3 pre-treated in synthetic air (red) and after subsequent ethylene epoxidation at 230 °C at 1 bar for 4 h (yellow) and 12 h (green).

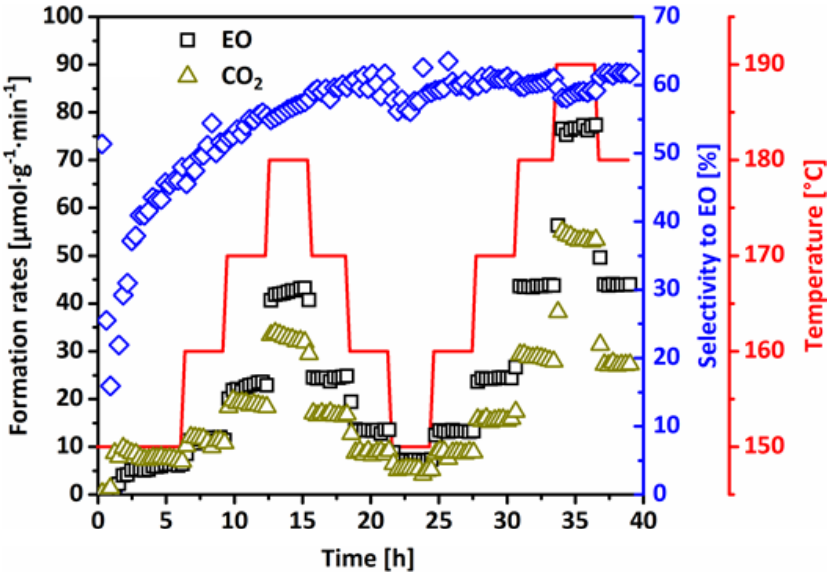

Figure S59. Ethylene epoxidation test of catalyst Ag5/SiO_2-N_2 at 17.5 bar using an increasing/decreasing/increasing temperature testing recipe. Show are the selectivity to EO (blue) and formation rates of EO (black) and CO_2 (yellow).

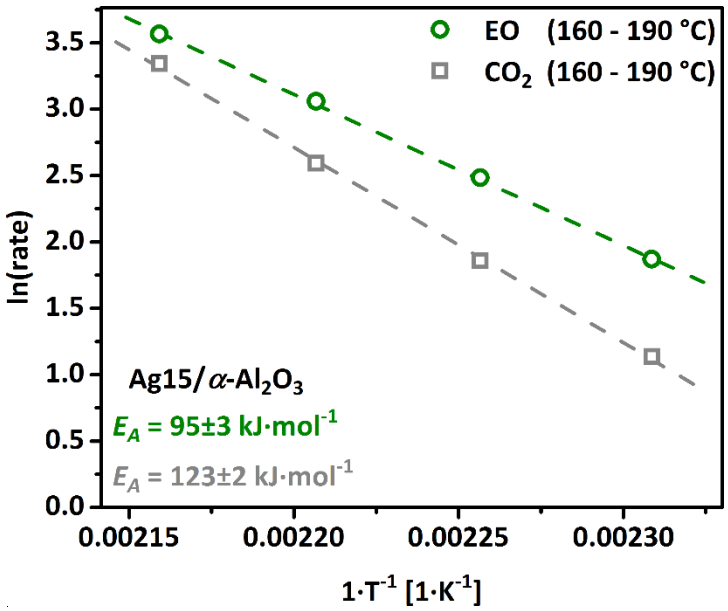

Figure S60. Apparent activation energy E_A for EO and CO_2 formation during ethylene epoxidation for equilibrated catalyst Ag15/α-Al_2O_3.

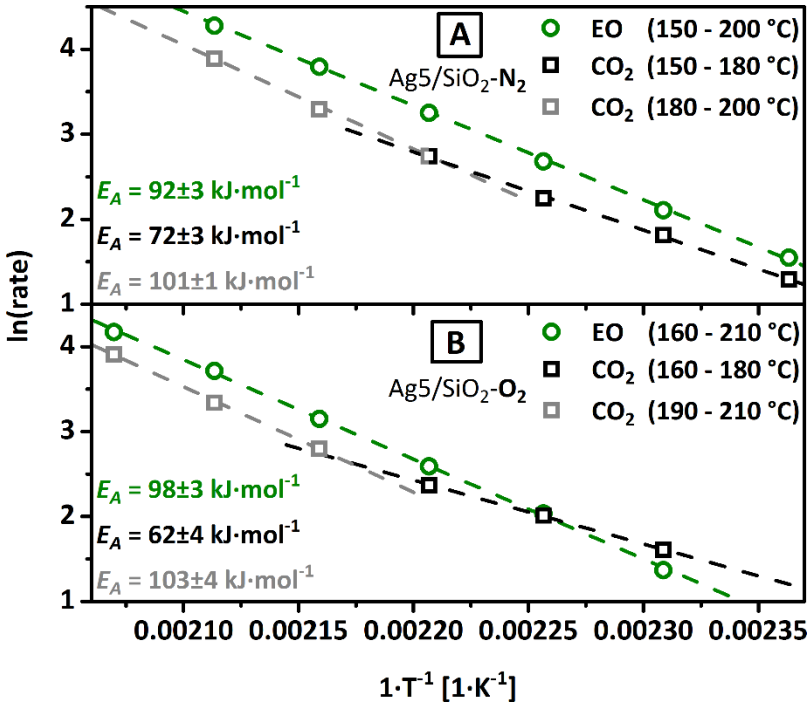

Figure S61. Apparent activation energy E_A for EO and CO_2 formation during ethylene epoxidation for catalyst Ag5/SiO_2 pre-treated in nitrogen (Ag5/SiO_2-N_2, A) and synthetic air (Ag5/SiO_2-O_2, B).

By comparing all three catalysts, E_A for regime I is increasing by Ag5/SiO_2-O_2 < Ag5/SiO_2-N_2 < Ag15/α-Al_2O_3 following the inverse trend as observed for the activation period time. This means that lower E_A for CO_2 results in lower S(EO). Thereby, three different E_A for CO_2 were calculated, which are 60 – 70 kJ·mol^{-1}, ~100 kJ·mol^{-1} and ~130 kJ·mol^{-1}, indicating differing CO_2 formation mechanism.

4 Systematic study on the SBA-15 synthesis: Impact of hydrothermal aging and fluoride addition on the structural integrity

4.1 Abstract

We describe a systematic variation of the SBA-15 synthesis conditions and its impact on the structural and chemical characteristics. An iterative alteration of the hydrothermal aging temperature and time led already to a significant change of the surface properties. Any effects on the total surface area and micropore contributions are amplified by a combined incremental increase of the NH_4F concentration. Based on changes of the unit cell parameters and an analysis of the BET surface area, microporosity and pore size distributions, the structural integrity is investigated. Our systematic approach enables the identification of coherencies between the evolution of physical SBA-15 properties. The obtained correlations of the surface and structural characteristics allow to discriminate between highly ordered SBA-15 up to disordered silica structures. The fluoride induced disintegration of the silica structure under hydrothermal conditions was also verified by TEM. A direct influence of the structural properties on the chemical properties of the surface was extracted by isopropanol oxidation, a probe reaction for acid and redox active surface sites. As a consequence of the combined results by complementary techniques, a lower limit for surface area and related properties of SBA-15 is identified as descriptor, critical for its structural integrity.

4.2 Introduction

Mesoporous materials, especially mesoporous silica, are of great interest in a wide field of applications. They are applied as catalysts, support materials, sorption media and sensor frameworks due to their large internal surface areas.[1, 2] Additionally, they exhibit a large structural diversity, leading to materials like MCM-41[3] consisting of unidirectional hexagonal pores arranged in a honeycomb structure, HMS[4] consisting of a wormhole framework structure or KIT-1[5] offering a branched mesoporous channel network. The common synthesis strategy for such mesoporous silica is based on a crystal templating approach, which strongly depends on the type and length of the surfactant, the alkaline character of the medium, the synthesis temperature and time. Thereby, physical properties like the pore size or pore wall thickness are manipulated. Such variations led to the synthesis of SBA-15[6], which exhibits a similar hexagonal mesoporous structure as MCM-41, but with larger pores and thicker pore walls. The improved pore wall thickness of this material significantly enhances the thermal and hydrothermal stability compared to mesoporous MCM-41 and related silica.[7-9] Interestingly, SBA-15 materials additionally feature microporosity in the walls of the mesopores, meaning they are connecting neighboring mesopores.[10]

The microporosity is controlled by the nature of the surfactant, which is in the case of SBA-15 the triblock co-polymer P123. P123 consists of poly(ethylene oxide)-poly(propylene oxide)-poly(ethylene oxide) chains (PEO-PPO-PEO, see also Figure 62). Under the respective synthesis conditions, micelles are formed where the hydrophilic PEO chains interact with each other sharing their hydration sphere. In addition, the EO headgroups of neighboring micelles also interact with each other. This interaction is still present when the silica network is formed, leading to microporous channels within the silica framework even after removing the template. This process was well investigated by Galarneau *et al.* or Impéror-Clerc *et al.*[7, 10] and is schematically represented in Figure 62. In combination with other studies,[11, 12] adapted synthesis conditions and especially hydrothermal aging at elevated temperatures are promising approaches to tune the mesopore size, wall thickness and microporosity of SBA-15 materials. The reduction of microporosity is based on the dehydration of the PEO chains and a decrease of the corresponding interaction. This causes a retreat of the PEO closer to the PPO part, which also leads to a swelling effect of the micelles, as illustrated for step 2 in Figure 62.

Another strategy follows the addition of a ionic compounds like e.g. NaCl or NH_4F, which influence the formation of the hydration sphere of the PEO chains. As a consequence, their interaction is weakened and the microporosity is reduced.[13-17] Furthermore, fluoride is a well-known catalyst for the polymerization of silica species.[18, 19] It is proposed that the strong affinity of silicon to fluorine and the ability of F^- to attack Si^{x+}-species lead to the expansion or substitution of its coordination sphere. Changing the Si coordination may facilitate the loss of –OR groups, generating more electrophilic species and consequently accelerates the polymerization.[20, 21] The addition of NH_4F as fluoride source can further reduce the solubility of P123 in the aqueous solution based on a salt-induced precipitation effect of both ionic species (NH_4^+ and F^-). This supports the micelle formation and is generally added together with alkanes like heptane[22] and hexane[23], which are used to enlarge SBA-15 mesopore sizes.

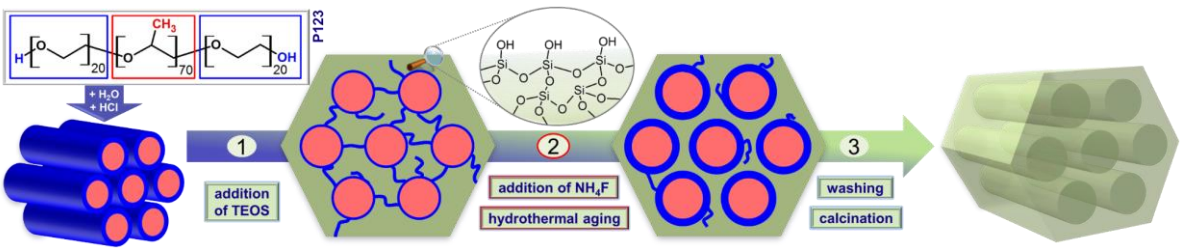

Figure 62. Overview of SBA-15 synthesis starting with the formation of hexagonal arranged P123 rods (micelles) with a hydrophilic shell (PEO, blue) and a hydrophobic core (PPO, red). Upon TEOS addition (step 1), a silica network is formed around the rods which is penetrated by hydrophilic tails of P123. These tails retreat upon hydrothermal aging (step 2), which can be supported by salt addition like NH_4F. The SBA-15 precursor is washed and calcined (step 3) to obtain a mesoporous silica SBA-15.

However, it is important to note that such synthesis approaches[22-24] combined with hydrothermal aging at elevated temperatures have been reported to lead to pore diameters close to or even larger than the distance

between the pore centers and thus equal to the unit cell parameter. Kruk and Cao[23] explained this apparent inconsistencies with the presence of large mesoporous gaps in the pore walls, supported by the presence of broadened pore size distribution together with a strong tailing. Such a formation of so called "mesotunnels" in the silica wall was described by Fan *et al.*[25] upon combination of hydrothermal treatment and the addition of tetramethylbenzidine (TMB; no fluoride source added). Also the addition of NH_4F alone is reported to promote the growth of the mesopore size exceeding the unit cell parameters.[13] Concluded, the so far mentioned synthetic adaptions led to a lability of the structure and a decrease of the hexagonality of the pores.

However, although based on comparable synthesis conditions, it was alternatively reported that highly ordered hexagonal mesostructured composites can be prepared by fluoride addition.[26, 27] It reveals that the effect of fluoride on the mesoporous silica network is diversely and still not completely understood, but it is clearly demonstrated that it has a significant impact. Within this study we report on the impact of fluoride on the integrity of the silica network of SBA-15 by a systemic variation of the fluoride concentration. In addition, the corresponding aging conditions are investigated and combined with the fluoride approach. All synthesized samples were thoroughly analyzed with N_2 physisorption technique to identify the BET surface area, microporosity and pore size distributions. Changes in the unit cell parameters were identified using low angle XRD. The surface acid/base and redox properties of selected SBA-15 samples were validated by the oxidation of isopropanol as test reaction.

4.3 Experimental section

SBA-15 synthesis was divided into two categories. Category I was the synthesis of conventional SBA-15 without NH_4F and aging at 80 °C. For this synthesis an automated reactor setup (METTLER TOLEDO LabMax) was used, applying a constant stirring of 250 rpm. It was performed by firstly dissolving the triblock copolymer P123 ($PEO_{20}PPO_{70}PEO_{20}$, 30 wt.-%, SIGMA ALDRICH; 0.005 eq) in 1.6 M HCl (SIGMA ALDRICH, 37 %, diluted with ultrapure H_2O; 0.005 eq) at 45 °C followed by the addition of tetraethyl orthosilicate (SIGMA ALDRICH, ≥ 99 %, TEOS; 1.000 eq). The mixture was stirred for 1 d at 45 °C (precipitation phase) and subsequently aged at 80 °C for 12 – 84 h. Afterwards, the product was vacuum filtrated using a P4 filter funnel and washed with the fourfold amount of ultrapure H_2O. The filtered product was dried at 110 °C for 12 h and calcined at 550 – 850 °C for 6 h applying a heating ramp of 1 °C·min^{-1} under synthetic air.

Category II represents the synthesis using aging temperatures above 80 °C and the addition of NH_4F (0.05 – 0.25 eq). The educts P123, HCl and TEOS were mixed identically to the category I synthesis. After the precipitation phase, the mixture was transferred into a poly ethylene bottle in which the NH_4F was added and further stirred for 10 min without heating. The NH_4F containing mixture was subsequently transferred into a

PTFE vessel (BERGHOF) and aged at a maximum temperature of 140 °C for varying times using a drying furnace (HARAEUS T 5042). Subsequently, the material was filtered, washed, dried, and calcined at 550 °C.

Low angle X-ray diffraction (XRD) patterns were recorded using a conventional (i.e. wide angle) STOE STADI P transmission powder diffractometer, equipped with a primary focusing Ge monochromator (Cu $K\alpha_1$ radiation) and scintillation counter. In order to enhance the accuracy of the 2θ scale, a measurement mode with two symmetric scans (negative and positive 2θ) was chosen. Small amounts of powdered sample were sandwiched between two layers of polyacetate film and fixed with a small amount of X-ray amorphous grease. This sandwich was clamped into a sample holder ring. At low angles, small differences in 2θ result in significant errors on the d-spacing scale. Thus, the diffractions patterns were evaluated using correlated fitting of the asymmetric diffraction peaks. An asymmetric instrumental function was convoluted with a symmetric Voigt function representing the sample contribution. A common lattice parameter *a* and a common 2θ offset (zero error) was refined on the 100, 110 and 200 reflections of the two-dimensional hexagonal lattice for both scan ranges (negative and positive) simultaneously. Due to the internal 2θ calibration based on the symmetric scan mode and correlated fitting, the instrumental zero error can be determined with high precision, yielding a more reliable determination of the a_0 lattice parameter in turn. Thus, this procedure allows a robust and reproducible evaluation of the d-values of differently treated samples. However, it needs to be kept in mind that, due to the asymmetric peak shape and the strongly asymmetric background, both these values will depend strongly on the evaluation procedure applied. Thus, care should be taken when comparing the results of different studies on an absolute scale.

N_2 physisorption was performed in a QUANTACHROME AUTOSORB-6-B-MP machine after degassing a specific amount of the sample at 200 °C for 24 h using a heating ramp of 1 °C·min^{-1}. The resulting isotherms were recorded at the temperature of liquid nitrogen. Calculation of the surface area was performed according to the equation of Brunauer, Emmet and Teller (BET equation).[28] Therefore, adsorption data in the range of p/p_0 = 0.05 – 0.25 were used. The pore size distribution was calculated from the adsorption isotherms by the nonlocal density functional theory (NLDFT).[29] Micropores were analyzed in the range of p/p_0 = 0.20 – 0.40 using the *t*-plot method developed by De Boer *et al.*[30]

Transmission electron microscopy (TEM) imaging was performed using a THERMO FISHER SCIENTIFIC TALOS F200X TEM operated at 200 kV acceleration voltage.

Isopropanol oxidation was performed by using 1 ml of the catalysts in a sieve fraction of 200 – 300 µm, which was placed in a stainless steel plug flow reactor with 4 mm inner diameter. The samples were surrounded by quartz wool plugs on both sides. Prior to testing, all samples were pre-treated at 300 °C for 3 h in synthetic air (21 % O_2 in N_2). The oxidation test was performed by applying a heating ramp of 1 °C·min^{-1}

up to 250 °C followed by a dwell of 3.5 h at 250 °C. Isopropanol (Rotisolv ≥ 99.5 %, LC-MS grade, CARL ROTH) was filled into a gas saturator located before the reactor with a constant temperature of 21.9 °C (p_0 = 0.0502 bar) which equals 1.2 % final isopropanol concentration in the gas feed, together with 5 % O_2 and 93.8 % N_2 at 100 ml·min^{-1} overall gas flow. Oxygen was added to prevent the reduction of the silica surface which suppresses the formation of isopropyl ether.[31] Gases from and to the reactor and gas saturator flowed through stainless steel tubes with an inner diameter of 1/8 inches. The products were identified using an online gas chromatograph (AGILENT 6890N) equipped with a flame ionization detector (FID) and thermal conductivity detector (TCD).

4.4 Results and discussion

An overview of all synthesized samples including their synthesis conditions and characterization data is presented in Table 7.

4.4.1 High temperature aging and NH_4F addition

Mesoporous silica SBA-15 is known for its high surface area of up to almost 1000 m^2·g^{-1} when synthesized at standard conditions.[6] This property is associated with a distinct microporosity, which might be undesired when SBA-15 is applied as support material for catalytic studies. A popular approach to reduce microporosity is a high temperature aging step, meaning the application of temperatures greater than 80 °C for defined times. In the following, aging conditions are given as X/Y (X = dwell time, t in h and Y = temperature, T in °C; also see overview in Table 7).

Already the low temperature aging (LTA) at 80 °C shows the significant impact of the aging time. Whereas 12 h aging led to a total surface area (S_{total}) of 1053 m^2·g^{-1} with 373 m^2·g^{-1} micropore surface area ($S_{\mu\text{-pore}}$). Increasing the time to 24 h led to a S_{total} of 992 m^2·g^{-1} and $S_{\mu\text{-pore}}$ of 283 m^2·g^{-1}. This represents a reduction of the microporosity of ca. 25 %, whereby S_{total} was only reduced by ca. 6 %. A further increase of the aging time led to a negligible change in S_{total} as well as $S_{\mu\text{-pore}}$. Therefore, the aging temperature was further modified at aging times of 24 h (Figure 63). This high temperature aging (HTA) approach was applied for T = 80 – 140 °C. Here, sample HTA_24/80 is a reproduction of LTA_24/80. The difference is the use of pressure vessels for the HTA series. The repetition of HTA_24/80 in the modified setup led to a S_{total} of 962 m^2·g^{-1} and $S_{\mu\text{-pore}}$ of 300 m^2·g^{-1}, showing a reasonable accordance to the LTA approach. Therefore, it is stated that the modified setup has no significant impact on the synthesis procedure. For the HTA series, a clear correlation of S_{total}, $S_{\mu\text{-pore}}$ and the average mesopore diameter (D_p) is identified. Whereas S_{total} and $S_{\mu\text{-pore}}$ are steadily decreasing with increasing temperature, D_p is increasing from 75.9 Å to 108.9 Å. As mentioned above, this observation is explained by the retreat of the hydrophilic tails of the P123 into the mesopores and the accompanied swelling effect of the mesopores(Figure 62).

Table 7. Overview of SBA-15 synthesis conditions (aging time and temperature, calcination temperature, NH_4F equivalents) and properties

Sample label	Aging time [h] and temp. [°C]	Calc. temp. [°C]	NH_4F eq.	S_{total} [$m^2 \cdot g^{-1}$][a]	$S_{\mu\text{-pore}}$ [$m^2 \cdot g^{-1}$][b]	D_p [Å][c]	a_0 [Å][d]	$a_0 - D_p$ [Å][e]	FHI #
LTA_12/80	12 / 80	550	0	1053	373	73.1	111.0	37.9	24827
LTA_24/80	24 / 80	550	0	992	283	75.9	112.4	36.5	24836
LTA_84/80	84 / 80	550	0	955	277	81.4	114.8	33.4	24743
HTA_24/80	24 / 80	550	0	962	300	75.9	111.3	35.4	24883
HTA_24/100	24 / 100	550	0	1008	285	75.9	115.8	39.9	24908
HTA_24/110	24 / 110	550	0	902	206	81.4	118.8	37.4	24920
HTA_24/120	24 / 120	550	0	818	173	87.8	118.7	30.9	24921
HTA_24/130	24 / 130	550	0	666	115	94.2	118.6	24.4	24922
HTA_168/130	168 / 130	550	0	562	107	108.9	119.8	10.9	25235
HTA_312/130	312 / 130	550	0	370	69	129.9	120.4	-9.5	25238
HTA_24/140	24 / 140	550	0	535	94	108.9	121.5	12.6	24923
$NH_4F_{0.05}$_24/80	24 / 80	550	0.05	652	130	94.2	123.0	28.8	28660
$NH_4F_{0.10}$_24/80	24 / 80	550	0.10	542	93	104.9	124.3	19.4	28661
$NH_4F_{0.15}$_24/80	24 / 80	550	0.15	466	83	108.8	124.9	16.1	28662
$NH_4F_{0.20}$_24/80	24 / 80	550	0.20	426	75	116.8	124.6	7.8	28663
$NH_4F_{0.05}$_24/110	24 / 110	550	0.05	459	86	117.0	124.2	7.2	28461
$NH_4F_{0.10}$_24/110	24 / 110	550	0.10	523	62	113.0	124.6	11.6	26894
$NH_4F_{0.15}$_24/110	24 / 110	550	0.15	367	54	126.0	124.7	-1.3	26897
$NH_4F_{0.05}$_72/110	72 / 110	550	0.05	243	36	127.9	127.1	-0.8	28505
$NH_4F_{0.10}$_72/110	72 / 110	550	0.10	237	25	133.8	129.3	-4.5	28506
$NH_4F_{0.15}$_72/110	72 / 110	550	0.15	153	18	200.6	130.3	-70.3	28507
$NH_4F_{0.05}$_168/110	168 / 110	550	0.05	224	26	199.0	127.0	-72.0	28466
$NH_4F_{0.10}$_168/110	168 / 110	550	0.10	195	20	238.0	129.1	108.9	26896
$NH_4F_{0.15}$_168/110	168 / 110	550	0.15	108	9	350.0	n/a	n/a	28467
$NH_4F_{0.05}$_24/130	24 / 130	550	0.05	470	75	104.9	121.5	16.6	26890
$NH_4F_{0.10}$_24/130	24 / 130	550	0.10	390	49	121.2	124.1	2.9	26040
$NH_4F_{0.20}$_24/130	24 / 130	550	0.20	230	24	129.9	125.7	-4.2	28564
$NH_4F_{0.25}$_24/130	24 / 130	550	0.25	194	10	166.9	125.9	-41.0	28565
$NH_4F_{0.05}$_168/130	168 / 130	550	0.05	191	13	166.8	124.4	-42.4	26041
$NH_4F_{0.10}$_168/130	168 / 130	550	0.10	154	13	199.0	124.6	-74.4	26042
$NH_4F_{0.20}$_168/130	168 / 130	550	0.20	26	4	273.7	123.7	150.0	26043

[a]total BET surface area; [b]micropore surface area; [c]average pore diameter determined from the adsorption isotherms by the NLDFT method; [d]hexagonal unit-cell parameter determined from low angle XRD; [e]apparent pore wall thickness estimated by subtracting the pore diameter value (D_p) from the unit-cell dimension (a_0)

S_{total} decreases from 962 $m^2 \cdot g^{-1}$ (HTA_24/80) to 535 $m^2 \cdot g^{-1}$ (HTA_24/140), which corresponds to a loss of 46 %. The $S_{\mu\text{-pore}}$ decreases as well to less than 100 $m^2 \cdot g^{-1}$ (or by 69 %). The highest temperature of 140 °C has to be applied with care due to a possible decomposition of P123.[7] Since the HTA_24/130 sample shows also a lower proportional $S_{\mu\text{-pore}}$ of 17 % (HTA_24/140: 18 %), 130 °C should be regarded as the maximum aging temperature for SBA-15 precursors. The distinct microporosity even at high HTA conditions is in contrast to reported results,[7] where micropore-free SBA-15 materials at 130 °C aging are gained. This might be based on diverging physisorption analytics. However, HTA shows the distinct reduction of microporosity, going along with the reduction of S_{total} and the increase of D_p. By determining the hexagonal unit-cell parameter a_0 from low angle XRD, the apparent pore wall thickness can be estimated by subtracting D_p from a_0. Hereby, a decrease in wall thickness from 39.9 Å to 12.6 Å is detectable, which is likely based on the increasing D_p. For the aging temperature of 130 °C also the dwell time was varied to 168 h and 312 h (samples HTA_168/130 and HTA_312/130, see Figure S73). Interestingly, the increased dwell time has the strongest impact on the pore wall thickness, which decreases from 24.4 Å (dwell: 24 h) to 10.9 Å (dwell: 168 h) to -9.5 Å (dwell: 312 h), whereby the negative pore wall thickness has no physical meaning. Therefore, it is assumed that the SBA-15 material has lost its highly symmetric character and hexagonality, maybe due to the decomposition of the structure directing agent P123. It seems reasonable since for sample HTA_312/130 the detectable S_{total} of 370 $m^2 \cdot g^{-1}$ is lower compared to sample HTA_24/140, which is already identified as critical. Thereby, the samples develop a rather SBA-15-like character due to a decrease of their characteristic symmetry.

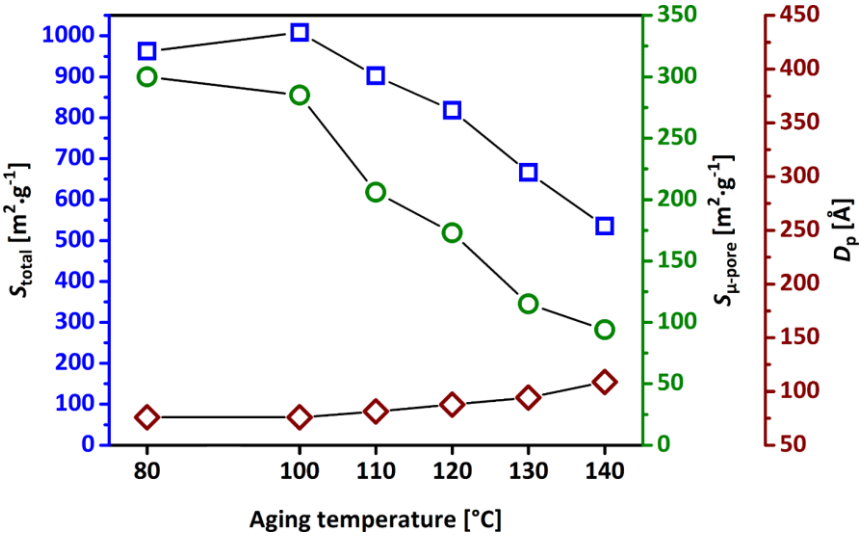

Figure 63. Total surface areas (S_{total}), micropore surface areas ($S_{\mu\text{-pore}}$) and mesopore diameters (D_p) of SBA-15 aged at 80 – 140 °C for 1 d.

To further investigate the effect of decreasing microporosity and hexagonality, the HTA_24/80 conditions were combined with the addition of NH_4F. The stepwise increase of the NH_4F concentration up to 0.20 eq (sample $NH_4F_{0.20}$_24/80) is accompanied by a pronounced decrease in the S_{total} as well as the $S_{\mu\text{-pore}}$ down to

426 $m^2 \cdot g^{-1}$ and 75 $m^2 \cdot g^{-1}$, respectively, and an increase of D_p up to 116.8 Å (Figure 64). The corresponding wall thicknesses are also decreased down to 7.8 Å. The effect of the NH_4F addition, however, is approaching a plateau, which indicates that the maximum effect of the NH_4F addition is reached. Nevertheless, the calculated pore wall thickness of 7.8 Å at a S_{total} of 426 $m^2 \cdot g^{-1}$ is already very low for SBA-15 materials and below the S_{total} of sample HTA_24/140, which were identified as critical synthesis conditions.

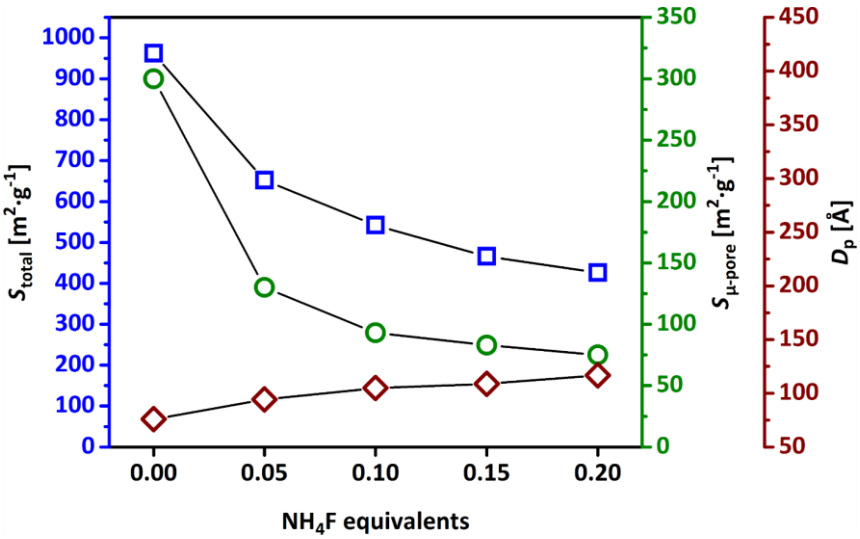

Figure 64. Total surface areas (S_{total}), micropore surface areas ($S_{\mu\text{-pore}}$) and mesopore diameters (D_p) of SBA-15 aged at 80 °C for 24 h with addition of different NH_4F equivalents of 0.00 – 0.20.

To explore the limitations of the NH_4F addition within another parameter field, the amount was varied up to 0.25 eq at 130 °C aging temperature and aging times of 24 h and 168 h, respectively (Figure 65). The general impact of the NH_4F addition for 24/130 is also observed, whereby the higher aging temperatures led to an ongoing decrease of the $S_{\mu\text{-pore}}$ down to 24 $m^2 \cdot g^{-1}$ for sample $NH_4F_{0.25}$_24/130. This corresponds to a 5 % proportion of the S_{total} of 194 $m^2 \cdot g^{-1}$, which represents an almost micropore-free material but with a negative wall thickness of -41.0 Å. The extended aging times from 24 h to 168 h led to the same trends with steeper decrease of all surface properties ($S_{\mu\text{-pore}}$, S_{total}) and increase of D_p, which stands for a pronounced negative wall thickness and a loss of the structural integrity, as seen for sample $NH_4F_{0.20}$_168/130 with -150 Å pore wall thickness. This sample has lost the structural and symmetrical characteristic of a SBA-15 sample and is rather interpreted as disordered silica. Only the $NH_4F_{0.05}$_24/130 sample shows a reasonable positive wall thickness of 16.6 Å and exhibits comparable properties as sample $NH_4F_{0.15}$_24/80. This means a difference of 0.1 eq of NH_4F has the same influence as a 50 °C higher aging temperature. The effect of the NH_4F addition on the SBA-15 properties represents a sensitive parameter for a structural manipulation, which is further confirmed by an intermediate aging temperature of 110 °C (Figure S74) resulting in a negative wall thickness for $NH_4F_{0.15}$_24/110 conditions at a S_{total} of 367 $m^2 \cdot g^{-1}$ with 15 % micropores ($S_{\mu\text{-pore}}$ = 54 $m^2 \cdot g^{-1}$). Interestingly, aging conditions of 168/110 with NH_4F additions of 0.05 – 0.15 eq resulted in larger D_p and a_0 values as for

the corresponding 130 °C aging sample series. This might be again correlated to the decomposition of P123 at 130 °C, which suppresses the swelling of the mesopores. Therefore, longer dwell times at 130 °C are not advisable, neither with salt addition nor without.

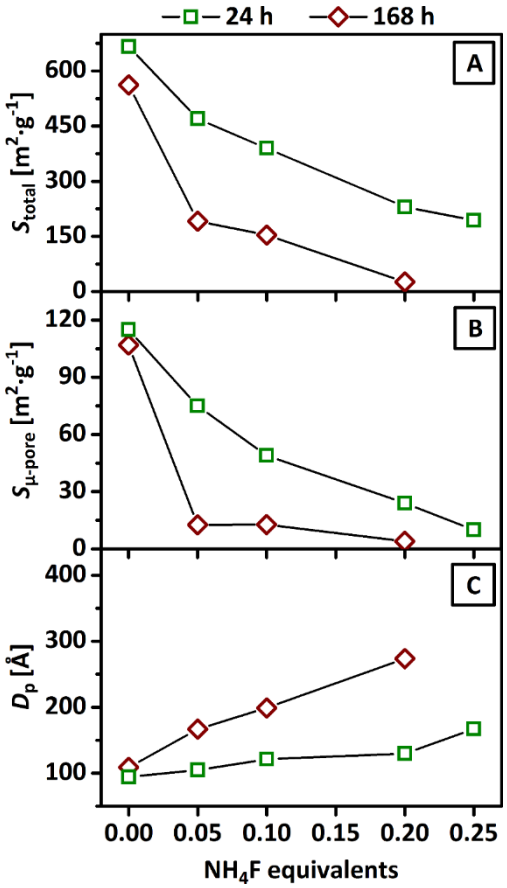

Figure 65. Total surface areas (S_{total}, A), micropore surface areas ($S_{\mu\text{-pore}}$, B) and mesopore diameters (D_p, C) of SBA-15 aged at 130 °C for 24 h and 168 h as a function of the NH_4F addition of 0.00 – 0.25 equivalents.

4.4.2 Structural consequences of LTA / HTA and NH_4F addition

Already the addition of small amounts of NH_4F amplifies the effect of the HTA on the surface and pore properties. Coupled to longer dwell times, the influences is even more significant. The first indication for a loss of structural integrity of the synthesized SBA-15 materials is the appearance of very low or negative pore wall thicknesses. To further investigate the different texture characteristics, the physisorption isotherms[32] of sample LTA_12/80 as reference for standard synthesis conditions, exhibiting the highest micropore fraction and thickest pore wall diameter, are investigated. They are compared to a serious consisting of sample LTA_24/80, the corresponding sample with additional 0.05 eq NH_4F (sample $NH_4F_{0.05}$_24/80), further treated at a higher temperature (sample $NH_4F_{0.05}$_24/110) and longer dwell time ($NH_4F_{0.05}$_72/110) as illustrated in Figure 66. For the reference sample (Figure 66A) as well as for sample LTA_24/80 (Figure 66B) the adsorption and desorption isotherms show a type V isotherm with a H1 type hysteresis loop. This is typical for narrow pore size distributions and uniformity of cylindrical pores typical for SBA-15 materials. These

structural properties guarantee also a good accessibility of the pores. The addition of a small amount of NH_4F decreased the symmetry to a H2 hysteresis loop (Figure 66C), which is usually explained by the formation of bottlenecks of relatively uniform channel-like pores. An increase in aging temperature and dwell-time strongly intensifies this effect. Thereby, sample $NH_4F_{0.05}$_24/110 (Figure 66D) shows first characteristics of a H3 type hysteresis loop, which is well developed for sample $NH_4F_{0.05}$_72/110 (Figure 66E). This kind of hysteresis loops are described for slit-like pores with strongly irregular shapes and broad size distributions.[33] Also a shift to higher relative pressures for the hysteresis is observed, which indicates an increase of the pore sizes. For sample $NH_4F_{0.05}$_72/110 (Figure 66E), additionally the absence of a plateau, as observed for the other samples at p/p_0 larger than ca. 0.9, indicates the presence of even larger pores, which are not accessible by a standard N_2 physisorption measurement.

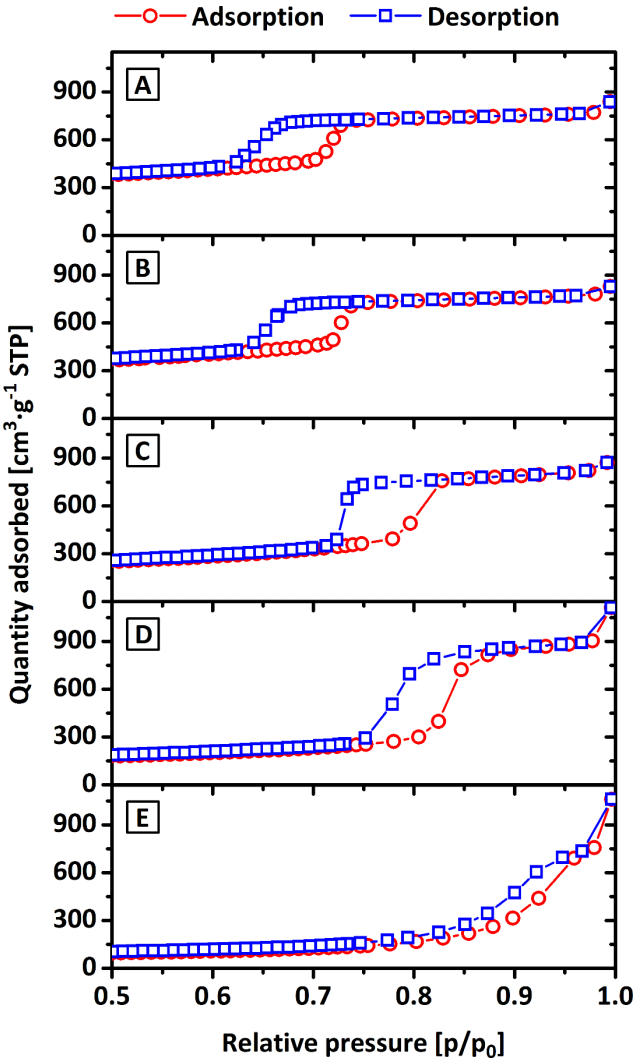

Figure 66. N_2 physisorption isotherms with adsorption (circles, red) and desorption (squares, blue) for samples LTA_12/80 (A), LTA_24/80 (B), $NH_4F_{0.05}$_24/80 (C), $NH_4F_{0.05}$_24/110 (D) and $NH_4F_{0.05}$_72/110 (E).

The indicated broad pore size distributions in the physisorption isotherms get clearly visible by analyzing the pore size distributions by the NLDFT method (for details see experimental part). Samples LTA_12/80

as highly ordered reference and $NH_4F_{0.05}$_72/110 representative for a disordered SBA-15-like structure with the lowest negative pore wall diameter value are shown in Figure 67A. For the LTA_12/80 sample pore sizes between 60 – 95 Å (average of 73 Å) are calculated, whereas the NH_4F treated sample shows a distribution in the range of 50 – 320 Å with multiple plateaus. The first plateau is located at around 75 Å, which is in good agreement with the pore sizes found for the reference sample. This is explained by in parts unmodified pore geometries. The highest number of pores are located at 128 Å which is likely based on the swelling effect of the micelles induced by the HTA, whose effect is reinforced by the NH_4F addition. The other plateaus are located at 150 – 170 Å, 210 – 230 Å and ~275 Å, and the differences between the plateaus (around 60 – 70 Å) are close to the average value of the pore size distribution of LTA_12/80. This observation suggests that pore sizes larger than about 130 Å are formed by a break or collapse of one or multiple pore walls. The connected neighboring pores might form a continuous mesopore, which originally separated several pores.[25] This might explain the negative values for the pore walls, since the breakthrough between the pores is strongly overestimating the overall pore width. This is not detectable by XRD as long as the overall periodicity remains unchanged, meaning no change in the reflex positions. It further matches with the observations and conclusions of Kruk and Cao[23] who also observed a pore size broadening with a pronounced tailing and related it to channels in the pore walls. The approximate pore size of about 130 Å for sample $NH_4F_{0.05}$_72/110 is interpreted as maximum size of a single pore, since also the calculated apparent negative pore wall diameters, a_0 minus D_p, start to appear for samples with average pore wall diameters D_p of greater or equal 126 Å (see Table 7). The highest increase in the average pore size was observed for sample $NH_4F_{0.15}$_168/110 with a D_p of 350 Å and a pore size distribution revealing pores larger than 700 Å (Figure S75). Such pore sizes are accompanied by a massive loss of structural integrity, which is verified by a non-detectable 100 reflection in low angle XRD, further indicating a collapse of the pore structure.

However, XRD not only provides a value for the unit cell parameter a_0, but can also give information about the crystallinity of the sample. Therefore, the intensity of the primary beam can be compared to the intensity of the occurring reflections, which is demonstrated in Figure 67B for the samples LTA_12/80 and $NH_4F_{0.05}$_72/110. For LTA_12/80 the 100 reflection is well visible with only a small contribution from the primary beam, the 100 reflection of $NH_4F_{0.05}$_72/110 is only visible as a small shoulder mostly overlaid by the dominant signal of the primary beam. Such an intense signal is explained by scattering of the beam at non-ordered structures. As already indicated by the negative wall thickness, amorphous fractions of the silica structure might be responsible for this phenomenon. This would be in line with a structural collapse and finally with the loss of SBA-15 typical symmetry and properties.

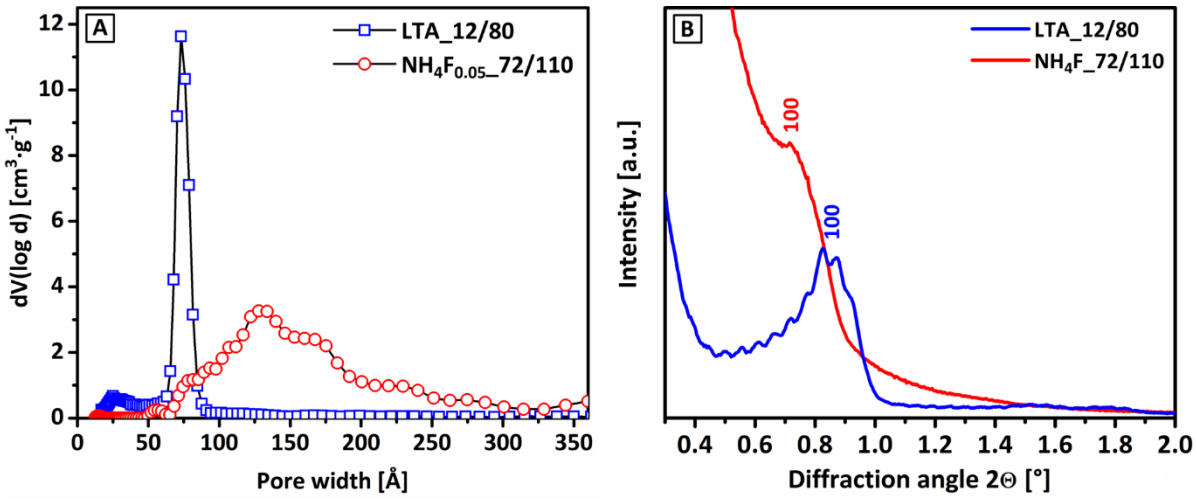

Figure 67. Pore size distributions (A) and low angle XRD (B) of samples LTA_12/80 (blue) and $NH_4F_{0.05}$_72/110 (red).

For further clarification, sample $NH_4F_{0.05}$_72/110 was analyzed by TEM. As shown in Figure 68A, the sample exhibits well defined pore structures with diameters between 75 – 98 Å. This is in very good agreement with the pore size distribution of sample LTA_12/80 and the plateau for sample $NH_4F_{0.05}$_72/110 in Figure 67A. Pore walls are approximately 13 – 16 Å thick with variations of only a few Å. Also breakthroughs connecting two channels are detected. The dominant motive, however, is seen in Figure 68B, with mainly disordered and not well-defined channels. Here, pore diameters of up to 270 Å are detected, which derived from a fuse of multiple channels. Furthermore, the disordered structures also show fractionized silica parts without any order or even isolated structures (see also Figure S76). Those disordered loose fractions are likely identified as origin for the intense primary beam in XRD analysis (see Figure 67B). Overall, TEM analysis supports the findings from physisorption and XRD analysis.

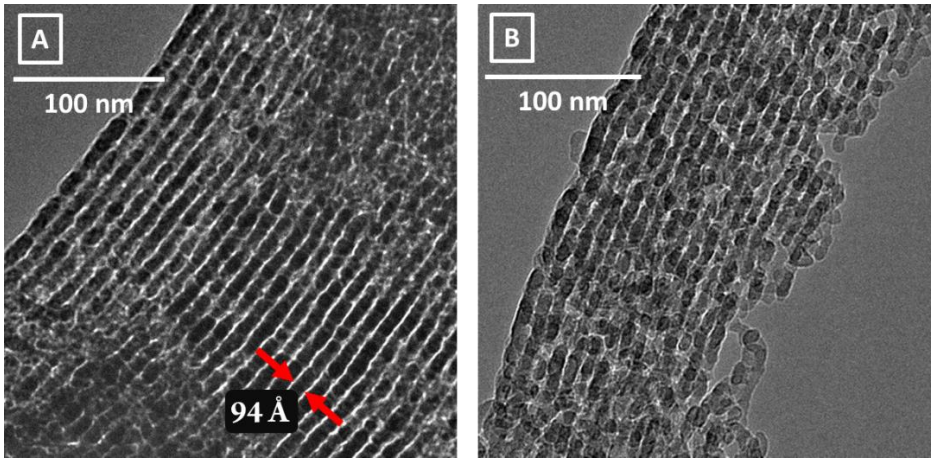

Figure 68. TEM analysis of sample $NH_4F_{0.05}$_72/110 showing in parts regular (A) and disordered structures (B).

Generally, all aging parameters like time, temperature and NH_4F addition point in the same direction and might also have an equal and cross-correlating impact on all surface and structure parameters. In Figure 69 an

overview of all synthesized samples is shown, whereas D_p and $S_{\mu\text{-pore}}$ is presented as a function of S_{total} and a_0 as a function of D_p (inset Figure 69A). A clear correlation of the parameters is visible. Down to around 500 $m^2 \cdot g^{-1}$, D_p shows a linear dependence and $S_{\mu\text{-pore}}$ is nearly exponentially increasing. For S_{total} values greater 500 $m^2 \cdot g^{-1}$, the $S_{\mu\text{-pore}}$ shows a linear dependence and D_p values greater 120 Å an exponential dependence. Samples that exhibit a S_{total} below 500 $m^2 \cdot g^{-1}$ showed solely pore wall thicknesses above 10 Å, D_p below 113 Å and a_0 larger 125 Å. This in good agreement with the described appearance of negative pore wall diameters analyzed for samples with average pore wall diameters above 126 Å. A similar conclusion is drawn by comparison of the evolutions of a_0 and D_p (inset Figure 69A). Values for a_0 are at first increasing from about 100 – 125 Å and reach finally a plateau at around 125 Å. This plateau starts at D_p values of 130 Å. Since a_0 stays constant and D_p is further increased, it is assumed that the increase of D_p is related to pore connections rather than swelling.

Overall, SBA-15 samples with S_{total} bigger than 500 $m^2 \cdot g^{-1}$ seem to be in a highly ordered state with a symmetrical hexagonal structure. The decrease in S_{total} below 500 $m^2 \cdot g^{-1}$ is accompanied by a loose of ordered structures, with SBA-15-like features as seen in Figure 67A. The ongoing decrease in S_{total} is coupled to an increasing amount of fractions exhibiting no structural order, as observed by TEM analysis (Figure 67B and Figure S76). Together with the increasing negative pore wall diameters, these samples should be regarded as non-SBA-15 structures and interpreted as disordered mesoporous silica materials.

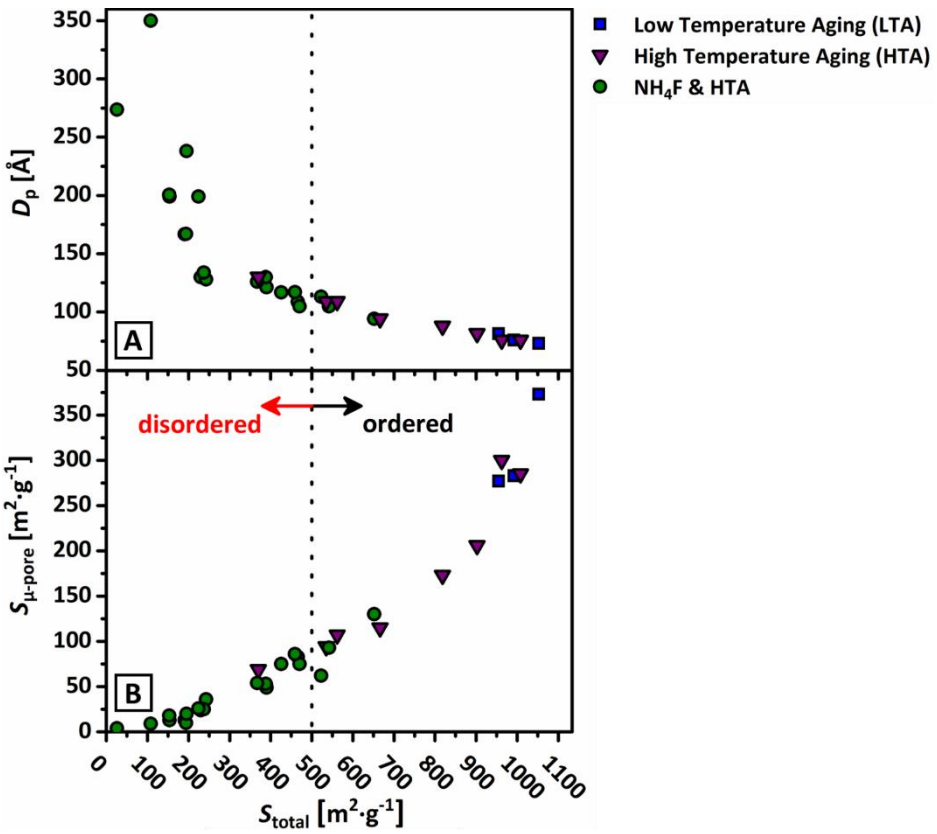

Figure 69. Mesopore diameters D_p (A) and micropore surface areas $S_{\mu\text{-pore}}$ (B) as a function of the total surface area (S_{total}) of SBA-15 aged and calcined under differing conditions. Inset of (A) shows the unit cell parameter a_0 as a function of D_p.

4.4.3 Isopropanol oxidation reaction

To translate the above described physical trends, i.e. porosity, crystallinity, structural integrity etc., into chemical ones, selected SBA-15 samples were tested in the isopropanol oxidation. The proper analysis of the reaction products of the isopropanol oxidation contains information on the nature of the active surface and its discrimination. This is based on the dehydration of isopropanol to form propylene on acidic surface sites and dehydrogenation *via* a concerted mechanism on adjacent acidic and basic surface sites (redox active sites) resulting in the formation of acetone.[34] For a better comparability, all isopropanol conversions are normalized based on the available S_{total} and are given relative to the highest detected conversion value of the most active sample $NH_4F_{0.05}$_72/110.

The sample LTA_12/80 represents the reference of a highly order SBA-15 material with a micropore fraction of 35 %. The corresponding results of the isopropanol oxidation test are shown in Figure 70. The onset of the activity is at approximately 100 °C, resulting in the formation of almost exclusively acetone. At 250 °C 72 % isopropanol is converted with a selectivity to acetone of 98 %. Concluded, the surface of LTA_12/80 contains mostly redox active sites. Sample HTA_24/130 was investigated as a representative of ordered low surface area SBA-15 materials (Figure 71). The sample exhibits a S_{total} of 666 $m^2 \cdot g^{-1}$ and the D_p (94.2 Å) and a_0 (118.6 Å) values are interpreted as indication for a structurally intact SBA-15. Although it shows a comparable onset temperature to LTA_12/80, the overall conversion did not exceed 8 %. This represents a reduction of the isopropanol conversion by 89 %, normalized to the BET surface area. It is likely that this effect is also influenced by the lowered fraction of microporosity (–69 %). The selectivity to propylene reaches a maximum of 78 % at 225 °C. During the dwell time at 250 °C the amount of propylene decreases again at stable isopropanol conversion. This observation indicates a change of the surface sites from acidic to redox-sites. Besides, compared to sample LTA_12/80, the number of acidic sites increases by a factor of around three for HTA_24/130 at 225 °C, despite the low isopropanol conversion. The change in the product selectivities as a function of time and temperatures is interpreted as an *in-situ* adaption of the surface properties under isopropanol oxidation conditions.

Since the NH_4F addition had the strongest influence on the physical properties, three selected samples with an NH_4F addition of 0.05 eq were also tested in the isopropanol oxidation reaction. The samples differ in aging temperature ($NH_4F_{0.05}$_24/80 and $NH_4F_{0.05}$_24/110) or dwell time ($NH_4F_{0.05}$_72/110). As illustrated in Figure 72, all samples exhibit comparable conversions, whereby the shape of the conversion curve is different compared to the previous samples. The isopropanol conversion curves of LTA_12/80 and HTA_24/130 reach a plateau during isothermal conditions. All three NH_4F treated samples show an ongoing and steady increase in conversion over the entire testing period.

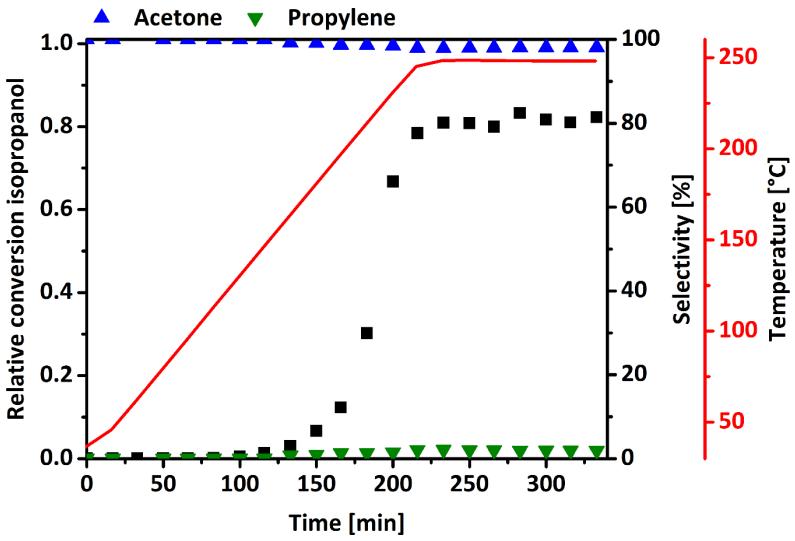

Figure 70. Isopropanol oxidation test of sample LTA_12/80. Isopropanol conversion is normalized to BET surface area.

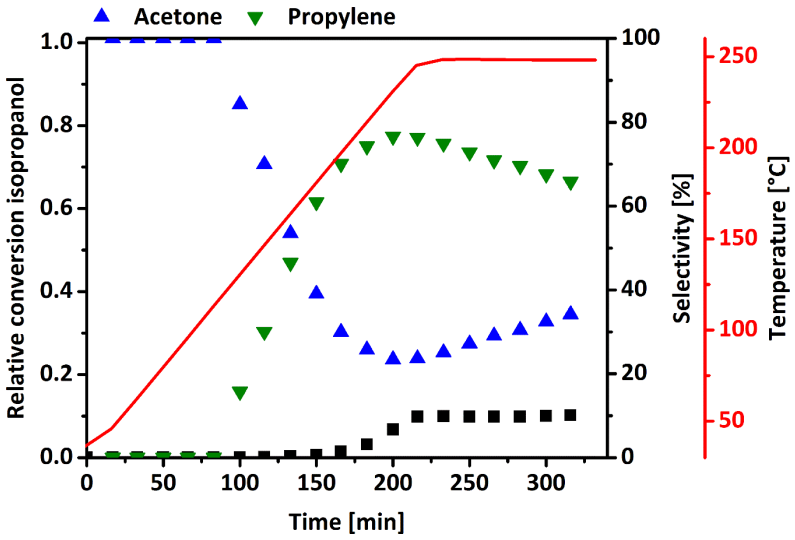

Figure 71. Isopropanol oxidation test of sample HTA_24/130. Isopropanol conversion is normalized to BET surface area.

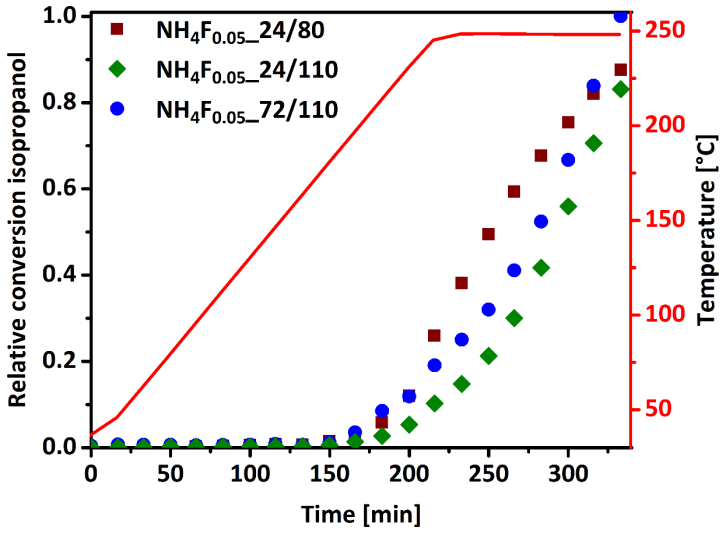

Figure 72. Isopropanol oxidation test of sample samples synthesized with the addition of 0.05 eq NH_4F and aged at 24/80 (wine) 24/110 (green) and 72/110 (green). Isopropanol conversions are normalized to BET surface area.

The absent steady conversion under isothermal isopropanol oxidation conditions is interpreted as a change in the silica structure exposing additional redox active sites induced by the NH_4F treatment. The overall conversion reaches values of around 80 % after 330 min under isopropanol oxidation at finally 250 °C. Only slight differences can be observed for the NH_4F treated samples, like a faster increase in conversion for samples snythesized under longer dwell times or higher temperature. However, all tested NH_4F modified samples show a higher conversion of isopropanol as the reference sample, although e.g. sample $NH_4F_{0.05}$_72/110 exhibits an around ten times lower micropore fraction. It is suggested that the microporosity of silica materials is not the main source of reactive sites for the isopropanol oxidation, if the structural integrity is limited. The role of NH_4F as being responsible for the continuous activation of the samples is evidenced upon direct comparison of samples with similar physical characteristics, but synthesized with and without NH_4F ($NH_4F_{0.05}$_24/80 and HTA_24/130, see Table 7). The NH_4F-free sample converts only a fraction of 4 % isopropanol to acetone if compared to the NH_4F containing sample. Regarding the selectivity, almost exclusively acetone is formed as probe for redox-sites. (Figure S77 – Figure S79).

The comparably high and non-static isopropanol conversion might be directly correlated to the already discussed formation of (amorphous-) silica fractions, almost isolated from the remaining structures, formed upon NH_4F addition (Figure 68 and Figure S76). It is likely that those loose fractures are instable and therefore are further fractured or re-functionalized under isopropanol oxidation conditions at elevated temperatures. As a consequence, the addition of NH_4F as structural promoter over-moderates the structural changes, leading to a collapse of the SBA-15 structure as observed in TEM, physisorption and XRD analysis. Finally, it also has a significantly influence on the chemical surface properties, which are important e.g. when SBA-15 is applied as support material.

4.5 Conclusion

The iterative variation of the hydrothermal aging conditions and NH_4F addition for SBA-15 synthesis conditions was used to identify a concerted evolution of SBA-15 characteristics. The addition of fluoride thereby promoted an effect already initiated by the hydrothermal aging. Hereby, a change in the cross-correlation for all investigated SBA-15 properties was observed for samples with a total surface area S_{total} of ~500 $m^2 \cdot g^{-1}$. Values for S_{total} above about 500 $m^2 \cdot g^{-1}$ exhibited a surface area dedicated to microporosity ($S_{\mu\text{-pore}}$) above about 90 $m^2 \cdot g^{-1}$ (18 %) with pore wall thicknesses above about 10 Å and average mesopore diameters D_p below about 115 Å. Thereby, the a_0 unit cell parameter did not overcome about 125 Å, even upon a further decrease in surface areas and increase in values for D_p. This might be correlated to a SBA-15 material that locally starts to lose its well-ordered structure. At values below S_{total} of about 500 $m^2 \cdot g^{-1}$, also the related cross-correlations of all discussed SBA-15 characteristics changed, evidencing a change in the SBA-15

structure. Consequently, one single property of the material could not be tuned without influencing all other investigated parameters.

A progressing structural disintegration for NH_4F modified SBA-15 structures was further supported by the appearance of pore sizes which represent multiples of the average pore diameter of a highly symmetrical reference SBA-15 material. This observation strongly suggests the collapse of pore wall structures and the coalescence of multiple mesoporous channel fractions. Upon increased fluoride concentration and harsher aging conditions, meaning increased temperature and elongated dwell times, this effect amplified, leading to a complete collapse of the SBA-15 structure and to rather amorphous silica materials.

Overall, the impact of fluoride on the silica structure was demonstrated to be significant. These data suggest that salt addition and/or hydrothermal aging cannot lead to the complete reduction of micropores without influencing the integrity of the silica structure. A consequence of the disintegration was thereby demonstrated using the oxidation of isopropanol as probe reaction for the chemical surface properties. A correlation between a change of the physical and chemical properties was demonstrated. A higher amount of disordered silica fractions thereby resulted in the formation of redox active sites on the silica surface. Finally, it is concluded that the modified synthesis conditions have a strong impact on the material's surface properties, which are directly related to their catalytic properties with severe consequences on the applicability of the SBA-15 or SBA-15-like materials.

4.6 References

[1] A. Corma, *Chem. Rev.* **1997**, *97*, 2373-2420.

[2] A. Taguchi, F. Schüth, *Micropor. Mesopor. Mat.* **2005**, *77*, 1-45.

[3] J. S. Beck, J. C. Vartuli, W. J. Roth, M. E. Leonowicz, C. T. Kresge, K. D. Schmitt, C. T. W. Chu, D. H. Olson, E. W. Sheppard, S. B. McCullen, J. B. Higgins, J. L. Schlenker, *J. Am. Chem. Soc.* **1992**, *114*, 10834-10843.

[4] P. T. Tanev, T. J. Pinnavaia, *Science* **1995**, *267*, 865-867.

[5] R. Ryoo, J. M. Kim, C. H. Ko, C. H. Shin, *J. Phys. Chem.* **1996**, *100*, 17718-17721.

[6] D. Zhao, J. Feng, Q. Huo, N. Melosh, G. H. Fredrickson, B. F. Chmelka, G. D. Stucky, *Science* **1998**, *279*, 548-552.

[7] A. Galarneau, H. Cambon, F. Di Renzo, F. Fajula, *Langmuir* **2001**, *17*, 8328-8335.

[8] K. Cassiers, T. Linssen, M. Mathieu, M. Benjelloun, K. Schrijnemakers, P. Van Der Voort, P. Cool, E. F. Vansant, *Chem. Mater.* **2002**, *14*, 2317-2324.

[9] N. Igarashi, K. A. Koyano, Y. Tanaka, S. Nakata, K. Hashimoto, T. Tatsumi, *Micropor. Mesopor. Mat.* **2003**, *59*, 43-52.

[10] M. Impéror-Clerc, P. Davidson, A. Davidson, *J. Am. Chem. Soc.* **2000**, *122*, 11925-11933.

[11] T. Klimova, A. Esquivel, J. Reyes, M. Rubio, X. Bokhimi, J. Aracil, *Micropor. Mesopor. Mat.* **2006**, *93*, 331-343.

[12] K. Miyazawa, S. Inagaki, *Chem. Commun.* **2000**, 2121-2122.

[13] V. A. Parfenov, I. V. Ponomarenko, S. M. Zharkov, S. D. Kirik, *Glass Phys. Chem.* **2014**, *40*, 69-78.

[14] S. Kubo, K. Kosuge, *Langmuir* **2007**, *23*, 11761-11768.

[15] B. L. Newalkar, S. Komarneni, *Chem. Mater.* **2001**, *13*, 4573-4579.

[16] C. Li, Y. Wang, Y. Guo, X. Liu, Y. Guo, Z. Zhang, Y. Wang, G. Lu, *Chem. Mater.* **2007**, *19*, 173-178.

[17] P. R. Desai, N. J. Jain, R. K. Sharma, P. Bahadur, *Colloids Surf., A* **2001**, *178*, 57-69.

[18] C. J. Brinker, G. W. Scherer, in *Sol-Gel Science* (Eds.: C. J. Brinker, G. W. Scherer), Academic Press, San Diego, **1990**, pp. 96-233.

[19] B. K. Coltrain, L. W. Kelts, in *The Colloid Chemistry of Silica, Vol. 234*, American Chemical Society, **1994**, pp. 403-418.

[20] H.-P. Boehm, *Angew. Chem.* **1980**, *92*, 328-328.

[21] R. Winter, J. B. Chan, R. Frattini, J. Jonas, *J. Non-Cryst. Solids* **1988**, *105*, 214-222.

[22] E. M. Johansson, M. A. Ballem, J. M. Córdoba, M. Odén, *Langmuir* **2011**, *27*, 4994-4999.

[23] M. Kruk, L. Cao, *Langmuir* **2007**, *23*, 7247-7254.

[24] S. M. L. dos Santos, K. A. B. Nogueira, M. de Souza Gama, J. D. F. Lima, I. J. da Silva Júnior, D. C. S. de Azevedo, *Micropor. Mesopor. Mat.* **2013**, *180*, 284-292.

[25] J. Fan, C. Yu, L. Wang, B. Tu, D. Zhao, Y. Sakamoto, O. Terasaki, *J. Am. Chem. Soc.* **2001**, *123*, 12113-12114.

[26] J. M. Kim, Y.-J. Han, B. F. Chmelka, G. D. Stucky, *Chem. Commun.* **2000**, 2437-2438.

[27] P. Schmidt-Winkel, P. Yang, D. I. Margolese, B. F. Chmelka, G. D. Stucky, *Adv. Mater.* **1999**, *11*, 303-307.

[28] S. Brunauer, P. H. Emmett, E. Teller, *J. Am. Chem. Soc.* **1938**, *60*, 309-319.

[29] J. P. Olivier, *J. Porous Mater.* **1995**, *2*, 9-17.

[30] J. H. de Boer, B. C. Lippens, B. G. Linsen, J. C. P. Broekhoff, A. van den Heuvel, T. J. Osinga, *J. Colloid Interface Sci.* **1966**, *21*, 405-414.

[31] J. E. Rekoske, M. A. Barteau, *J. Catal.* **1997**, *165*, 57-72.

[32] K. S. W. Sing, R. T. Williams, *Adsorpt. Sci. Technol.* **2004**, *22*, 773-782.

[33] M. Kruk, M. Jaroniec, *Chem. Mater.* **2001**, *13*, 3169-3183.

[34] M. Ai, S. Suzuki, *J. Catal.* **1973**, *30*, 362-371.

4.7 Supporting information

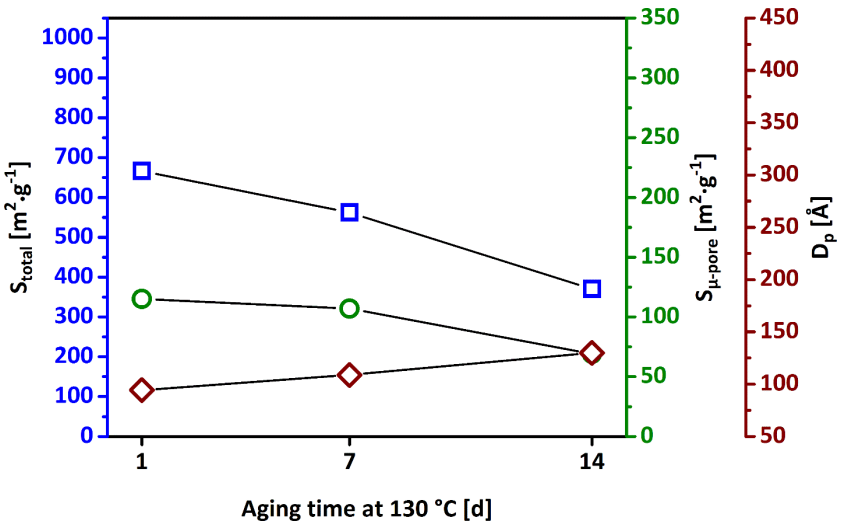

Figure S73. Total surface areas (S_{total}), micropore surface areas ($S_{\mu\text{-pore}}$) and mesopore diameters (D_p) of SBA-15 aged at 130 °C for 1, 7 and 14 d.

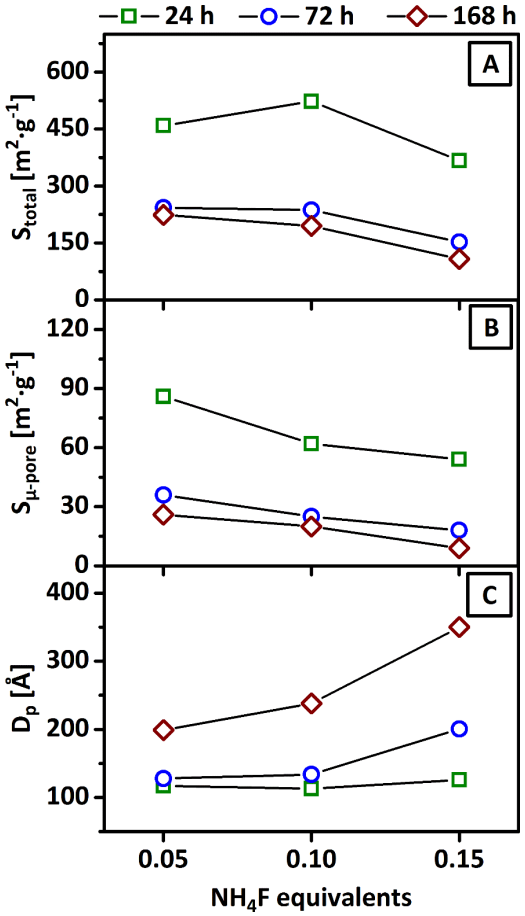

Figure S74. Total surface areas (S_{total}, A), micropore surface areas ($S_{\mu\text{-pore}}$, B) and mesopore diameters (D_p, C) of SBA-15 aged at 110 °C for 1 – 7 d as a function of the NH_4F addition of 0.05 – 0.15 equivalents.

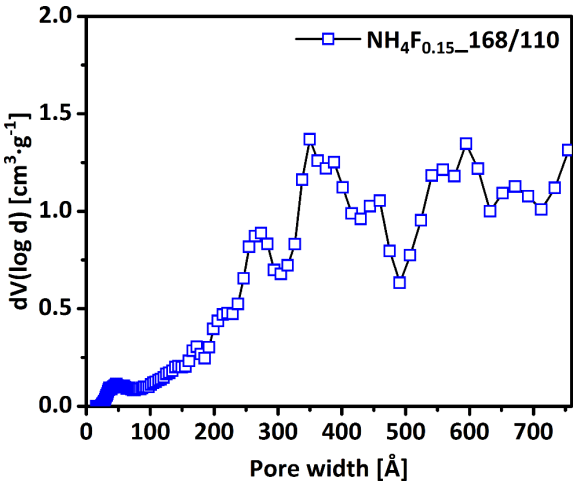

Figure S75. Pore size distribution of sample $NH_4F_{0.15}$_168/110.

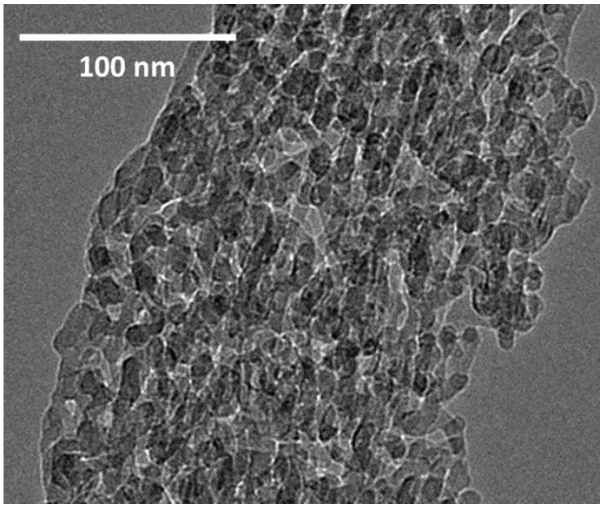

Figure S76. TEM image of sample $NH_4F_{0.05}$_72/110 showing fractioned silica structures.

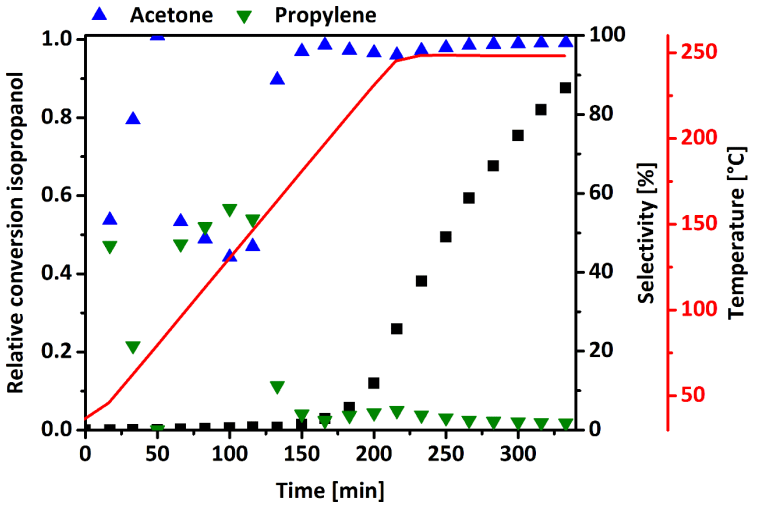

Figure S77. Isopropanol oxidation of SBA-15 samples synthesized with the addition of 0.05 eq NH_4F and aged at 80 °C for 24 h ($NH_4F_{0.05}$_24/80).

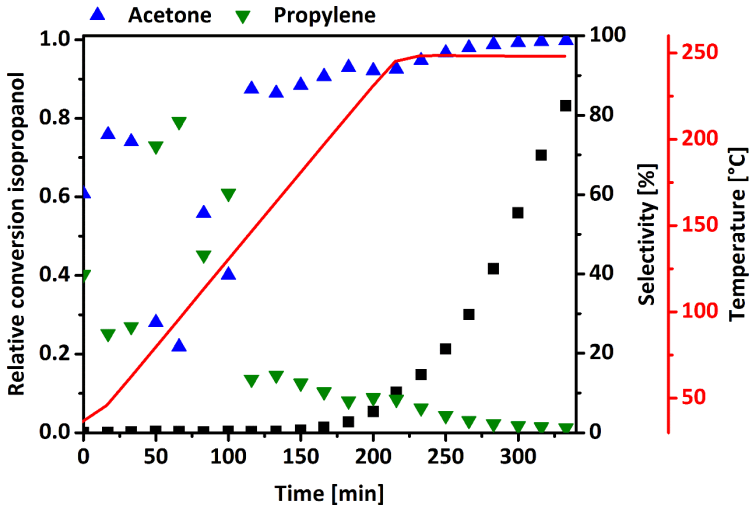

Figure S78. Isopropanol oxidation of SBA-15 samples synthesized with the addition of 0.05 eq NH_4F and aged at 110 °C for 24 h ($NH_4F_{0.05}$_24/110).

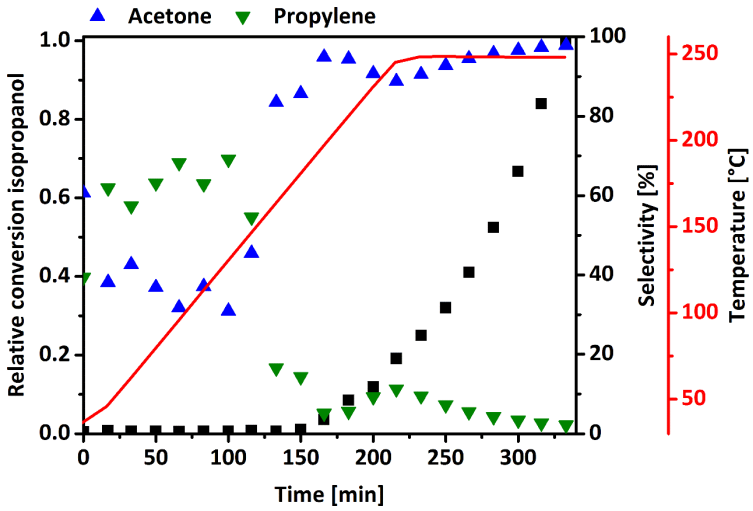

Figure S79. Isopropanol oxidation of SBA-15 samples synthesized with the addition of 0.05 eq NH_4F and aged at 110 °C for 72 h ($NH_4F_{0.05}$_72/110).

5 Summary and final conclusion

The essential basis for investigations on supported silver nanoparticles in the lower nanometer regime is a successful synthesis concept. Within this work the synthesis and stabilization of supported silver catalysts is demonstrated, based on an advanced incipient wetness impregnation technique. This strategy allowed the creation of silver nanoparticles below 6 nm with a narrow size distribution and median particle size of around 2 nm. Additionally, silver clusters below 1 nm were obtained by an *in-situ* formation approach. Based on the developed class of materials, this thesis demonstrated the effect of the silver nanostructuring with respect to its catalytic performance discussed in the two main chapters (chapter 2 and chapter 3).

In chapter 2, the catalytic oxidation of carbon monoxide was applied as suitable catalytic test reaction. Silica supported silver nanoparticle catalysts as well as a corundum supported bulk-like silver catalysts were thoroughly analyzed. Thereby, silver nanoparticles showed a high tendency to form carbonates, demonstrated by X-ray diffraction, being absent for the bulk-like reference sample. These nanoparticle catalysts were highly active in carbon monoxide oxidation, after a dedicated pre-treatment which is related to the carbonate formation. Performing detailed investigations concerning the pre-treatment conditions it was further demonstrated that silver nanoparticles need a significantly harsher pre-treatment compared to bulk-like silver particles, potentially based on the desorption of oxygen and creation of an increased number of adsorption sites. This pre-treatment dependence might also be a severe reason for differentiated findings in literature concerning silver nanoparticles and their catalytic performance. Further, *in-situ* formed silver clusters showed a significantly higher activity in carbon monoxide oxidation.

Thermal desorption spectroscopy experiments were performed to investigate the oxygen desorption behavior, which is influenced by the silver – oxygen interaction strength. Silver nanoparticles of around 2 nm showed significantly higher oxygen desorption temperatures compared to the reference catalyst. A newly introduced method using ethylene as sensor molecule was used as complementary technique for the characterization of the silver – oxygen interaction. The formation of high temperature stable oxygen species with a strong silver – oxygen interaction on silver nanoparticles, as well as silver clusters, were identified by microcalorimetric oxygen and ethylene adsorption experiments. Silver clusters additionally exhibited diverging reaction orders compared to silver nanoparticles and showed an in parts irreversible adsorption behavior.

The adsorption of ethylene was further used as a novel technique for the determination of the accessible silver surface area. Thereby, a linear correlation of the carbon monoxide oxidation rate with the silver surface area of bulk-like silver and silver nanoparticles was identified. silver clusters exhibited a superior carbon

monoxide oxidation activity compared to nanoparticles and the bulk reference and deviated from the linear correlation. This was directly attributed to the discussed silver – oxygen interaction and a distinct size effect for silver below 1 nm, supporting the presence of a cluster size effect also for supported silver in carbon monoxide oxidation.

The knowledge gained in chapter 2 was transferred to the ethylene epoxidation reaction, which was demonstrated in chapter 3. The corresponding activity and selectivity of the most stable silver nanoparticle catalyst and the bulk silver reference catalyst was hereby investigated under industrially relevant epoxidation conditions. Based on the pre-treatment dependence for highly stable oxygen species found in chapter 2, all samples were treated in inert atmosphere to achieve their highest possible activity. Consequently, it was shown that silver nanoparticles of around 2 nm can be almost as selective as the reference catalysts. The high strength of the silver – oxygen interaction detected for silver nanoparticle allowed a more detailed view on the activation period of the silver catalysts. The variation of oxygen concentrations in and on silver allowed the identification of unselective and unreactive oxygen species. Combined with oxygen desorption experiments and a detailed kinetic approach, this finally facilitated the extraction of the selective state of silver, being poor in oxygen. This finding identified the minimization of atomic oxygen as one important prerequisite for a selective silver catalyst in the epoxidation of ethylene. It also demonstrated that only a small fraction of oxygen is needed to modify silver electronically to open the silver *d*-band, which is essential for ethylene adsorption as well as oxygen activation.

In addition, in chapter 3 it was shown that the general concept of nanostructering resulting in a high number of active sites is, particularly for silver, not without pitfalls. The formation of unexpected highly stable phases as consequence of a size effect may possibly override the positive effect of the higher dispersion. The present case showed, that for supported silver in the ethylene epoxidation, the intriguing silver – oxygen chemistry caused a particle size dependent activation phenomenon. Thus, being the origin of the controversially discussed role of silver nanoparticles and a possible particle size effect, which has now been understood and clarified.

Supplementary to the catalytic tests, in chapter 4 the synthesis of potentially applied support materials improving the synthesis and stabilization of metal nanoparticles was investigated, thereby focusing on mesoporous silica SBA-15. The iterative variation of hydrothermal aging conditions and ammonium fluoride addition for its synthesis was used to identify a concerted evolution of SBA-15 characteristics. The addition of fluoride promoted the effect already initiated by the hydrothermal aging. Upon progressing development of the materials, a limited cross-correlation for SBA-15 properties was observed. For samples with a total surface area greater than around 500 $m^2 \cdot g^{-1}$, a distinct microporosity of at least 18 % was linked to a pore wall thickness of more than 10 Å, an average mesopore diameters not exceeding 115 Å and a unit cell parameter

below about 125 Å. Consequently, one single property like the microporosity of the material could not be tuned without influencing all other investigated parameters. However, this correlation was not valid for samples falling below a total surface area of around 500 $m^2 \cdot g^{-1}$, clearly visible for unit cell parameter, which remained constant even upon further decreasing in surface areas and increasing values for the average mesopore diameter. This served as an indication that corresponding SBA-15 materials locally started to lose their well-ordered structure.

A progressing structural disintegration for ammonium fluoride modified SBA-15 structures was further supported by transmission electron microscopy and nitrogen physisorption analysis. They verified the appearance of large and unsymmetrical mesopores, representing multiples of the average pore diameter of unmodified SBA-15, being a result of the collapse of pore wall structures and the coalescence of multiple mesoporous channel fractions. Upon increased fluoride concentration and harsher aging conditions, this effect was amplified, leading to a complete collapse of the SBA-15 structure and almost amorphous silica materials. Consequently, the impact of fluoride on the silica structure was demonstrated to be significant. Furthermore, hydrothermal aging and/or fluoride addition was shown to be unable to completely reduce the micropores without a pronounced disintegration of the silica structure.

The consequence of this physical change was demonstrated using the oxidation of isopropanol as probe reaction for the chemical surface properties. A higher amount of disordered silica fractions resulted in the formation of redox active sites on the silica surface. In addition, a pure hydrothermal treatment slightly increased the acidity of the SBA-15 surface, being a critical parameter for the application as potential support material. Overall, the modified SBA-15 synthesis conditions strongly impact physical and chemical surface properties, effecting also catalytic features. Consequently, modified SBA-15 materials as support materials in heterogeneous catalysis have to be analyzed and chosen thoroughly to achieve highly selective catalytic systems.